

NONLINEAR AND RATE-DEPENDENT HYSTERESIS ELECTRO
MECHANICAL RESPONSES OF FERRO ELECTRIC MATERIALS

A Dissertation
by
AMIR SOHRABI MOLLAHOUSEF

Submitted to the Office of Graduate and Professional Studies of
Texas A&M University
in partial fulfillment of the requirements for the degree of

DOCTOR OF PHILOSOPHY

Chair of Committee,	Anastasia Hanifah Muliana
Committee Members,	Arun Srinivasa
	Miladin Radovic
	Stefan Hurlebaus
Head of Department,	Andreas A. Polycarpou

March 2015

Major Subject: Mechanical Engineering

Copyright 2015 Amir Sohrabi Mollayousef

ABSTRACT

This study presents nonlinear and time-dependent analyses of ferroelectric materials and structures. Phenomenological constitutive models are considered for simulating macroscopic responses of materials undergoing various histories of electro-mechanical inputs, such as, polarization switching under large electric fields and minor hysteretic loops under relatively low electric fields. The nonlinearity is due to large electric field inputs. The constitutive models are implemented at each material (Gaussian) points within continuum finite elements. Nonlinear finite element method is used for obtaining solutions to electro-mechanical boundary value problems (BVPs). At the end, several examples of structural analyses are presented. These examples illustrate the nonlinear and time-dependent electro-mechanical responses of smart structures.

TABLE OF CONTENTS

	Page
ABSTRACT	ii
TABLE OF CONTENTS	iii
LIST OF FIGURES	v
LIST OF TABLES	ix
1. INTRODUCTION	1
1.1 Literature Review	2
1.1.1 Material Response	2
1.1.2 Structural Behavior	6
1.2 Motivation and Research Objectives	10
2. CONSTITUTIVE MODEL FOR POLARIZATION SWITCHING	11
2.1 Phenomenological Model	13
2.2 User Element Subroutine for Abaqus/UEL	17
2.2.1 Time-Integration Algorithm at The Material Level	18
2.2.2 Solution at the Structural Level	22
2.3 Numerical Implementation	24
2.3.1 Verification of the constitutive model	25
2.3.2 Structural Analyses	27
3. MINOR LOOP CONSTITUTIVE MODEL	39
3.1 Multiple Time Integral Method	43
3.2 Time Integration Method for Multiple Integral Form	45
3.2.1 Multiple Integral Model	48
3.3 Quasi Linear Viscoelastic (QLV) Model	50
3.4 Finite Element Implementation of QLV Model	56
3.5 Numerical Implementation	60
3.5.1 Analyses of Nonlinear Electro-Mechanical Response	60
3.5.2 Structural Analyses	62
4. STRUCTURAL ANALYSES	73

4.1	Analyses of Smart Beams	73
4.1.1	Governing Equation for Electro-Active Beams	74
4.1.2	Responses of 3-Layered Active Beam Under Constant Electric Field	78
4.1.3	Numerical Validation	83
4.1.4	Effect of Frequency on the Hysteresis Responses of Active Beams	89
4.2	Large Deformation Analyses	90
4.3	Active Fiber Composites	92
4.3.1	Unit Cell of an Active Fiber Composite	95
4.3.2	Validating The AFC Model with Experiment Data	97
4.3.3	The effect of scale time on electro mechanical response of AFC	100
5.	ACTIVE TRUSSES	105
5.1	Deformed Shapes	105
5.2	Nonlinear Truss Finite Element	106
5.2.1	Space Filler Truss Configuration	108
5.2.2	Tetrahedral Beam Like Truss	112
5.2.3	Effect of Nonlinear and Time Dependent Constitutive Equation on Active Truss	116
6.	CONCLUSION	125
	REFERENCES	127

LIST OF FIGURES

FIGURE	Page
2.1 Major hysteresis loops in a piezoelectric sample: a) polarization response and b) corresponding strain response	31
2.2 Minor hysteresis loops in a polarized piezoelectric sample: a) polarization response and b) corresponding strain response	31
2.3 Hysteresis polarization and butterfly strain responses for PZT51 at zero stress	31
2.4 Saturated strain responses for PZT51 at zero stress	32
2.5 Hysteresis polarization responses under constant compressive stresses	32
2.6 Butterfly strain responses under constant compressive stresses	33
2.7 Hysteresis polarization responses under constant compressive stresses above the coercive stress	34
2.8 Butterfly strain responses under constant compressive stresses above the coercive stress	35
2.9 Active composite plate with PZT patches	35
2.10 Tip deflection of the cantilever plate due to uniform cyclic electric fields applied to the piezoelectric patches	36
2.11 The corresponding deformed shape of an active cantilever plate due to a uniform cyclic electric field applied to the piezoelectric patches	36
2.12 Tip deflection of the twisting cantilever plate due to a non-uniform cyclic electric field applied to the piezoelectric patches	37
2.13 The comparison between viscoelastic and elastic materials as host structure	38
3.1 The comparison between viscoelastic and elastic materials as host structure.	65

3.2	Linear time independent model compared with experimental strain (ε_{11}) response under electric field (E_3) with frequency 0.1 Hz in [20].	65
3.3	Linear and history dependent model compared with experimental strain (ε_{11}) response under electric field (E_3) with frequency 0.1 Hz in [20].	66
3.4	Nonlinear time dependent strain (ε_{11}) response under electric field (E_3) with frequency 0.1 Hz compared with experiment[20].	66
3.5	Nonlinear time dependent strain (ε_{11}) response under electric field (E_3) with frequency 0.1 Hz for third order model compared with experiment[20].	67
3.6	Effect of frequency of applied electric field (E_3) on strain (ε_{11}) response.	67
3.7	The effect of the higher order terms on the hysteretic response (f=0.1 Hz)	68
3.8	The butterfly-like shape of the electro-mechanical coupling response	69
3.9	Geometry of PZT-586 Telescopic Actuator (dimensions are in mm)	69
3.10	Electric potential and deflection contour of PZT-586 Telescopic Actuator	70
3.11	Tip deflection of PZT-586 comparing FEM with experiment	70
3.12	Geometry of MSI-53 (dimensions are in mm)	71
3.13	Geometry of MSI-53	71
3.14	Tip deflection of MSI-53 comparing FEM model with experiment	72
4.1	Substrated bimorph beam geometry	74
4.2	Bimorph PVDF beam geometry and placement of electrodes	82
4.3	Bimorph PVDF beam electric potential distribution	84
4.4	Tip deflection of bimorph beam, comparing Laplace solution with numerical recursive method	85
4.5	Experimental result [44] compared with Laplace solution of an actuator made of three layer active beam	88
4.6	Tip deflection of bimorph beam, comparing observing effect of frequency of applied electric field	89

4.7	Folding of bimorph PVDF beam under very high electric potential	93
4.8	Schematic for placement of Fibers and electrodes in the Epoxy matrix [34]	94
4.9	Active Fiber Composite and applying electric potential	94
4.10	Geometry of Unit Cell (dimensions are in μm)	95
4.11	Active Fiber Composite distribution of electric potential in its unit cell	98
4.12	Electro-mechanical hysteresis at 1Hz compared with experiment	98
4.13	Displacement field distribution in unite cell of AFC in mm	99
4.14	Nonlinear electro-mechanical hysteresis for different electric fields at 1Hz compared with experiment	101
4.15	Linear electro-mechanical hysteresis response of AFC model with time shift for different electric fields at 1Hz compared with experiment . .	102
4.16	Effect of frequency of applied electric field on strain response of AFC	104
5.1	One element of space filler truss	109
5.2	Planar Truss in Reference Configuration	110
5.3	The desired current configuration for the planar truss	111
5.4	The deformed configuration for the planar truss	112
5.5	The Building block of Tetrahedral beam like Truss	113
5.6	Tetrahedral beam like Truss with 150 Units that is Used as Reference Configuration	113
5.7	Cross Section View of Tetrahedral beam like Truss (perspective view)	114
5.8	Arc shape produced in the tetrahedral beam like truss	115
5.9	Cyclic shape produced in the tetrahedral beam like truss	115
5.10	Shape produced in the tetrahedral beam like truss including the all normal strains	116
5.11	Shape of tetrahedral beam that passes thought four specific points . .	117

5.12 The strain distribution in a beam like tetrahedral truss in the arc configuration	118
5.13 The electric field distribution in a beam like tetrahedral truss in the arc configuration	118
5.14 linear and time independent model for deflection under frequency 1Hz	119
5.15 linear and time dependent response for deflection under frequency 1Hz	120
5.16 nonlinear and time dependent response for deflection of beam like truss under frequency 1Hz	121
5.17 The snapshots of linear tetrahedral truss in configurations labeled in figure 5.16	121
5.18 The strain distribution in a beam like tetrahedral truss in the arc configuration with limiting strain 1%	122
5.19 The electric field distribution in a beam like tetrahedral truss in the arc configuration with limiting strain 1%	122
5.20 nonlinear and time dependent response for deflection of beam like truss under frequency 1Hz with limiting strain	123
5.21 Effect of frequency of applied electric field on strain response of tetrahedral truss	124

LIST OF TABLES

TABLE	Page
2.1 Material parameters for the time-dependent polarization of PZT-51	30
2.2 Electro-mechanical coupling parameters for PZT-51	30
2.3 Elastic constants for PZT-51 [56]	30
2.4 Material parameters above the coercive stress limit	30
2.5 Proney series for viscoelastic host structure	30
2.6 Material parameters above the coercive stress limit	30
3.1 Material Properties of PZT-586 Actuator on its peak[5]	64
3.2 Material Properties of MSI-53 Actuator [5]	64
4.1 Numerical Result from Present Model for Deflection of PVDF Bimorph	84
4.2 Coefficients for close form time dependent solution of PVDF beam	86
4.3 Material Properties of AFC	97
4.4 Nonlinear Material Properties of AFC	100

1. INTRODUCTION

Discovery of electro-mechanical coupling effect which was first seen on natural materials dates back to early days. For example, Quartz and Rochelle salt are shown to exhibit electro-mechanical coupling behavior [47]. The ability of the materials to generate electric displacement when subjected to a mechanical force or displacement was called a direct effect. The reason was, that the direct electro-mechanical coupling response was experimentally observed and quantified first. Curie brothers have studied the direct piezoelectric response [21, 55] which is attributed to the crystal structures of the materials. The inverse piezoelectric effect is observed when an electric field input causes deformations in the materials. This phenomena was also observed and mathematically quantified by Curie [21, 55]. The electro-mechanical coupling effect in ceramics is due to electric polarization. Materials that have a spontaneous electric polarization that can be reversed by the application of an external electric field are known as ferroelectric [47]. The piezoelectric ceramics considered in this study are ferroelectric materials. Piezoelectric materials first found their applications in sonar devices for emitting ultrasonic waves. Other applications of piezoelectric ceramics, are for sensors and actuators. The sensing and actuation are limited to small ranges of motion. Atomic force microscopy (AFM), and data reader and recorder from electro magnetic hard disk drives are just some of these applications. Recently, piezoelectric materials are being used in energy harvester devices [22].

Piezoelectric ceramics can undergo relatively small displacements that limit their applications in mechanical systems. There have been innovations in production of new amplification architectures for piezoelectric materials. The telescopic actuators

[3, 5], piezo stack actuators [8], and active fiber composites [13] are devices utilizing several actuation architectures. There have been applications and designs of piezoelectric materials and devices in order to increase motion capability. The variable geometry trusses are one of these possible applications that will be discussed and considered in this dissertation. Prior to designing active structures made of piezoelectric materials, there is a need to understand the electro-mechanical response of active materials. This has been done through the development of constitutive models. Consequently, analytical/numerical tools that allow for analyzing active structures are also needed.

This section presents a brief literature review. The review focuses on the response of electro-active ceramic based materials, electro-mechanical constitutive models and numerical methods for analyzing electro-mechanical response of active materials and structures. Motivation and research objectives are discussed at the end of this chapter.

1.1 Literature Review

1.1.1 *Material Response*

In this study piezoelectric materials are being classified as hard and soft materials. Stiff electro-active materials are typically made of ceramics, such as lead zirconate titanate (PZT) and barium titanate ($BaTiO_3$). The polymeric based materials, such as polyvinylidene fluoride (PVDF) and dielectric elastomer, are examples of soft electro-active materials. This literature review focuses on the piezoelectric ceramics based materials. Experimental studies on polarized piezoelectric materials, i.e. PZT, and piezoelectric devices [20, 8, 7] shows nonlinear ¹ electro-mechanical response, es-

¹The nonlinear behavior is considered when the responses do not satisfy proportionality and superposition conditions.

pecially under large electric fields. Linear electro-mechanical constitutive equation is only applicable when piezoelectric materials are subjected to relatively small stimuli. The large electric field applied will cause nonlinear response that does not follow proportionality and superposition of the input. Therefore, linear electro-mechanical constitutive equations, can lead to substantial error when large electric fields are applied to electro active materials and devices [30]. There have been several studies on understanding the nonlinear response of piezoelectric materials. These studies are done by taking the coupling coefficient dependent on the electric fields [20]. Another way to model the nonlinearity is by incorporating higher order electro-mechanical coupling effect in the constitutive equations. There are examples of nonlinear constitutive equation based on a higher order electro-mechanical coupling effect and their finite element implementation. Some of these constitutive equations can be found in [12, 73, 53, 58, 69], in which a linearized strain is considered. Therefore, these models are applicable for materials undergoing small strains such as ceramics based piezoelectric materials.

Another aspect that has been observed in experimental studies of piezoelectric ceramics is their rate dependent responses [85, 84]. These effects are shown by time and field dependent piezoelectric coupling coefficients and hysteresis electro-mechanical coupling. Devices made of piezoelectric materials, such as actuators, sensors and energy harvesters often to operate under oscillating stimuli, at various frequencies. It has been observed that behaviors of piezoelectric materials, even under relatively low input regimes, are history dependent[20, 7]. At higher amplitude of electro-mechanical stimuli, piezoelectric materials experience pronounced nonlinear time-dependent behaviors. It is then necessary to incorporate the nonlinear and time-dependent electro-mechanical coupling responses for analyzing performance of piezoelectric devices.

Several experimental studies have also been conducted on understanding response of ceramics based electro active materials under cyclic electric fields with amplitudes higher than the coercive electric field limits of the materials. Under such loading conditions, materials exhibit polarization switching. This Nonlinear effect has been reported in Schmidt [65], Gookin et al. [27] and [17]. It was also shown that compressive stresses that are applied along the poling axis of the ferroelectric materials could induce depolarization of the poled ferroelectric materials [50, 18, 17]. Fang and Li [17] experimentally studied changes in polarization and strain responses of a PZT specimen under a cyclic electric field input. After several cycles, the saturated polarization response converges to a constant value, which is slightly smaller than the one measured in the first cycle. An experimental study on a polarized PZT specimen under cyclic electric fields with the maximum amplitude of 85 percent of the coercive electric field of the PZT, reported by Crawley and Anderson [20], also showed nonlinear hysteresis electro-mechanical response. They observed that the effects of creep and loading rate on the piezoelectric constant were more significant at larger strains and lower frequencies. The electrical and mechanical responses of ferroelectric materials are time and frequency dependent. The experimental evidence of this phenomena is shown by Fett and Thun [23], Schaeufele and Hardtl [64], Zhou and Kamlah [83, 84], Ben Atitallah et al. [13]. Among others, Zhou and Kamlah [83, 84] showed the creep response in a soft PZT under static electric fields and compressive stresses, which were more pronounced at higher stresses and at electric fields near the coercive electric field.

There have been constitutive models developed to predict nonlinear electro-mechanical behaviors of electro-active ceramics undergoing polarization switching. These models can be classified as phenomenological (macroscopic) model based on continuum mechanics approach and micro-mechanics based models. In an analogy

to rate-independent plasticity theory, the macroscopic constitutive models have been formulated for predicting polarization switching response in ferroelectric materials due to electric field inputs. In such cases, strains and electric displacements are additively decomposed into reversible and irreversible components. The irreversible component incorporates the switching mechanism. Examples of the macroscopic models can be found in Bassiouny et al. [11, 12], Huang and Tiersten [32, 31], Kamlah and Tsakmakis [36], Linnemann et al. [48], Muliana [56]. Massalas et al. [52] and Chen [19] presented nonlinear electro-mechanical constitutive equations for materials with memory-dependent (viz. viscoelastic materials). They also incorporated the dissipation of energy due to the visco-elastic effect, which is converted into heat. It is known that the macroscopic response of materials depends strongly upon their micro-structural response, which occurs at various length scales. Microscopically motivated constitutive models that take into account polarization response of each crystal in predicting the overall nonlinear electro-mechanical response of ferroelectric materials can be found in Chen and Lynch [18], Fan et al. [17], Li and Weng [45, 46], Smith et al. [67, 66], Su and Landis [71].

Finite element (FE) method has been used for analyzing linear electro-mechanical responses of piezoelectric materials and structures. Allik and Hughes [6] are among the first authors to present FE formulation of piezoelectric materials which is used in commercial FE codes. A review of various finite element formulations for simulating linear electro-mechanical responses of piezoelectric materials is presented in Benjedou, [14]. FE method has also been used for analyzing coupled piezo-electro-hydro thermo viscoelasto-dynamic-problems [80] which focuses on linear viscoelastic and field coupling response. FE analyses of nonlinear electro-mechanical and hysteresis polarization switching responses of structures consisting of conductive and ferroelectric materials are mainly available for time (rate)-independent behavior, e.g. Kamlah

and Bohle [35], Landis [42], Zeng et al. [81], Li and Fang [44], Zhang et al. [82], Klinkel [39], Wang and Kamlah [78], Linnemann et al. [48], Klinkel et al. [40], and Muliana and Lin [58]. Macroscopic constitutive models were considered in the above FE analyses. Zeng et al. [81] presented incremental and iterative solutions for problems involving polarization switching due to high electric field and heat generation from the dissipation of energy during the domain reversal process. FE methods that also include the time (rate) - dependent effects are currently limited. Kim and Jiang [38] presented FE algorithm for simulating macroscopic polarization and strain responses in ferroelectric materials undergoing domain switching. They also defined the functions for the rate of change of the mass fractions, which allow for incorporating rate-dependent loading.

1.1.2 Structural Behavior

1.1.2.1 Active Composite Beams

Piezoelectric ceramics have been used in the form of layered composite beams. Their applications can be found for structural health monitoring, actuators and, recently energy harvesting devices. In the case of energy harvesting devices piezoelectric materials offer large power generating capacity compared to other energy harvesting sources [22]. However, the small strains in piezoelectric ceramics limits their applications for motion generation. In order to overcome this restriction they are normally used in the form of stacked beams, bimorph and multi-layer beams which forms a composite structure. The piezo ceramics can be used in many different forms in order to magnify the displacement resulted from electromechanical coupling. When large forces are expected in the device the stacked piezoelectric is used, while, the bimorph configuration is preferred when the devices are intended

to achieve large displacements. Low and Guo [49] have formulated a mathematical model for a three layer composite piezoelectric bimorph beam. A state variable was introduced in order to incorporate the hysteresis response. An experimental set up for an actuator consists of four bimorph beams, one moving plate, two guides, and one base. Each pair of bimorph beams was connected with two small hinges at each end so that the ends are free from moment and the only force acting on each end is the reacting force. They applied electric field with amplitude of 100 V on the beam with thickness of 0.0075 inch. This would result in 2620 V/m electric field through the thickness of each piezo electric layer of the bimorph beam. They used the data from the test to calibrate the material parameters in their mathematical model. A mathematical model for bending of piezoelectric composite layered beam was also developed by Raja et al. [60]. A sandwich beams was considered in their research. They presented a closed form solution for bending of a composite piezoelectric bimorph beam, and they compared the result from their analytical solution with ABAQUS finite element analyses. They also examine the effect of PZT-5H patches on bending of sandwich beam. They have shown that the transverse deflection of the beam predicted by their method correlates with results available in literature and also finite element analyses performed in ABAQUS.

Activation in shear mode for producing bending in a composite beam was studied by Kheidar et al. [37]. They compared the bending behaviors in beam by utilizing piezo electric patches for shear mode and extension mode. A first order beam theory was presented for the composite piezoelectric beam. The effect of transverse shear deformation was considered. They have shown that using piezo electric patches in shear mode for actuation can lead to higher bending deflection. A comparison between extension and shear actuators was also considered by Benjeddou et al. [15]. They analytically investigated patched beam for static and dynamic responses.

They also performed finite element simulations for PZT-5H actuated beam and compare the responses to those of the analytical model. Rakotondrabe et al. [62] used a piezoelectric unimorph system for controlling bending deformations of an active beam. They have conducted experiments on the piezoelectric unimorph beam and compensated vibration of piezoelectric unimorph. Using piezoelectric in controlling vibration in the active beam is shown to be effective to reduce unwanted vibration. The analytical results are shown to be in good agreement with their experiments [61]. Utilizing a piezoelectric composite beam as an actuator for adaptive structures has been considered by Correia et al. [25]. They treated the adaptive beam as a multilayered composite and offered general properties of the beam. They compared their work with experiments and other results from literature. They also offered a comprehensive review on different piezoelectric models and experiments used in multifunctional composites. Suleman and Venkayya [72] examined polymeric piezoelectric beams under bending. They used finite element for analyzing bending of a PVDF beam. They considered PVDF bimorph beam for sensing and also actuation. They showed that their finite element analyses is in a good agreement with the sensing and actuation experiments using PVDF beam.

1.1.2.2 Active Trusses

Truss systems consist of relatively slender members connected by joints. The joints connect the translations and allow the members to rotate with respect to each others. Recent advances in active materials, such as shape memory and electro-active materials, allow for generating autonomous compliant structures, in which the structure can change their shape from one configuration to another configuration. This shape change is controlled by utilizing the multifunctional properties of active mate-

rials. Employing embedded piezoelectric actuation to actuate truss like system has been proposed by Moored et al. [54]. They compared this type of actuation with other strategies such as tension wires for tensegrity truss like structures that aims to mimic flapping of an artificial pectoral fin. They proposed that their approach costs minimal power consumption and shows the simple design of a high performance tensegrity-based artificial pectoral fin. There have been several studies on understanding the geometry of these truss systems actuated by shape memory and piezoelectric materials. Sofla et al. [68] studies morphing hinged truss structures, where they used shape memory wires in order to activate their structure. They presented an experimental study of their prototype for different configurations. They have used a truss structure made of tetrahedrons truss elements. Macareno et al. [51] considered a linear truss made of 3D tetrahedral units for Variable Geometry Trusses (VGTs). They discussed manufacturing of prototype and the actuation methodology of the VGTs. They showed that their VGT configuration made of five-module is quite capable for positioning purposes. They have presented the detailed design of their joints and used finite element analyses in order to support the design and motion control of VGTs. Aguirrebeitia et al. [2] applied optimization technique for VGTs to modify their trusses. Aviles et al. [10] investigated the position problems in the open-loop variable geometry trusses. An optimization scheme is designed [10] in order to minimize the actuator's displacement and consequently its energy. This method has been applied to different truss architectures in specific to modular tetrahedral linear truss. Recently, Bilbao et al. [16] have considered dynamic analyses of their previously designed modular configuration.

1.2 Motivation and Research Objectives

Experimental studies show that the electro - mechanical response of piezoelectric materials is time- (and rate-) dependent. This time dependency is observed even for ceramics based piezoelectric materials, subjected to electric fields and mechanical loadings. The electro-mechanical response of these materials also depends strongly upon the applied electric fields and mechanical stresses. There have been constitutive models derived for predicting nonlinear electro-mechanical response of piezoelectric ceramics based materials. These models are focusing on time (rate) independent. Modeling the time-dependent electro-mechanical response of piezoelectric and ferroelectric ceramics based materials is still limited. The goal in this work is to capture the nonlinear and time-dependent response of electro active materials, through formulating constitutive material models and providing solutions methods. The solution methods allows for analyzing coupled nonlinear electro-mechanical and time dependent response in active structures. The analyses can support design of electro-active structures.

The objectives of this study are to:

- 1) Formulate nonlinear time-dependent electro-mechanical constitutive models of piezoelectric ceramics with small deformation gradients taking into account polarization switching and minor hysteretic behaviors.
- 2) Develop FE methods for analyzing the nonlinear and time-dependent electro-mechanical responses for piezoelectric ceramics.
- 3) Perform large scale analyses of active structures undergoing various histories of electro-mechanical stimuli.

2. CONSTITUTIVE MODEL FOR POLARIZATION SWITCHING

This chapter deals with macroscopic response of materials that possess electro-mechanical coupling behaviors, focusing on piezoelectric ceramics of Perovskite structures. The macroscopic response of the materials strongly depends on their microstructural changes when they are subjected to external stimuli. A single crystal of Perovskite undergoes a spontaneous polarization, indicating by a separation of negative and positive charges, at temperatures below its Curie temperature. This separation is quantified by a dipole moment and a dipole moment per unit volume is known as polarization. The direction of the polarization in this crystal structure is towards the positive charge. As bulk piezoelectric ceramics comprise of polycrystalline structures, the spontaneous polarization axes of all crystallites are randomly distributed upon processing the piezoelectric ceramics. Therefore, net (macroscopic) polarization is considered zero and the materials do not show macroscopic electro-mechanical coupling response. Applying an electric field in certain direction would align the poling directions of the crystallites towards the electric field direction so that the net polarization of the materials is measurable, as illustrated in Figure 2.1a, where x_3 is the direction of the electric field applied. Increasing the electric field would increase the measured polarization until it reaches the saturated value and upon removal of the electric field, there exist a remanent polarization¹. The net poling axis of the piezoelectric materials can be reversed by applying an electric field in the opposite direction to the current polarization. When the net polarization in the materials is non-zero the materials have electro-mechanical coupling responses,

¹The ability of materials to undergo spontaneous polarization and retain its polarized state after removal of electric field is called ferroelectricity. The materials with ferroelectric behavior are called ferroelectric materials.

as shown by the corresponding nonzero strain in Figure 2.1b, which shows a strain response with respect to the applied electric field.

For practical application purposes, the materials need to be polarized/poled in order to have an electro-mechanical coupling. This is done by applying a relatively large electric field, greater than the coercive electric field (E_c) of the material, until it reaches the saturated polarization, which is often done at elevated temperatures but below the Curie temperature of the material [47], then the temperature is decreased to room temperature prior to removing the electric field which results in a remanent polarization. At this stage, the polarized material would have piezoelectric effects, as shown by the minor loops in Figure 2.2a,b. By applying an electric field, the polarized material would undergo mechanical deformations or experience stresses and when a mechanical load is applied the polarized material would generate electric charge or voltage difference. Typically, electric fields and/or mechanical stresses should be applied to the piezoelectric materials with their magnitude less than the coercive limit so that they will not cause depolarization of the materials. Applying large electric field or compressive stress in the poling direction to the polarized materials would cause depolarization and consequently loss of the electro-mechanical coupling properties. The stress and electric field threshold that causes depolarization are called coercive stress and coercive electric field, respectively[70].

Polarization behaviors in the materials due to application of cyclic electric fields show hysteretic responses (see Figure 2.1 and Figure 2.2). These responses also depend on the frequencies of the electric field inputs, ambient temperatures, and existence of mechanical loading.

2.1 Phenomenological Model

A time-dependent hysteretic polarization model is formulated to describe the macroscopic polarization response of ferroelectric materials due to various histories of external electric field inputs. The model is then modified to include the effect of the mechanical stress on the polarization response of the ferroelectric materials [56, 70]. Consider an electric field input in the x_3 direction $E_3(s), s > 0$, and $E_3(s) = 0, \forall s < 0$, where s is the time history. The corresponding polarization response at current time t is:

$$P_3^t \equiv P_3[E_3(t - s), t] = R[E_3(t - s), t] + Q[E_3(t - s), t] \quad (2.1)$$

where $R[E_3(t - s), t]$ is the time-dependent reversible polarization response at current time $t \geq 0$ with $R[0, t] = 0$ and $Q[E_3(t - s), t]$ is the residual (irreversible) polarization. The reversible polarization response is expressed as:

$$R^t \equiv R[E_3(t - s), t] = R[E_3^0, t] + \int_{0^+}^t \frac{\partial R}{\partial E_3}[E_3^t, t - s] \frac{dE_3^s}{ds} ds, t \geq 0 \quad (2.2)$$

$$R[E_3^0, t] = R_0(E_3^0) + R_1(E_3^0) \left(1 - \exp\left[-\frac{t}{\tau_1}\right]\right) \quad (2.3)$$

One may consider $R[E_3^0, t]$ as the polarization at current time t due to a constant electric field applied at $s = 0$. The superscript s and t denote the representative of the previous time history and current time, respectively. Both $R_0(E_3^s)$ and $R_1(E_3^s)$ are functions of E_3^s . The characteristic time τ_1 measures the speed that the polarization changes with time. For a linear electric behavior $R_0(E_3^s)$ and $R_1(E_3^s)$ are considered as follows:

$$\begin{aligned} R_0(E_3^s) &= \kappa_0 E_3^s \\ R_1(E_3^s) &= \kappa_1 E_3^s \end{aligned} \tag{2.4}$$

where κ_0 is the dielectric constant of a macroscopically non-polarized material (corresponding to the second order permeability tensor in a multi-axial case) and κ_1 is the time dependent dielectric constant; when $\kappa_1 = 0$, a time-independent polarization behavior is considered. The state of polarization is defined through the following polarization function:

$$f(P_3^t, P_c) = \left\langle P_3^{t2} - P_c^2 \right\rangle \tag{2.5}$$

where P_c is the current polarization state, analogous to yield stress in an over stress plasticity theory, and $\langle \rangle$ are the Macaulay brackets. It is assumed that the irreversible polarization is formed when $f(P_3^t, P_c) = 0$ and $E_3^t P_3^t > 0$. The irreversible polarization is defined as:

$$Q^t \equiv Q[E_3^t] = \int_{0^+}^{E_3^t} \frac{dQ^s}{dE_3} dE_3 \tag{2.6}$$

$$\frac{dQ^t}{dE_3} = \begin{cases} \lambda \left| \frac{E_3^t}{E_c} \right|^n & \text{if } |E_3^t| \leq E_c, f = 0 \\ \mu \times \exp[-\omega(\frac{|E_3^t|}{E_c} - 1)] & \text{if } |E_3^t| > E_c, f = 0 \\ 0 & \text{if } f \leq 0 \end{cases} \tag{2.7}$$

where E_c is the coercive electric field and λ, μ, ω, n are material parameters that are calibrated from experiments. In a non-polarized sample, the current polarization state $P_c = 0$, and once the ferroelectric sample is completely polarized, the current polarization state is equal to the saturated polarization ($P_c = P_s$ or $P_c = -P_s$) see

reference [56]. Ferroelectric materials exhibit macroscopic electro-mechanical coupling response when they are macroscopically polarized. This is shown by an elongation in the material along the electric field line and a contraction in the transverse directions when the electric field is applied in the poling direction. When the electric field is applied opposite to the poling direction, the material experiences shortening along the electric field line and expansion in the transverse directions and when the electric field is applied perpendicular to the poling directions, the transverse shear deformations are shown. The macroscopic strains due to the polarization are measured through the piezoelectric constant $\mathbf{g}(\mathbf{P}_3^t)$ whose magnitude depends on the polarization state. The polarized ferroelectric material could experience depolarization $P_3^t = 0$ when a sufficient electric field is applied in the opposite direction to its poling axis. When the depolarization occurs, the materials loose their electro-mechanical coupling effect, which is represented by $\mathbf{g}(\mathbf{0}) = \mathbf{0}$. Polarizing the ferroelectric material by applying an electric field, while at the same time the ferroelectric material is under a compressive stress along the electric field line, results in reductions of the saturated and remanent polarizations and the coercive electric field. A nonlinear electro-mechanical coupling constitutive model for ferroelectric ceramics undergoing small deformations that incorporates changes in the polarization due to an electric field while undergoing mechanical stresses is:

$$\begin{aligned}\varepsilon_{ij}^t &= S_{ijkl} \sigma_{kl}^t + 4g_{nij}^t \kappa_{nm} g_{mkl}^t \sigma_{kl}^t + 2g_{kij}^t P_k^t \\ D_i^t &= 2\kappa_{im} g_{mkl}^t \sigma_{kl}^t + P_i^t\end{aligned}\tag{2.8}$$

where S_{ijkl} is the scalar component of the elastic compliance tensor measured at fixed electric field, $\sigma_{ij}^t, D_i^t, P_i^t$ are the scalar components of the mechanical stress, electric displacement and polarization, respectively, κ_{ij} is the scalar component of the permittivity constant of a polarized specimen measured at fixed stress and constant

(remanent) polarization P_r , and the small strain is defined as $\varepsilon_{ij} = \frac{1}{2}(u_{i,j} + u_{j,i})$, where u_i is the scalar component of the displacement. The scalar component of the piezoelectric constant g_{ijkl}^t depends on the current polarization state P_3^t :

$$g_{ijk}^t \equiv g_{ijk}(P_3^t) = \frac{P_3^t}{P_r} e^{-|P_3^t|/C_1} g_{ijk}^r \quad (2.9)$$

where P_r is the remnant polarization, C_1 is the material parameter that needs to be calibrated from experiment (see [56]), and g_{ijk}^r is the scalar component of the piezoelectric constant measured at constant polarization. Thus, the constitutive model in equation (2.8) is a nonlinear function of electric field and depends on time. The third component of the polarization in equation (2.8) is given in equation (2.1), while the other two components are

$$\begin{aligned} P_1^t &= \kappa_{11} E_1^t \\ P_2^t &= \kappa_{22} E_2^t \end{aligned} \quad (2.10)$$

Experimental studies show that the coercive electric field of ferroelectric materials depends on the compressive stress applied to the material along its poling direction, while little is known about the effect of tensile stress on the polarization response of ferroelectric ceramics. This is due to the fact that ceramics is brittle and has a relatively low ultimate strength under tension. It then is necessary to have the coercive electric field varies with the compressive stresses and we further assume that the coercive electric field remains unaltered with the tensile stress:

$$E_c = \begin{cases} E_c(E_c^o, \sigma_{33}^t), \sigma_{33}^t < 0.0 \\ E_c^o, \sigma_{33}^t \geq 0.0 \end{cases} \quad (2.11)$$

where E_c^0 is the coercive electric field in absence of the mechanical stresses. The exis-

tence of compressive stresses also influences the polarization response of ferroelectric materials. When a compressive stress higher than the coercive stress σ_c is applied to the polarized ferroelectric ceramics, the materials undergo the polarization switching [44]. An attempt is made to incorporate the effect of polarization switching due to a compressive stress on the overall electro-mechanical response. It is assumed that the compressive stress that is higher than the coercive stress limit affects the polarization state P_3^t and the piezoelectric constants:

$$g_{ijk}^t \equiv g_{ijk}(P_3^t) = \frac{P_3^t}{P_r} e^{-|P_3^t|/C_1} e^{-C_2 |\sigma_{33}^t|/\sigma_c} g_{ijk}^r \quad (2.12)$$

$$C_2 = 0, \text{when, } \sigma_{33}^t > -\sigma_c$$

where the material parameters σ_c, C_2 have positive values and they need to be calibrated from the experimental tests.

2.2 User Element Subrouine for Abaqus/UEL

A three-dimensional (3D) continuum finite element for nonlinear time-dependent electro-mechanical response is presented here. The following field variables: displacements in the three directions of the Cartesian coordinate system and electric potential are sampled at each node within a finite element. Here $\{\mathbf{U}^n\}^T = \{u_1^1, u_2^1, u_3^1, \dots, u_1^{Nd}, u_2^{Nd}, u_3^{Nd}\}$ and $\{\Phi^n\}^T = \{\varphi^1, \varphi^2, \dots, \varphi^{Nd}\}$ are the nodal displacement and electric potential vectors, respectively, in a single element with a number of nodes Nd . The mapping of the field variables is done through the use of shape functions $\{N^1, N^2, \dots, N^{Nd}\}$:

$$u_k = \sum_{i=1}^{Nd} N^i u_k^i \quad k = 1, 2, 3 \quad (2.13)$$

$$\varphi = \sum_{i=1}^{Nd} N^i \varphi^i$$

The corresponding strains and electric fields, which are sampled at the material integration points within the finite element, are obtained as:

$$\begin{aligned}\varepsilon_{ij} &= \frac{1}{2} (u_{i,j} + u_{j,i}) = B_{ijm}^u U_m^n \quad \varepsilon = \mathbf{B}^u \mathbf{U}^n \\ E_i &= -\frac{\partial \varphi}{\partial x_i} = B_{im}^\varphi \varphi_m^n \quad \mathbf{E} = \mathbf{B}^\varphi \mathbf{\Phi}^n\end{aligned}\tag{2.14}$$

where \mathbf{B}^u and \mathbf{B}^φ are the spatial derivative of the shape functions related to the macroscopic strain and electric field, respectively. The stress and electric displacement counterparts are determined using the constitutive relation discussed previously. The overall governing equations for the electro-mechanical deformation are formed at the structural level by imposing the energy balance equations. In this study, the nonlinear time-dependent electro-mechanical constitutive model is expressed in terms of the stress and electric field components as the independent field variables, while the displacement based finite element formulation leads to strain and electric field components as the independent variables. Thus, the constitutive model in previous sections cannot be directly implemented in the finite element. The nonlinear time-dependent response is solved incrementally by linearizing the response and iteratively correcting the residual (error) from the linearized solutions. It is necessary to define the consistent tangent stiffness, piezoelectric and dielectric constants.

2.2.1 Time-Integration Algorithm at The Material Level

The electro-mechanical constitutive model, equation (2.8), depends on the polarization state P_3^t , which is a function of the electric field input E_3^s . A time-integration algorithm is formulated based on a recursive method in order to approximate the

current polarization state. At each time t , the polarization state is approximated as:

$$\begin{aligned} P_3^t &\approx R^t + Q^t; Q^t = Q^{t-\Delta t} + \Delta Q^t \\ \Delta Q^t &\equiv \frac{dQ^t}{dE_3} \Delta E_3^t; \Delta E_3^t = E_3^t - E_3^{t-\Delta t} \end{aligned} \quad (2.15)$$

where the superscript $t - \Delta t$ denotes the previous time, ΔQ^t is the incremental irreversible polarizations, and $\Delta E_3^{t-\Delta t}$ is the history variable defining the irreversible polarization at the previous converged time. The reversible polarization in equation (2.3) is approximated as:

$$\begin{aligned} R^t &= R_0(E_3^t) + R_1(E_3^t) \left(1 - \exp \left[-\frac{t}{\tau_1} \right] \right) + \\ &\int_{0^+}^t \left\{ \frac{\partial R_0(E_3^s)}{\partial E_3} + \frac{\partial R_1(E_3^s)}{\partial E_3} \left(1 - \exp \left[-\frac{t-s}{\tau_1} \right] \right) \right\} \frac{dE_3^s}{ds} ds \\ &= R_0(E_3^t) + R_1(E_3^t) - R_1(E_3^0) \exp \left[-\frac{t}{\tau_1} \right] - q^t \end{aligned} \quad (2.16)$$

where the history variable related to the reversible polarization is:

$$\begin{aligned} q^t &= \int_{0^+}^t \frac{\partial R_1(E_3^s)}{\partial E_3} \exp \left[-\frac{t-s}{\tau_1} \right] \frac{dE_3^s}{ds} ds \\ &= \int_{0^+}^{t-\Delta t} \frac{\partial R_1(E_3^s)}{\partial E_3} \exp \left[-\frac{t-s}{\tau_1} \right] \frac{dE_3^s}{ds} ds + \\ &\int_{t-\Delta t}^t \frac{\partial R_1(E_3^s)}{\partial E_3} \exp \left[-\frac{t-s}{\tau_1} \right] \frac{dE_3^s}{ds} ds \end{aligned} \quad (2.17)$$

$$\begin{aligned} q^t &\approx \exp \left[-\frac{\Delta t}{\tau_1} \right] q^{t-\Delta t} + \\ &\left[\frac{\partial R_1(E_3^t)}{\partial E_3} \frac{\Delta E_3^t}{\Delta t} + \exp \left[-\frac{\Delta t}{\tau_1} \right] \frac{\partial R_1(E_3^{t-\Delta t})}{\partial E_3} \frac{\Delta E_3^{t-\Delta t}}{\Delta t} \right] \frac{\Delta t}{2} \end{aligned} \quad (2.18)$$

At an initial time, $q^t = q^0 = 0.0$ and $R^0 = R_0(E^0)$. Once the polarization state is determined the electro-mechanical response of the ferroelectric materials at current time can be determined. Within an incremental time Δt , the incremental nonlinear constitutive relation in equation (2.8) can be expressed in a linearized form:

$$\begin{Bmatrix} \Delta \varepsilon^t \\ \Delta D^t \end{Bmatrix} = \begin{bmatrix} \tilde{\mathbf{S}} & \tilde{\mathbf{d}}'^T \\ \tilde{\mathbf{d}} & \tilde{\kappa} \end{bmatrix} \begin{Bmatrix} \Delta \sigma^t \\ \Delta \mathbf{E}^t \end{Bmatrix} = \begin{bmatrix} \tilde{\mathbf{A}}^t \\ \tilde{\mathbf{A}}^t \end{bmatrix} \begin{Bmatrix} \Delta \sigma^t \\ \Delta \mathbf{E}^t \end{Bmatrix} \quad (2.19)$$

The consistent tangent compliance, piezoelectric, and dielectric constants are defined as:

$$\begin{aligned} \tilde{S}_{ijkl} &\equiv \frac{\partial \varepsilon_{ij}^t}{\partial \sigma_{kl}} = S_{ijkl} + 4g_{nij}^t \kappa_{nm} g_{mkl}^t & \tilde{d}_{kij} &\equiv \frac{\partial \varepsilon_{ij}^t}{\partial E_k} = \frac{\partial g_{kij}^t}{\partial P_3^t} \frac{\partial P_3^t}{\partial E_m^t} P_m^t + 2g_{mij}^t \frac{\partial P_m^t}{\partial E_k^t} \\ \tilde{d}_{ikl} &\equiv \frac{\partial D_i^t}{\partial \sigma_{kl}} = 2\kappa_{im} g_{mkl}^t & \tilde{\kappa}_{ij} &\equiv \frac{\partial P_i^t}{\partial E_j} \end{aligned} \quad (2.20)$$

where the partial derivative of the nonlinear piezoelectric constant and polarization in equation (2.20) are expressed as:

$$\begin{aligned} \frac{\partial g_{kij}^t}{\partial P_3^t} &= \left(\frac{1}{P_r} - \frac{P_3^t}{C_1 P_r} \right) e^{-\frac{|P_3^t|}{C_1}} g_{kij}^r \\ \frac{\partial P_1^t}{\partial E_1^t} &= \kappa_{11} \\ \frac{\partial P_2^t}{\partial E_2^t} &= \kappa_{22} \\ \frac{\partial P_3^t}{\partial E_3^t} &= \kappa_0 + 0.5\kappa_1 + \frac{\partial \left(\frac{dQ^t}{dE_3^t} \right)}{\partial E_3^t} (E_3^t - E_3^{t-\Delta t}) + \frac{dQ^t}{dE_3^t} \end{aligned} \quad (2.21)$$

As mentioned above, the constitutive model is implemented in a displacement based finite element framework, in which the strain and electric field variables are taken as the independent variables obtained from equations (2.13) and the corresponding

stresses and electric displacements need to be determined. The incremental strain and electric field at current time are obtained from $\Delta\boldsymbol{\varepsilon}^t = \mathbf{B}^u \mathbf{U}^{n,t} - \mathbf{B}^u \mathbf{U}^{n,t-\Delta t}$ and $\Delta\mathbf{E}^t = \mathbf{B}^\varphi \mathbf{U}^{\varphi,t} - \mathbf{B}^\varphi \mathbf{U}^{\varphi,t-\Delta t}$ respectively. For this purpose, the linearized constitutive relation in equation (2.19) is rewritten as:

$$\begin{Bmatrix} \Delta\sigma^t \\ \Delta\mathbf{D}^t \end{Bmatrix} = \begin{bmatrix} \tilde{\mathbf{C}} & -\tilde{\mathbf{e}}'^T \\ \tilde{\mathbf{e}} & \tilde{\kappa}' \end{bmatrix} \begin{Bmatrix} \Delta\boldsymbol{\varepsilon}^t \\ \Delta\mathbf{E}^t \end{Bmatrix} = [\tilde{\mathbf{B}}^t] \begin{Bmatrix} \Delta\boldsymbol{\varepsilon}^t \\ \Delta\mathbf{E}^t \end{Bmatrix} \quad (2.22)$$

where the consistent tangent stiffness, piezoelectric constant, and dielectric constants are:

$$\begin{aligned} \tilde{\mathbf{C}} &= \tilde{\mathbf{S}}^{-1} \tilde{\mathbf{e}}'^T = \tilde{\mathbf{S}}^{-1} \tilde{\mathbf{d}}'^T \\ \tilde{\mathbf{e}} &= \tilde{\mathbf{d}} \tilde{\mathbf{S}}^{-1} \tilde{\kappa}' = \tilde{\kappa} - \tilde{\mathbf{d}} \tilde{\mathbf{S}}^{-1} \tilde{\mathbf{d}}'^T \end{aligned} \quad (2.23)$$

Finally, the stresses and electric displacements at current time are:

$$\begin{aligned} \boldsymbol{\sigma}^t &= \boldsymbol{\sigma}^{t-\Delta t} + \Delta\sigma^t \\ \mathbf{D}^t &= \mathbf{D}^{t-\Delta t} + \Delta\mathbf{D}^t \end{aligned} \quad (2.24)$$

The polarization state P_3^t is a function of the coercive electric field that depends on the current compressive stress σ_{33}^t . In the displacement based FE, the current value of stresses need to be determined from the strain and electric field inputs. In this study, during the incremental solution at the material level, the coercive electric field at current time is obtained as:

$$E_c = \begin{cases} E_c(E_c^o, \sigma_{33}^{t-\Delta t}), \sigma_{33}^{t-\Delta t} < 0.0 \\ E_c^o, \sigma_{33}^{t-\Delta t} \geq 0.0 \end{cases} \quad (2.25)$$

Thus, the calculated consistent tangent stiffness, piezoelectric constant, and dielectric constants in equation (2.24) depend on the current electric field E_3^t and stress from

the previous time increment $\sigma_{33}^{t+\Delta t}$. Instead of performing an iteration at the material level, the correction due to a linearized stress is performed through an iteration scheme at the structural level.

2.2.2 Solution at the Structural Level

The governing equations for the electro-mechanical deformation under a quasi-static loading and small-deformation gradients are formed at the structural level by imposing the energy balance equations, which in absences of the body forces and body charges are:

$$\begin{aligned}\int_V \sigma_{ij}^t d\varepsilon_{ij}^t dV &= \int_A t_i^t du_i^t dA \\ \int_V D_i^t dE_i^t dV &= \int_A q_s^t d\varphi^t dA\end{aligned}\quad (2.26)$$

where t and q_s are the surface traction and surface charge, respectively. Using the strain and electric field defined in equations (2.13), respectively, the linearized constitutive model in equation (2.19), and the principle of virtual work, the energy balance equations for one element are:

$$\begin{aligned}\int_V d\mathbf{U}^{nT} \mathbf{B}^{uT} [\tilde{\mathbf{C}} \mathbf{B}^u \mathbf{U}^n - \tilde{\mathbf{e}}'^T \mathbf{B}^\varphi \Phi^n] dV &= \int_A d\mathbf{U}^{nT} \mathbf{N}^T \mathbf{t} dA \\ \int_V d\Phi^{nT} \mathbf{B}^{\varphi T} [\tilde{\mathbf{e}} \mathbf{B}^u \mathbf{U}^n + \tilde{\kappa}' \mathbf{B}^\varphi \Phi^n] dV &= \int_A d\Phi^{nT} \mathbf{N}^T q_s dA\end{aligned}\quad (2.27)$$

Equation (2.27) can be rewritten as:

$$\begin{aligned}d\mathbf{U}^{nT} \int_V \mathbf{B}^{uT} \tilde{\mathbf{C}} \mathbf{B}^u dV \mathbf{U}^n - \int_V \mathbf{B}^{uT} \tilde{\mathbf{e}}'^T \mathbf{B}^\varphi dV \Phi^n &= d\mathbf{U}^{nT} \int_A \mathbf{N}^T \mathbf{t} dA \rightarrow \\ \mathbf{K}^{uu} \mathbf{U}^n - \mathbf{K}^{u\varphi} \Phi^n &= \mathbf{F}^M \\ d\Phi^{nT} \int_V \mathbf{B}^{\varphi T} \tilde{\mathbf{e}} \mathbf{B}^u dV \mathbf{U}^n + \int_V \mathbf{B}^{\varphi T} \tilde{\kappa}' \mathbf{B}^\varphi dV \Phi^n &= d\Phi^{nT} \int_A \mathbf{N}^T q_s dA \rightarrow \\ \mathbf{K}^{\varphi u} \mathbf{U}^n + \mathbf{K}^{\varphi\varphi} \Phi^n &= \mathbf{F}^E\end{aligned}\quad (2.28)$$

In order to obtain solutions for the displacements and electric potential at the element level the Gaussian quadrature method is used for the spatial integration. At each time increment the linearized relations in equations (2.20)-(2.24) are used as a starting point for obtaining trial solutions to the nodal displacements and electric potential. The Newton-Raphson iterative method is then used to correct for the errors from the linearization. After assembly over all elements the overall equilibrium equation can be obtained with the residual vector at time t :

$$\mathbf{R}^t = \begin{Bmatrix} \mathbf{R}^{u,t} \\ \mathbf{R}^{\varphi,t} \end{Bmatrix} = \begin{Bmatrix} \mathbf{F}^{M,t} - (\mathbf{K}^{uu,t}\mathbf{U}^{n,t} - \mathbf{K}^{u\varphi,t}\Phi^{n,t}) \\ \mathbf{F}^{E,t} - (\mathbf{K}^{\varphi u,t}\mathbf{U}^{n,t} + \mathbf{K}^{\varphi\varphi,t}\Phi^{n,t}) \end{Bmatrix} \quad (2.29)$$

The above equation is solved when the boundary conditions are prescribed to the structures:

$$\begin{aligned} \mathbf{t} &= \bar{\sigma}\mathbf{n} & \partial S_t \\ q_s &= \bar{\mathbf{D}}\mathbf{n} & \partial S_q \\ \mathbf{u} &= \bar{\mathbf{u}} & \partial S_u \\ \varphi &= \bar{\varphi} & \partial S_\varphi \end{aligned} \quad (2.30)$$

where \mathbf{n} is the unit outward normal vector on the boundaries ∂S_t and ∂S_q . It is also necessary for the boundaries to satisfy the following conditions:

$$\begin{aligned} \partial S_t \cup \partial S_u &= \partial S & \partial S_t \cap \partial S_u = 0 \\ \partial S_q \cup \partial S_\varphi &= \partial S & \partial S_q \cap \partial S_\varphi = 0 \end{aligned} \quad (2.31)$$

It is noted that at the element level, the nodal displacements and electric potentials are taken as the independent field variables $\{\mathbf{X}^t\} = \left\{ \mathbf{U}^{n,t} \quad \Phi^{n,t} \right\}$ and in order to minimize the residual vector at each time due to the trial linearized solution, the independent field variables need to be corrected. Let k be an iterative counter, the

corrected field variables at time t is:

$$\{\mathbf{X}^{t,k+1}\} = \{\mathbf{X}^{t,k}\} + \left[\frac{\partial \mathbf{R}^{t,k}}{\partial \mathbf{X}} \right]^{-1} \mathbf{R}^{t,k} \quad (2.32)$$

and

$$\tilde{\mathbf{K}}^{t,k} \equiv \left[\frac{\partial \mathbf{R}^{t,k}}{\partial \mathbf{X}} \right] = \begin{bmatrix} -\mathbf{K}^{uu,t,k} \mathbf{K}^{u\varphi,t,k} \\ -\mathbf{K}^{\varphi u,t,k} - \mathbf{K}^{\varphi\varphi,t,k} \end{bmatrix} \quad (2.33)$$

The numerical algorithm at the structural and material levels within each time increment is summarized as follows:

1. Input variables $\mathbf{U}^{n,t-\Delta t}, \Phi^{n,t-\Delta t}, \mathbf{F}^{M,t-\Delta t}, \mathbf{F}^{E,t-\Delta t}, \tilde{\mathbf{K}}^{t-\Delta t}, Q^{t-\Delta t}, q^{t-\Delta t}, P_c$
2. Determine trial nodal variables at time t : $\mathbf{U}^{n,t,k}, \Phi^{n,t,k}; k = 0$
3. Iterate for $k=0,1,2,\dots$ (k =iteration counter)
 - (a) Calculate $\mathbf{E}^{t,k}, P_3^{t,k}, \mathbf{g}^{t,k}, \tilde{\mathbf{B}}^{t,k}, \Delta\sigma^{t,k}, \Delta\mathbf{D}^{t,k}, \sigma^{t,k}, \mathbf{D}^{t,k}, \mathbf{F}^{M,t,k}, \mathbf{F}^{E,t,k}, \tilde{\mathbf{K}}^{t,k}$
 - (b) Define residual (equation 2.29) $\mathbf{R}^{t,k}$ and check for $\|\mathbf{R}^{t,k}\| \leq Tol$; yes then go to 4 else
 - (c) Correct the nodal displacement and electric potential (equation (2.30)) and go to 3.1
4. Output variables $\mathbf{U}^{n,t}, \Phi^{n,t}, \mathbf{F}^{M,t}, \mathbf{F}^{E,t}, \tilde{\mathbf{K}}^t$ and update history variables Q^t, q^t, P_c

2.3 Numerical Implementation

This section presents analyses of the electro-mechanical response of ferroelectric materials and structural components undergoing coupled mechanical loading and electric field. Experimental data on the polarization switching response of PZT 51, reported by Fang and Li [44], are used to validate the constitutive model. Parametric studies on understanding the effects of different boundary conditions and loading

rates on the electro-mechanical response of the ferroelectric materials are presented. Finally the FE method is used to perform time-dependent analyses of smart structural components undergoing various histories of mechanical loading and electric fields.

2.3.1 Verification of the constitutive model

The electro-mechanical constitutive model in equation (2.8) is validated using the experimental data of PZT51 reported by Fang and Li [44]. Figure 2.3a shows the polarization hysteretic response ($D_3 - E_3$) of PZT-51 subject to a cyclic electric field at zero stress. The amplitude of the electric field is 1.2 MV/m with a frequency of 1 Hz. The test started from an unpolarized condition and with increasing the electric field the polarization takes place. The loop in the first cycle is higher by about 0.03 C/m^2 . After several cycles, the saturated polarization converges to a constant value, which shows a slightly smaller value than the one in the first cycle. The material parameters for the time-dependent polarization in equations (2.3), (2.4), and (2.8) are calibrated from this hysteretic polarization response. The time-dependent polarization model is shown to be capable in capturing the hysteretic polarization response. The material parameters of the PZT-51 used in the simulation are reported in Table 2.1. The corresponding butterfly hysteretic responses during the first and saturated cycles at zero stresses are shown in Figure 2.3b. It is seen from Figure 2.3b that at the coercive electric fields the strains from the experimental tests are nonzero, which is about $500 \mu\epsilon$ higher. This might be due to the accumulated strain from the first cycle loading.

In this study, the parameter C_1 in equation (2.12) is calibrated from the saturated butterfly curve in Figure 2.4a after shifting the strain response obtained from the simulation $500 \mu\epsilon$ higher. The piezoelectric constants measured at the rema-

net polarization are obtained from Fang and [44] and the permittivity constants at the remanent polarization are taken from [56]. It is noted that the piezoelectric constants at the remanent polarization used in equation (2.8) are determined from $\mathbf{g}^r = \kappa^{r-1} \mathbf{d}^r$. Tables 2.2 and 2.3 report the electro-mechanical coupling parameters and elastic constants, respectively, for PZT-51. The corresponding transverse butterfly strain response is shown in Figure 2.4b. The nonlinear electro-mechanical coupling model is capable of simulating the hysteretic polarization switching electro-mechanical response. Next, the hysteretic responses due to a cyclic electric field at various constant compressive stresses are simulated. Figures 2.5 and 2.6 illustrate the polarization and butterfly strain responses under a cyclic electric field with amplitude of 1.2 MV/m and frequency of 1 Hz and various compressive stresses: 5-30 MPa. From the experimental evidences the coercive electric fields vary with the compressive stresses, which can be described by the following function:

$$E_c = E_c^o - 0.0041 |\sigma_{33}^t| \quad (2.34)$$

The material parameters reported in Tables 2.1 and 2.2 are used in the simulation. Good model predictions are shown for the response up to 20 MPa compressive stresses and at the compressive stress 30 MPa, the model over-predicts the polarization and strain responses. The effect of compressive stresses in reducing the overall axial strain and electric displacement is due to the electro-mechanical coupling $4g_{n33}^t \kappa_{nm} g_{m33}^t \sigma_{33}^t$ and $2\kappa_{3m} g_{m33}^t \sigma_{33}^t$, respectively, with indices **m** and **n** vary from 1 to 3. Fang and Li [44] discussed that when the ferroelectric materials are subjected to compressive stresses higher than the coercive stress σ_c of the materials, polarization switching occurs, which can alter the material properties. Figures 2.5d and 2.6d indicate that under a compressive stress of 30 MPa the polarization switching has

occurred in PZT-51 which is shown by a significantly low strain response. In order to incorporate the effect of polarization switching due to high compressive stresses, the piezoelectric constants in Eq. (2.12) is used. This study used the hysteretic responses under a compressive stress 40 MPa (Figures 2.7b and 2.8b) to calibrate the material parameters when the polarization switching occurs due to high compressive stresses. The coercive stress is taken as 25 MPa. In this study an attempt is made to recalibrate the parameters corresponding to the irreversible polarization. Table 2.6 presents the calibrated material parameters above the coercive stress limit. The hysteretic responses under compressive stresses 30-80 MPa are shown in (Figures 2.7 and 2.8). Relatively good predictions of the polarization and butterfly strains are observed.

2.3.2 Structural Analyses

The PZT-51 is now used to induce deformations in a fiber reinforced laminated composite plate. Consider a composite plate (host structure) of $100 \times 50 \times 1 \text{ mm}^3$, shown in Figure 2.9, with four PZT patches. Each PZT patch has a dimension of $10 \times 10 \times 1 \text{ mm}^3$. The properties of the PZT are given in Tables 1-4, while the composite plate is made of a glass fiber composite. The composite plate is assumed linear elastic with the following elastic material properties: $E=36000 \text{ MPa}$, $\nu=0.25$ in the longitudinal fiber axis. The plate is clamped along one of its 50 mm side surface and the PZT patches are bonded perfectly to the host structure. The potential on the surfaces of the PZT patches that are in contact to the host structure is grounded to zero. The PZT patches are uniformly subjected to the potential gradient through their thickness $E_3(t) = 1.2 \sin(2\pi ft) \text{ MV/m}$ so that they experience expansion in their planar direction, thus inducing bending to the composite plate. Figure 2.10 depicts the lateral displacement measured at the mid section of the free end due to the

input electric field applied uniformly to the four PZT patches, which show vibration of the composite plate. It is seen that the highest deformation occurs at the first quarter cycle, when the electric field reaches 1.2 MV/m (point A). Upon removal of the electric field, the remanent deformation is shown (point B) and when the electric field reaches the coercive limit of the PZT patches no deformation is shown in the plate (point C) due to depolarization of the PZT patches. Continuing applying the electric field till it reaches the lowest peak -1.2 MV/m (point D) trigger bending in the composite plate. It is also seen that due to the time-dependent effect, the highest displacement is at the first quarter cycle and after several cycles, saturation in the butterfly displacement loop is achieved. The corresponding deformed shapes of the composite plate at several instant of times during the first cycle are illustrated in Figure 2.11. It is also possible to create different deformed shapes by considering various histories of electric field inputs. For example, to induce twisting of the plate different electric field inputs can be applied to the four patches. The tip-deflection, illustrated in Figure 2.12, is generated by prescribing the following electric field input to the PZT patches 3 and 4, and to the patches 1 and 2.

The effect of time dependent response of a viscoelastic host structures with piezoelectric patches on the overall mechanical deflection is examined. Figure 2.13 illustrate the lateral deflection in smart beams activated by applying electric field to the patches. The patches are activated with the same time function with the frequency of 0.1Hz. The elastic host materials is made of a linear elastic material with $E = 2710.03\text{ MPa}$ and $\nu = 0.35$. In the case of viscoelastic host structure the instantaneous elastic modulus is taken as $E = 2710.03\text{ MPa}$ while the time dependent material properties are given in Table 2.5. It is seen that lateral deflections of the elastic and visco-elastic host structure are quite different in these two different cases. This could be due to delay of the host structure for responding to internal stresses.

This delay is caused by viscoelastic response of the host structure.

A loop can be observed in the response of beam as it is shown in Figure 2.13. As we pay close attention Figure 2.13 we see small loops forming the top left of the curve. This form of response is observable in the situation where there are more than one source of hysteresis response. A looping phenomenon is evident near the extremes of the main hysteresis loop in Piezoelectric Microfiber Composite (MFC) actuators [76]. The looping is also observed as distortion of hysteresis loop while resistor is added to actuation circuit of PZT ($BaTiO_3$) as phase shift is introduced to experiment [33]. From observation of the experimental data and also the prediction of structural response in the simulation in Figure 2.13 it can be concluded that looping happens due to superposition of two different hysteresis phenomena. As an instance in the case of tip displacement of Piezoelectric Microfiber Composite (MFC) actuators [76] there are two sources of hysteresis. First is the hysteresis due from electromechanical coupling phenomena between electric field and mechanical response. Second source is the hysteresis from mechanical response between stress and strain rate that happens due to viscoelasticity.

Table 2.1: Material parameters for the time-dependent polarization of PZT-51

E_c^o	κ_0	κ_1	τ_1	λ	n	μ	ω
MV/m	pF/m	pF/m	sec	$\mu F/m$	$\mu F/m$	$\mu F/m$	
0.67 ²	70	225	1	0.35	3	1.6	4

Table 2.2: Electro-mechanical coupling parameters for PZT-51

d_{333}^r $(\times 10^{-12} m/V)$	d_{311}^r	κ_{11}^r $(\times 10^{-9} F/m)$	κ_{33}^r	P_r C/m^2	C_1 C/m^2
1520 ³	570	38	42	0.194	0.19

Table 2.3: Elastic constants for PZT-51 [56]

$E_{11} = E_{22}$	E_{33}	$G_{12}(GPa)$	$G_{13} = G_{23}$	ν_{12}	$\nu_{13} = \nu_{23}$
34.48	33	13.19	12.37	0.307	0.334

Table 2.4: Material parameters above the coercive stress limit

$\sigma_c(MPa)$	C_2	$\lambda(\times 10^{-6} F/m)$	n	$\mu(\times 10^{-6} F/m)$	ω
25	0.3	0.4	3	1.1	4

Table 2.5: Prony series for viscoelastic host structure

J_n	λ_n
6	2.10E-05
1	2.16E-05
0.1	1.18E-05
0.01	1.59E-05
0.001	2.16E-05
0.0001	2.01E-05
1.00E-05	6.60E-05

Table 2.6: Material parameters above the coercive stress limit

$\sigma_c(MPa)$	C_2	$\lambda(\times 10^6 F/m)$	n	$\mu(\times 10^{-6} F/m)$	ω
25	0.3	0.4	3.0	1.1	4

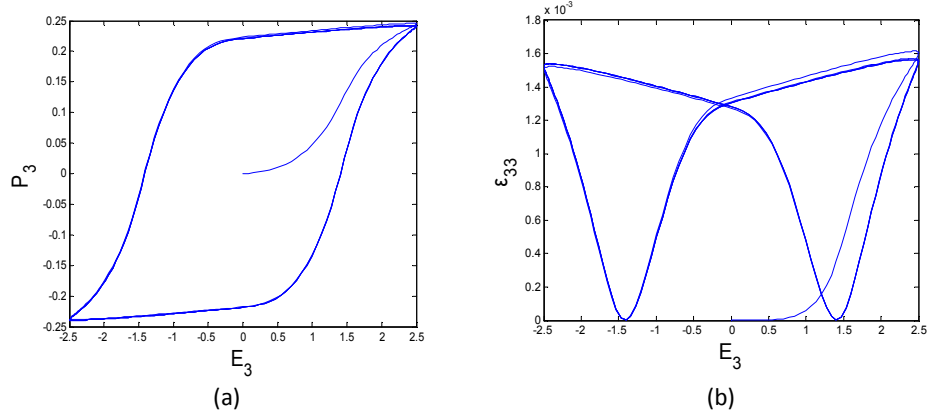


Figure 2.1: Major hysteresis loops in a piezoelectric sample: a) polarization response and b) corresponding strain response

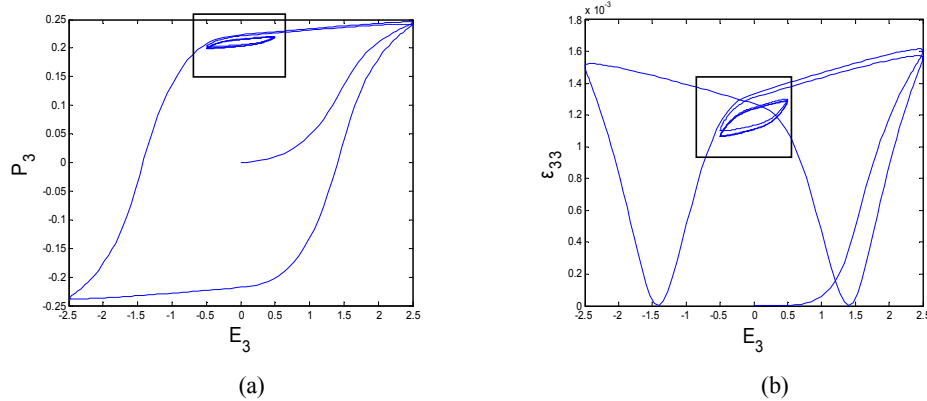


Figure 2.2: Minor hysteresis loops in a polarized piezoelectric sample: a) polarization response and b) corresponding strain response

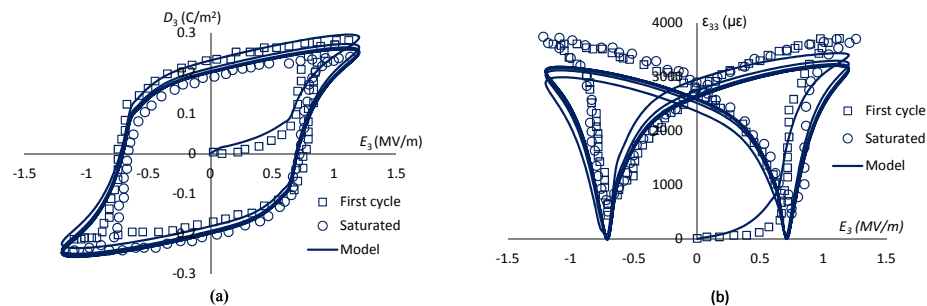


Figure 2.3: Hysteresis polarization and butterfly strain responses for PZT51 at zero stress

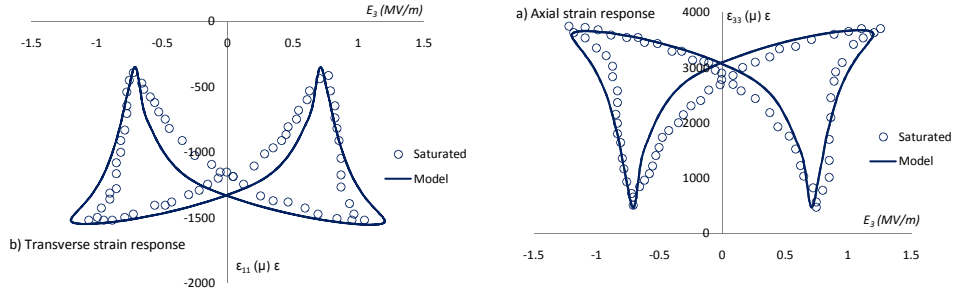


Figure 2.4: Saturated strain responses for PZT51 at zero stress

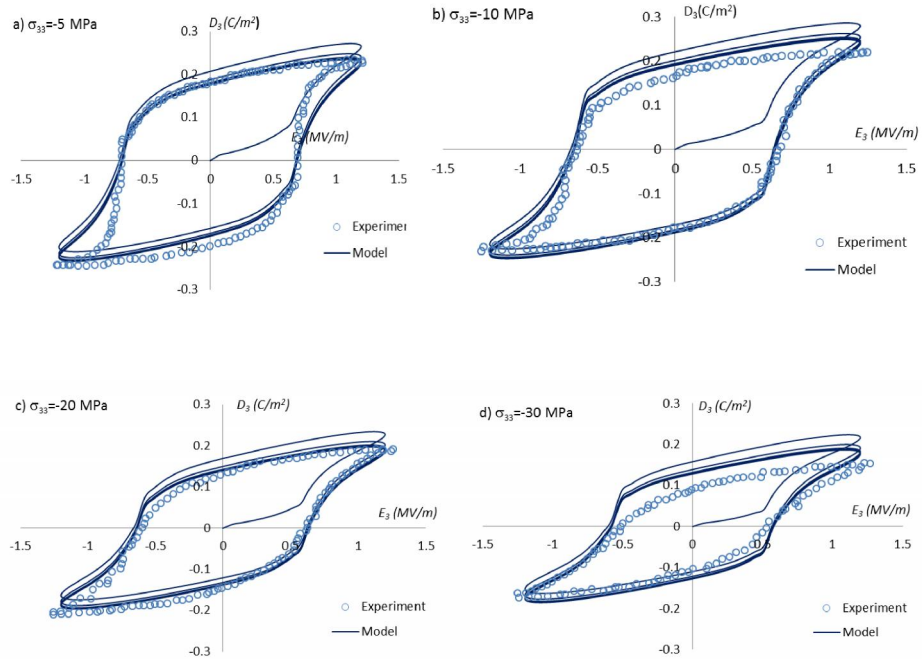


Figure 2.5: Hysteresis polarization responses under constant compressive stresses

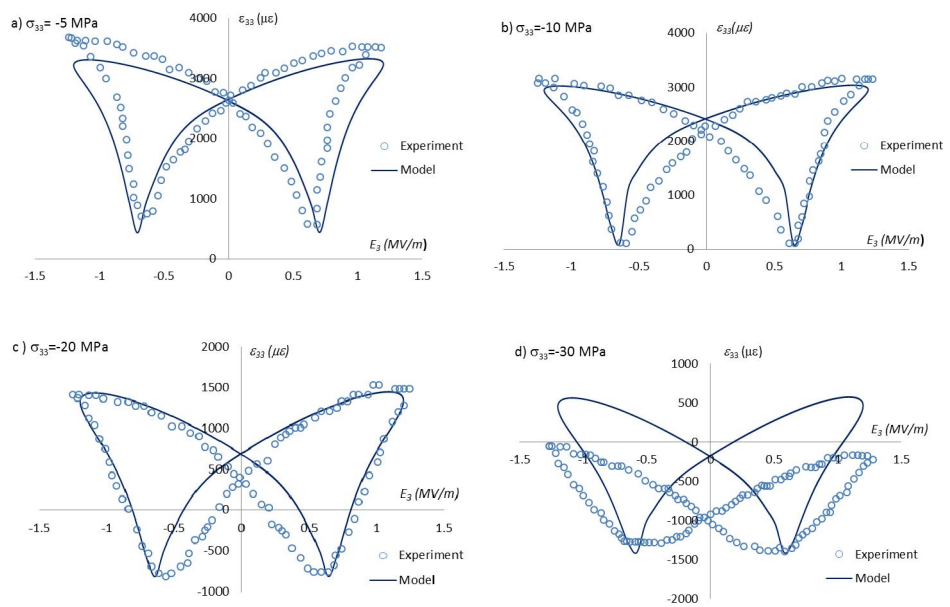


Figure 2.6: Butterfly strain responses under constant compressive stresses

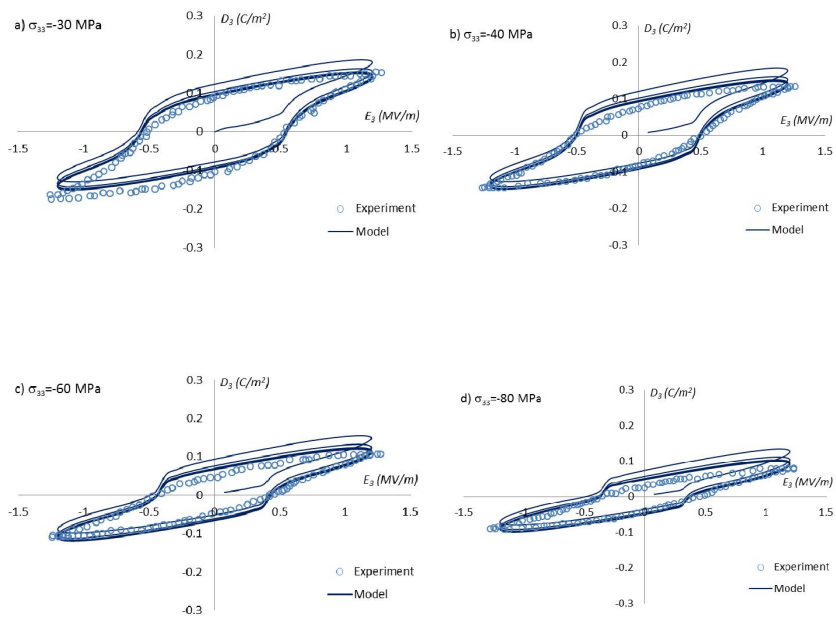


Figure 2.7: Hysteresis polarization responses under constant compressive stresses above the coercive stress

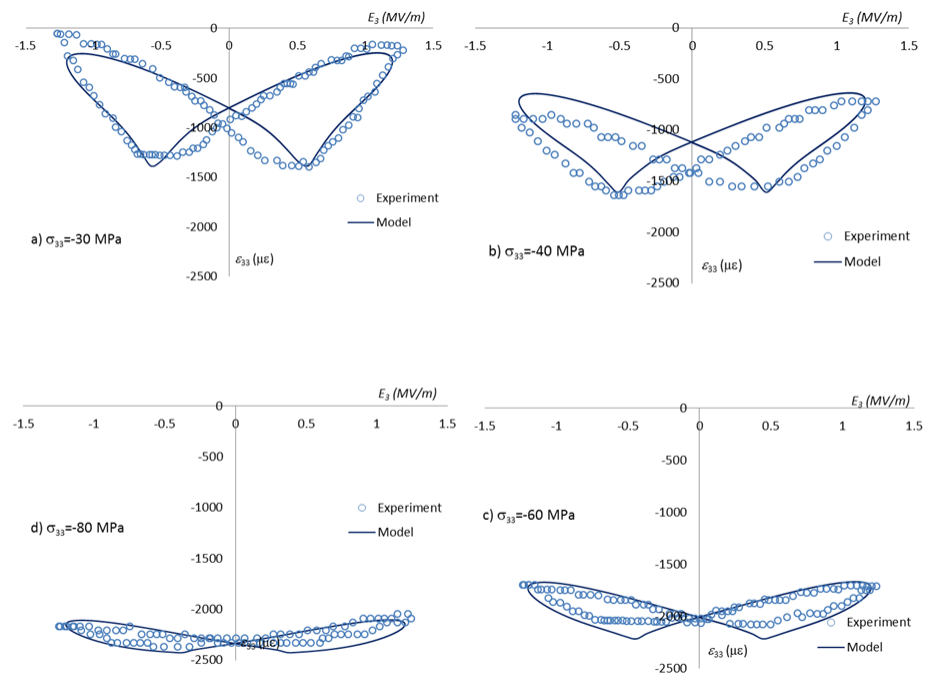


Figure 2.8: Butterfly strain responses under constant compressive stresses above the coercive stress

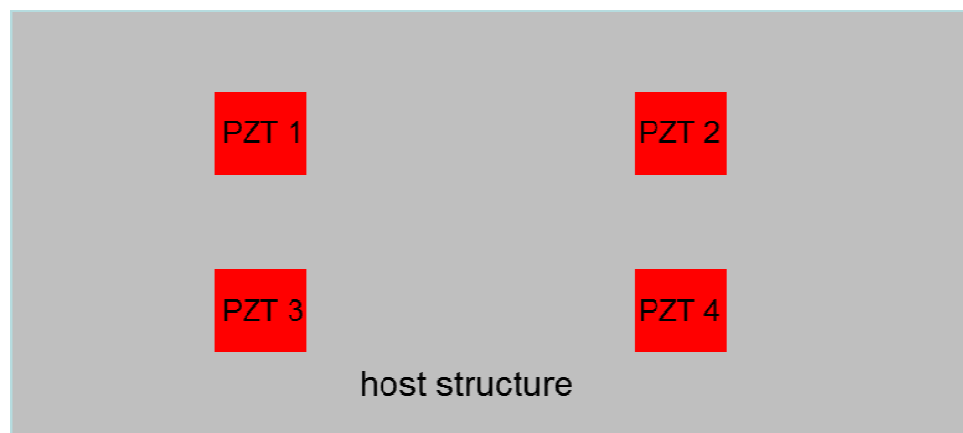


Figure 2.9: Active composite plate with PZT patches

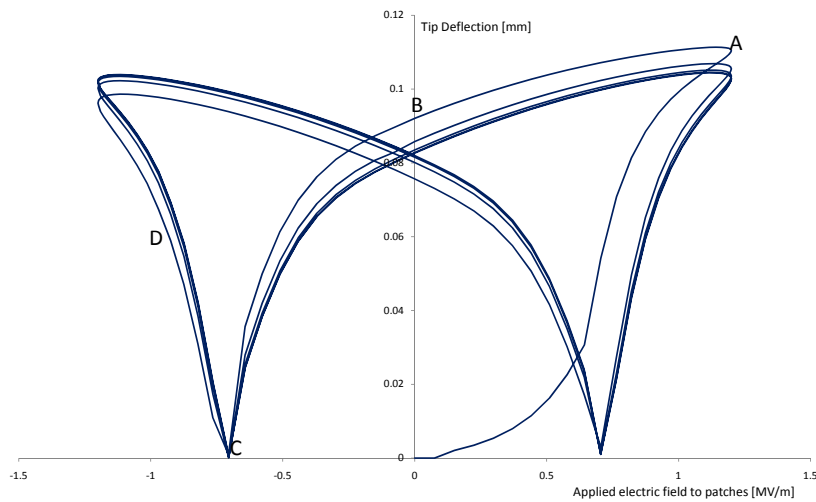


Figure 2.10: Tip deflection of the cantilever plate due to uniform cyclic electric fields applied to the piezoelectric patches

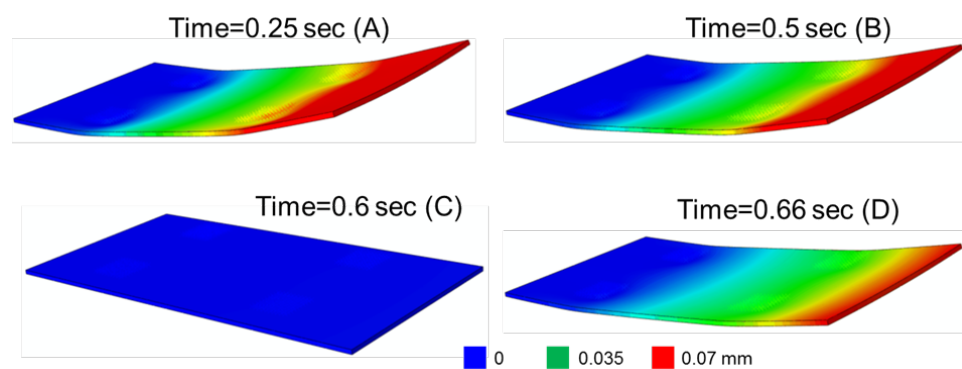


Figure 2.11: The corresponding deformed shape of an active cantilever plate due to a uniform cyclic electric field applied to the piezoelectric patches

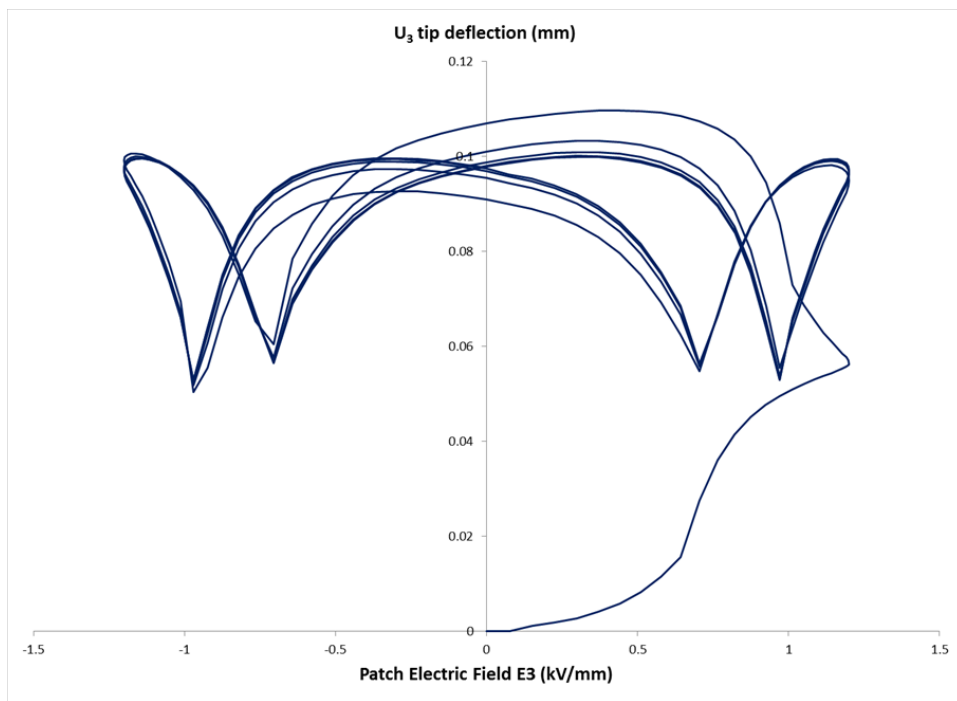


Figure 2.12: Tip deflection of the twisting cantilever plate due to a non-uniform cyclic electric field applied to the piezoelectric patches

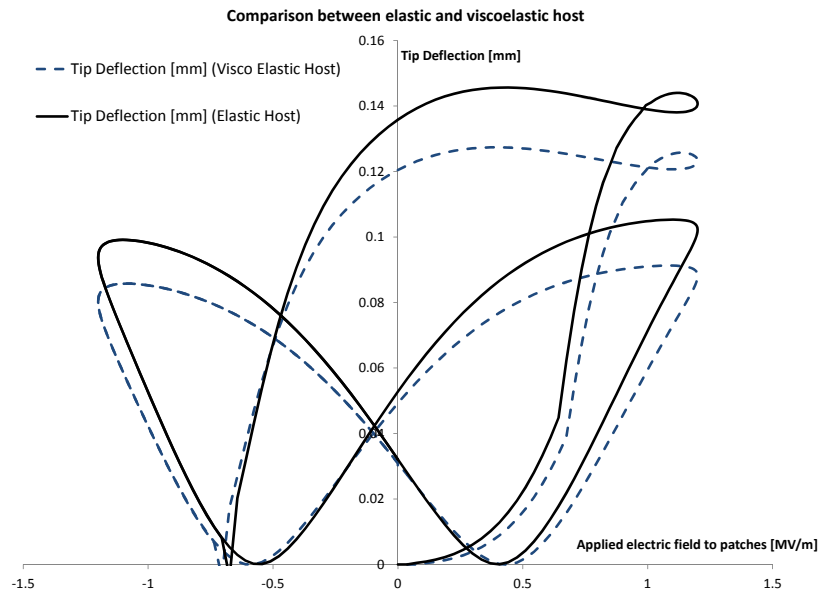


Figure 2.13: The comparison between viscoelastic and elastic materials as host structure

3. MINOR LOOP CONSTITUTIVE MODEL

This chapter discusses a time-dependent constitutive model for polarized piezoelectric materials with an intention to capture minor hysteretic response. The model is suitable for piezoelectric ceramics, which experience small deformation gradient, and can sustain large electric fields. It is assumed that the loading is within a quasi-static condition so that we neglect the inertia effect on the electro-mechanical response and ignore the energy dissipation effect. The constitutive model for a polarized ferroelectric ceramics is obtained from:

$$\begin{aligned}\sigma_{ij} &= \frac{\partial \Psi_e}{\partial \varepsilon_{ij}}|_{E_k} \\ D_k &= -\frac{\partial \Psi_e}{\partial E_k}|_{\varepsilon_{ij}} \\ \Psi_e &= \hat{\Psi}_e(E_k, \varepsilon_{ij})\end{aligned}\tag{3.1}$$

where $\hat{\Psi}_e(E_k, \varepsilon_{ij})$ is the thermodynamics function expressed in terms of the electric field vector E_k and strain tensor ε_{ij} . The notations $|_{E_k}$ and $|_{\varepsilon_{ij}}$ mean that the field variables are evaluated at constant E_k and ε_{ij} , respectively. The thermodynamics potentials are often expressed in a Taylor series expansion of the independent field variables that can include higher order terms. Following the constitutive model of Tiersten [73] for active materials undergoing large electric fields and small strains, the free energy $\hat{\Psi}_e(E_k, \varepsilon_{ij})$ at an isothermal condition is then expressed as:

$$\begin{aligned}\hat{\Psi}_e = & \sum_{i,j,k,l=1}^3 \frac{1}{2} C_{ijkl} \varepsilon_{ij} \varepsilon_{kl} - \sum_{k,i,j=1}^3 e_{kij} \varepsilon_{ij} E_k - \sum_{k,j=1}^3 \frac{1}{2} \kappa_{kj} E_j E_k - \\ & \sum_{i,j,k,l=1}^3 \frac{1}{2} \hat{b}_{klij} E_k E_l \varepsilon_{ij} + \sum_{i,j,k,l=1}^3 \frac{1}{6} \chi_{kij} E_i E_j E_k + H.O.T\end{aligned}\tag{3.2}$$

where C_{ijkl} are the components of the elastic stiffness, e_{kij} represents the components of electro mechanical coupling tensor and κ_{kj} are the components of the electric permittivity tensor. The field variables are the stress σ_{ij} , strain ε_{kl} , electric displacement D_k , and electric field E_j . Moreover, \hat{b}_{klij} and χ_{kij} are the components of the fourth-order electro-mechanical tensor and third-order electric permeability tensor, respectively. Equation (3.2) can be further expanded to include fourth, fifth, etc. order terms of electric field. In such case, additional material parameters are required. It is also possible to consider only the odd or even terms of electric field in order to capture response of the material. Using equations (3.2) and (3.1) the stress and electric displacement for piezoelectric materials undergoing small strain and large electric field are written as:

$$\begin{aligned}\sigma_{ij} &= \sum_{k,l=1}^3 C_{ijkl} \varepsilon_{kl} - \sum_{k=1}^3 e_{kij} E_k - \sum_{k,l=1}^3 \frac{1}{2} \hat{b}_{ijkl} E_k E_l \\ D_k &= \sum_{i,j=1}^3 e_{kij} \varepsilon_{ij} + \sum_{j=1}^3 \kappa_{kj} E_j + \sum_{i,j,l=1}^3 \hat{b}_{klij} E_l \varepsilon_{ij} + \frac{1}{2} \sum_{i,j=1}^3 \chi_{kij} E_i E_j\end{aligned}\quad (3.3)$$

$$(i, j, k = 1 \dots 3)$$

When the nonlinear terms are neglected, a linear electro-mechanical response of piezoelectric material [43] is then obtained:

$$\begin{aligned}\sigma_{ij} &= \sum_{k,l=1}^3 C_{ijkl} \varepsilon_{kl} - \sum_{k=1}^3 e_{kij} E_k \\ D_k &= \sum_{i,j=1}^3 e_{kij} \varepsilon_{ij} + \sum_{j=1}^3 \kappa_{kj} E_j\end{aligned}\quad (3.4)$$

$$(i, j, k = 1 \dots 3)$$

In the above expression, strains and electric fields are chosen as the independent field variables. In case of a finite element analysis, displacements u_i and electric

potential Φ are defined at nodes within finite elements. The field variables in the constitutive equations are obtained directly from the displacements u_i and electric potential Φ . The strain displacement relationship based on infinitesimal strain theory is defined as:

$$\varepsilon_{kl} = \frac{u_{k,l} + u_{l,k}}{2} \quad (3.5)$$

where subscript with comma $(,l)$ means derivative with respect to x_l ($\frac{\partial}{\partial x_l}$). The electric field is defined as:

$$E_j = -\Phi_{,j} \quad (3.6)$$

For a linear electro mechanical response given in equation (3.4) the derivatives of the stress and electric displacement with respect to the independent field variables result in the following material parameters:

$$\begin{aligned} \frac{\partial \sigma_{ij}}{\partial \varepsilon_{kl}} &= C_{ijkl} \\ \frac{\partial \sigma_{ij}}{\partial E_k} &= -e_{kij} \\ \frac{\partial D_k}{\partial \varepsilon_{ij}} &= e_{kij} \\ \frac{\partial D_k}{\partial E_i} &= \kappa_{ki} \end{aligned} \quad (3.7)$$

For the nonlinear electro-mechanical model such as in equation (3.3), the derivatives of the stress and electric displacement with respect to the independent field variables are:

$$\begin{aligned}
\frac{\partial \sigma_{ij}}{\partial \varepsilon_{kl}} &= C_{ijkl} \\
\frac{\partial \sigma_{ij}}{\partial E_k} &= -e_{kij} - \sum_{l=1}^3 \hat{b}_{klij} E_l \\
\frac{\partial D_k}{\partial \varepsilon_{ij}} &= e_{kij} + \sum_{l=1}^3 \hat{b}_{klij} E_l \\
\frac{\partial D_k}{\partial E_i} &= \kappa_{ki} + \sum_{m,n=1}^3 \hat{b}_{kimn} \varepsilon_{mn} + \sum_{j=1}^3 \chi_{kij} E_j
\end{aligned} \tag{3.8}$$

Tiersten [73] also discussed an alternative expression of the constitutive model with nonlinear electric field and small strain when stress and electric field are taken as the independent field variables

$$\begin{aligned}
\varepsilon_{ij} &= \sum_{k,l=1}^3 S_{ijkl} \sigma_{kl} + \sum_{k=1}^3 d_{kij} E_k + \sum_{k,l=1}^3 \frac{1}{2} f_{ijkl} E_k E_l \\
D_k &= \sum_{i,j=1}^3 d_{kij} \sigma_{ij} + \sum_{j=1}^3 \kappa_{kj}^\sigma E_j + \sum_{i,j,l=1}^3 f_{klij} E_l \sigma_{ij} + \frac{1}{2} \sum_{i,j=1}^3 \chi_{kij}^\sigma E_i E_j
\end{aligned} \tag{3.9}$$

$(i, j, k = 1 \dots 3)$

The elastic compliances, S_{ijkl} , piezoelectric constant, d_{kij} , and nonlinear electroelastic constants, f_{ijkl} are:

$$\begin{aligned}
S_{ijkl} &= C_{ijkl}^{-1} \\
d_{ijk} &= \sum_{m,n=1}^3 e_{imn} S_{mnjk} \\
f_{ijkk} &= \sum_{m,n=1}^3 \hat{b}_{ijmn} S_{mnkl}
\end{aligned} \tag{3.10}$$

The second- and third-order electric permeability constants are measured at zero or constant stresses:

$$\begin{aligned}\kappa_{ij}^\sigma &= \hat{\kappa}_{ij} + \sum_{m,n=1}^3 e_{imn} d_{jmn} \\ \chi_{ijk}^\sigma &= \chi_{ijk} + \sum_{m,n=1}^3 e_{imn} f_{jkmn}\end{aligned}\tag{3.11}$$

In analogy to the time-dependent deformation of viscoelastic materials, the non-linear electro-elastic model developed by Tiersten [73] is extended to include time-dependent material parameters. There have been several integral models developed to describe nonlinear viscoelastic behavior: modified superposition principle (Findley and Lai, [24]), multiple integral model (Green and Rivlin [28]), finite strain integral models (Pipkins and Rogers [59]; Rajagopal and Wineman [79]), single integral models (Pipkins and Rogers [59]; Schapery [63]), and quasi linear viscoelastic model (Fung [26]). The work by Green and Rivlin [28] provides the fundamental framework for nonlinear viscoelastic response based on continuum mechanics. It is assumed that small changes in the input field variables cause only small changes in the corresponding output field variables; this can be approximated by using continuous functions in order to express the output field variables in terms of history of inputs and time-dependent material properties. For a nonlinear viscoelastic material, Green and Rivlin [28] formed a sum of multiple integrals of the polynomial functions to incorporate history of input variables in predicting output at current time. This study considers two integral approaches in modelling nonlinear time-dependent electro-nechabical response of piezo electric, namely multiple integral and single integral based on quasi linear viscoelastic representations.

3.1 Multiple Time Integral Method

The constitutive equations (3.3) and (3.9) is expressed in terms of polynomial functions of independent field variables. In analogy to the correspondence between

elastic and viscoelastic materials, the nonlinear electro-elastic equations of Tiersten ([73]) is modified to include the time-dependent effect (for non-aging materials):

$$\begin{aligned}
\varepsilon_{ij}(t) &= \int_{s=0^-}^t \sum_{k,l=1}^3 S_{ijkl}(t-s) \frac{d\sigma_{kl}}{ds} ds + \int_{s=0^-}^t \sum_{k=1}^3 d_{kij}(t-s) \frac{dE_k}{ds} ds \\
&\quad + \int_{s_1=0^-}^t \int_{s_2=0^-}^t \sum_{k,l=1}^3 \frac{1}{2} f_{ijkl}(t-s_1)(t-s_2) \frac{dE_k}{ds_1} \frac{dE_l}{ds_2} ds_1 ds_2 \\
D_k &= \int_{s=0^-}^t \sum_{i,j=1}^3 d_{kij}(t-s) \frac{d\sigma_{kl}}{ds} ds + \int_{s=0^-}^t \sum_{j=1}^3 \kappa_{kj}^\sigma \frac{dE_k}{ds} ds + \\
&\quad + \int_{s_1=0^-}^t \int_{s_2=0^-}^t \sum_{i,j,l=1}^3 f_{klij}(t-s_1)(t-s_2) \frac{dE_l}{ds_2} \frac{d\sigma_{ij}}{ds_2} ds_1 ds_2 \\
&\quad + \int_{s_1=0^-}^t \int_{s_2=0^-}^t \sum_{k,l=1}^3 \frac{1}{2} \chi_{kij}^\sigma(t-s_1)(t-s_2) \frac{dE_i}{ds_1} \frac{dE_j}{ds_2} ds_1 ds_2 \\
&\quad (i, j, k = 1 \dots 3)
\end{aligned} \tag{3.12}$$

It is also possible to include higher order terms of the electric field. In order to graphically visualize the linear and nonlinear kernel functions of time, a one-dimensional multiple integral forms (up to the second order) is considered:

$$\begin{aligned}
R(t) &= \int_{s=0^-}^t \psi_1(t-s) \frac{dI(s)}{ds} ds \\
&\quad + \int_{s_1=0^-}^t \int_{s_2=0^-}^t \psi_2(t-s_1, t-s_2) \frac{dI(ds_1)}{ds_1} ds_1 \frac{dI(s_2)}{s_2} ds_2
\end{aligned} \tag{3.13}$$

where $R(t)$ is the corresponding output at current time t , $I(s)$ is the input history prescribed at $0 \leq s \leq t$, $\psi_1(t)$ and $\psi_2(t, t)$ are the two kernel functions. When the kernels are assumed to increase with time, Figure 3.1 illustrates the linear and second order kernel functions of time (see Findley et al. [24] for a detailed explanation). It is also assumed that the material response is unaltered by an arbitrary shift of the

time scale, so that the following functions can be used for the two kernels in equation (3.13)

$$\begin{aligned}\psi_1(t-s) &= A_0 + A_1(1 - e^{-(t-s)/\tau_1}) \\ \psi_2(t-s_1, t-s_2) &= B_0 + B_1(2 - e^{-(t-s_1)/\lambda_1} - e^{-(t-s_2)/\lambda_2}) + \\ &\quad B_2(1 - e^{-(t-s_1)/\lambda_1})(1 - e^{-(t-s_2)/\lambda_2})\end{aligned}\quad (3.14)$$

where $A_0, A_1, B_0, B_1, \tau_1, \lambda_1, \lambda_2$ are the material parameters that need to be determined from experiments. A set of experiments may be performed by applying the input variables at different times, say at $t = 0$ and $t = s_1$. The main disadvantage of the multiple integral forms is in difficulties characterizing the material parameters from experiments, even when only up to the second order kernel function is considered. The characterization of material parameters becomes even more complicated for the anisotropic and nonlinear time-dependent case, which is the case for piezoelectric ceramics. In case of the third order term is included, the following third order kernel function can be considered.

$$\begin{aligned}\psi_3(t-s_1, t-s_2, t-s_3) &= C_0 + C_1(3 - e^{-(t-s_1)/\eta_1} - e^{-(t-s_2)/\eta_2} - e^{-(t-s_3)/\eta_3}) + \\ &\quad C_2(1 - e^{-(t-s_1)/\eta_1})(1 - e^{-(t-s_2)/\eta_2})(1 - e^{-(t-s_3)/\eta_3})\end{aligned}\quad (3.15)$$

It is also necessary that $\psi_3(t, t, t-s_1) = \psi_3(t-s_1, t, t) = \psi_3(t, t-s_1, t)$. Detailed description of this method and its implementation for numerical method is discussed in Sohrabi and Muliana [69].

3.2 Time Integration Method for Multiple Integral Form

A numerical algorithm for determining time-dependent response from the multiple integral moduli is presented here. Let $R[I(t-s), t]$ be the time-dependent response at current time $t \geq 0$ due to an input history $I^s \equiv I(s)$

A general single integral representation for the response is:

$$R^t \equiv R[I^s, t] = R[I^0, t] + \int_{0^+}^t \frac{\partial R}{\partial I}[I^s, t-s] \frac{dI^s}{ds} ds; (t \geq 0) \quad (3.16)$$

where

$$R[I^0, t] = R_0(I^0) + R_1(I^0) \left(1 - \exp \left[-\frac{t}{\tau_1} \right] \right) \quad (3.17)$$

and

$$\frac{\partial R}{\partial I}[I^s, t-s] = \frac{\partial R_0(I^s)}{\partial I} + \frac{\partial R_1(I^s)}{\partial I} \left(1 - \exp \left[-\frac{t-s}{\tau_1} \right] \right) \quad (3.18)$$

Here a superscript is used to denote the time-dependent variables. A recursive method is used for solving the above integral form. Substituting Eqs. (3.17) and (3.18) into equation (3.16) yields:

$$R^t = R_0(I^t) + R_1(I^t) - R_1(I^0) \exp \left[-\frac{t}{\tau_1} \right] - q^t \quad (3.19)$$

where

$$q^t = \int_{0^+}^t \frac{\partial R_1(I^s)}{\partial I} \exp \left[-\frac{t-s}{\tau_1} \right] \frac{dI^s}{ds} ds \quad (3.20)$$

is the history variable, which can be approximated as:

$$q^t \approx \exp \left[-\frac{-\Delta t}{\tau_1} \right] q^{t-\Delta t} + \left[\frac{\partial R_1(I^t)}{\partial I} \frac{dI}{ds} \Big|_t + \exp \left[\frac{-\Delta t}{\tau_1} \right] \frac{\partial R_1(I^{t-\Delta t})}{\partial I} \frac{dI}{ds} \Big|_{t-\Delta t} \right] \frac{\Delta t}{2} \quad (3.21)$$

The superscript $t-\Delta t$ denotes the previous time history. At initial time, $q^t = q^0 = 0.0$ and $R^0 = R_0(I^0)$. Equations (3.19) and (3.20) give the corresponding output due to an arbitrary input $I(s)$. For the multi-axial constitutive relation, the approximate solution in equation (3.19) can be applied independently to each scalar component of constitutive equation. The numerical algorithm for the multiple integral models

(one-dimensional representation) with the kernels defined in equation (3.14) can be approximated by applying the recursive method as discussed above. The linear kernel is approximated as:

$$\begin{aligned} \int_{s=0^-}^t \psi_1(t-s) \frac{dI(s)}{ds} ds &\approx \\ [A_0 + A_1] I_t - A_1 I(0^+) \exp\left[-\frac{t}{\tau_1}\right] - q_1^t & \\ q_1^t \approx \exp\left[-\frac{\Delta t}{\tau_1}\right] q_1^{t-\Delta t} + A_1 \frac{\Delta t}{2} \left[\frac{dI}{ds} \Big|_t + \exp\left[-\frac{\Delta t}{\tau_1}\right] \frac{dI}{ds} \Big|_{t-\Delta t} \right] & \\ t \geq 0 & \end{aligned} \quad (3.22)$$

The second order kernel in equation (3.13) is rewritten as:

$$\begin{aligned} \int_{s_1=0^-}^t \int_{s_2=0^-}^t \psi_2(t-s_1, t-s_2) \frac{dI(s_1)}{ds_1} \frac{dI(s_2)}{ds_2} ds_1 ds_2 &= \\ [B_0 + B_1(2 - e^{-t/\lambda_1} - e^{-t/\lambda_1}) + B_2(1 - e^{-t/\lambda_2})(1 - e^{-t/\lambda_2})] I(0^+) I(0^+) + & \\ \int_{s_1=0^-}^t \int_{s_2=0^-}^t \left(B_0 + B_1 (2 - e^{-(t-s_1)/\lambda_1} - e^{-(t-s_2)/\lambda_2}) + \right. & \\ \left. B_2 (1 - e^{-(t-s_1)/\lambda_1})(1 - e^{-(t-s_2)/\lambda_2}) \right) \frac{dI(s_1)}{ds_1} \frac{dI(s_2)}{ds_2} ds_1 ds_2 & \end{aligned} \quad (3.23)$$

It can be approximated by:

$$\begin{aligned} \int_{s_1=0^-}^t \int_{s_2=0^-}^t \psi_2(t-s_1, t-s_2) \frac{dI(s_1)}{ds_1} \frac{dI(s_2)}{ds_2} ds_1 ds_2 &= \\ [B_0 + B_1(2 - e^{-t/\lambda_1} - e^{-t/\lambda_1}) + B_2(1 - e^{-t/\lambda_2})(1 - e^{-t/\lambda_2})] I(0^+) I(0^+) + & \\ (B_0 + 2B_1)(I(t) + I(0^+))^2 - B_1(I(t) + I(0^+))(f_1^t + g_1^t) + & \\ b_2((I(t) + I(0^+))^2 - f_2^t(I(t) + I(0^+)) - g_2^t(I(t) + I(0^+)) + f_2^t g_2^t) & \end{aligned} \quad (3.24)$$

where the history variables $f_1^t, f_2^t, g_1^t, g_2^t$ at $t > 0.0$ are given as:

$$\begin{aligned} f_1^t &\approx \exp\left[-\frac{-\Delta t}{\lambda_1}\right] f_1^{t-\Delta t} + \frac{\Delta t}{2} \left[\frac{dI}{s_1} \Big|_t + \exp\left[\frac{-\Delta t}{\lambda_1}\right] \frac{dI}{s_1} \Big|_{t-\Delta t} \right] \\ g_1^t &\approx \exp\left[-\frac{-\Delta t}{\lambda_1}\right] g_1^{t-\Delta t} + \frac{\Delta t}{2} \left[\frac{dI}{s_2} \Big|_t + \exp\left[\frac{-\Delta t}{\lambda_1}\right] \frac{dI}{s_2} \Big|_{t-\Delta t} \right] \\ f_2^t &\approx \exp\left[-\frac{-\Delta t}{\lambda_2}\right] f_2^{t-\Delta t} + \frac{\Delta t}{2} \left[\frac{dI}{s_1} \Big|_t + \exp\left[\frac{-\Delta t}{\lambda_2}\right] \frac{dI}{s_1} \Big|_{t-\Delta t} \right] \\ g_2^t &\approx \exp\left[-\frac{-\Delta t}{\lambda_2}\right] g_2^{t-\Delta t} + \frac{\Delta t}{2} \left[\frac{dI}{s_2} \Big|_t + \exp\left[\frac{-\Delta t}{\lambda_2}\right] \frac{dI}{s_2} \Big|_{t-\Delta t} \right] \end{aligned} \quad (3.25)$$

It is noted that at initial time $f_1^0 = f_2^0 = g_1^0 = g_2^0 = 0.0$ and $R(0) = A_0 I(0^+) + B_0 I(0^+) I(0^+)$. Thus, the corresponding response due to an arbitrary input obtained from the multiple integral model is approximated as:

$$\begin{aligned} R(t) &\approx [A_0 + A_1] I(t) - A_1 \exp\left[-\frac{t}{\tau_1}\right] - q_1^t \\ &\quad [B_0 + B_1(2 - e^{-t/\lambda_1} - e^{-t/\lambda_1}) + B_2(1 - e^{-t/\lambda_2})(1 - e^{-t/\lambda_2})] I(0^+) I(0^+) + \\ &\quad (B_0 + 2B_1)(I(t) - I(0^+))^2 - B_1(I(t) - I(0^+))(f_1^t + g_1^t) + \\ &\quad B_2 [(I(t) - I(0^+))^2 - f_2^t(I(t) - I(0^+)) - g_2^t(I(t) - I(0^+)) + f_2^t g_2^t] \end{aligned} \quad (3.26)$$

For the multi-axial constitutive relation, the approximate solution in equation (3.26) can be applied independently to each scalar component.

3.2.1 Multiple Integral Model

This section presents a multiple integral model to simulate hysteretic response of a piezoelectric ceramics subject to a sinusoidal electric field. We consider up to the third order kernel function and we examine the effect of these kernel functions on the overall nonlinear hysteretic curve. The following material parameters are used

for the simulation:

$$\begin{aligned}
A_0 &= 200 \cdot 10^{-12} m/V; A_2 = 100 \cdot 10^{-12} m/V \\
\tau_1 &= 2 \text{sec} \\
B_0 = B_1 = B_2 &= 20 \cdot 10^{-18} m^2/V^2 \\
C_0 = C_1 = C_2 &= 50 \cdot 10^{-24} m^3/V^3 \\
\eta_1 &= 2 \text{sec}; \eta_2 = 5 \text{sec}
\end{aligned} \tag{3.27}$$

When only the first and third kernel functions are considered, the nonlinear hysteretic response at steady state under positive and negative electric fields is identical as shown by an anti-symmetric hysteretic curve in Figure 3.7a. The hysteretic response under the amplitude of electric field of 0.25 MV/m shows nearly linear response. Including the second order kernel function allows for different response under positive and negative electric fields as seen in Figure 3.7b. At low amplitude of applied electric field, nearly linear response is shown; however this hysteretic response does not show an anti-symmetric shape with respect to the strain and electric field axes. The contribution of each order of the kernel function depends on the material parameters. For example the material parameters in equation (3.27) yield to more pronounced contribution of the first order kernel function; while the contributions of the second and third order kernel functions are comparable. Intuitively, the corresponding strain response of a piezoelectric ceramics when an electric field is applied in the poling direction (positive electric field) need not be the same as when an electric field is applied opposite to the poling direction (negative electric field), especially for nonlinear response due to high electric fields. Depoling could occur in the piezoelectric ceramics when a negative electric field with a magnitude greater than the coercive electric field is considered. Thus, to incorporate the possibility

of the depoling process, the even order kernel functions can be incorporated in the multiple time-integral model. In order to numerically simulate the depolarization in the piezoelectric ceramics we apply a sinusoidal electric field input with amplitude of 1.5 MV/m. We consider the first and second order kernel functions and use the following material parameters so that the contributions of the first and second order kernel functions on the strain response are comparable:

$$\begin{aligned} A_0 &= 200 \cdot 10^{-12} m/V; A_2 = 100 \cdot 10^{-12} m/V \\ \tau_1 &= 2 \text{sec} \\ B_0 &= B_1 = B_2 = 100 \cdot 10^{-18} m^2/V^2 \\ \eta_1 &= 2 \text{sec}; \eta_2 = 5 \text{sec} \end{aligned} \tag{3.28}$$

Figure 3.7 illustrates the corresponding strain response from the multiple integral model having the first and second kernel functions. The response shows an un-symmetric butterfly-like shape. The un-symmetric butterfly-like strain-electric field response is expected for polarized ferroelectric materials undergoing high amplitude of sinusoidal electric field input. The nonlinear response due to the positive electric field is caused by different microstructural changes than the microstructural changes due to polarization switching under a negative electric field.

3.3 Quasi Linear Viscoelastic (QLV) Model

In an analogy to a time-dependent deformation of visco-elastic materials [79], a single integral representation for formulating time dependent electro-mechanical constitutive equations is also considered. The time dependent electromechanical model is:

$$\begin{aligned}\sigma_{ij}(t) &= \int_{0^-}^t \sum_{k,l=1}^3 \frac{\partial \sigma_{ij}}{\partial \varepsilon_{kl}}(t-s, \varepsilon_{kl}(s)) \dot{\varepsilon}_{kl}(s) ds - \int_{0^-}^t \sum_{k=1}^3 \frac{\partial \sigma_{ij}}{\partial E_k}(t-s, E_k(s)) \dot{E}_k(s) ds \\ D_k(t) &= \int_{0^-}^t \sum_{i,j=1}^3 \frac{\partial D_k}{\partial \varepsilon_{ij}}(t-s, \varepsilon_{ij}(s)) \dot{\varepsilon}_{ij}(s) ds + \int_{0^-}^t \sum_{i=1}^3 \frac{\partial D_k}{\partial E_i}(t-s, E_i(s)) \dot{E}_i(s) ds\end{aligned}\quad (3.29)$$

where the overdot indicates the time derivative, t denotes the present time and s is indicates the time history. It is assumed that all field variables at $t < 0$ are zero, and loading starts at initial time 0. It is assumed that the time and field dependent parts can be separated by multiplicative decomposition¹. Following the Quasi Linear Viscoelastic (QLV) model, the constitutive relation in equations (3.29) can be further expressed in terms of the normalized time-dependent function [74, 26], where it is written as:

$$\begin{aligned}\sigma_{ij}(t) &= \int_{0^-}^t \sum_{k,l=1}^3 K_{ijkl}^C(t-s) \frac{\partial \sigma_{ij}}{\partial \varepsilon_{kl}}(\varepsilon_{kl}(s)) \dot{\varepsilon}_{kl}(s) ds + \\ &\quad \int_{0^-}^t \sum_{k=1}^3 K_{kij}^e(t-s) \frac{\partial \sigma_{ij}}{\partial E_k}(E_k(s)) \dot{E}_k(s) ds \\ D_k(t) &= \int_{0^-}^t \sum_{i,j=1}^3 K_{kij}^e(t-s) \frac{\partial D_k}{\partial \varepsilon_{ij}}(\varepsilon_{ij}(s)) \dot{\varepsilon}_{ij}(s) ds + \\ &\quad \int_{0^-}^t \sum_{i=1}^3 K_{ki}^\kappa(t-s) \frac{\partial D_k}{\partial E_i}(E_i(s)) \dot{E}_i(s) ds\end{aligned}\quad (3.30)$$

where K_{ijkl}^C , K_{kij}^e and K_{ki}^κ are the normalized time-dependent tensors corresponding to the elastic, electromechanical coupling, and permittivity tensor, respectively. The stresses σ_{ij} , and electric displacements D_k , are evaluated at time t and the input

¹The separation of variables between the time and field dependent parts was adopted from the quasi linear viscoelastic (QLV) model proposed by Fung [26], which is used in many biological materials.

history is prescribed at $0^- < s < t$. For the time-dependent constitutive relation, the kernel functions can be chosen to be general functions of time that are in accordance with the time-dependent behaviors, e.g., relaxation or creep like behaviors, of the materials. In this study a series of discrete exponential functions, often called Prony series, is used for each time dependent kernel function. The nonlinear time-dependent response discussed in this section can be used to model hysteresis electro-mechanical response of polarized piezoelectric ceramics under a cyclic electric field. The kernel functions are expressed as:

$$\begin{aligned} K_{ijkl}^C(t) &= \sum_{I=0}^{NP} {}^I K_{ijkl}^C \exp(-{}^I \lambda_{ijkl}^C t) \\ K_{ijk}^e(t) &= \sum_{I=0}^{NP} {}^I K_{ijk}^e \exp(-{}^I \lambda_{ijk}^e t) \\ K_{ki}^\kappa(t) &= \sum_{I=0}^{NP} {}^I K_{ki}^\kappa \exp(-{}^I \lambda_{ki}^\kappa t) \end{aligned} \quad (3.31)$$

where ${}^I K_{ijkl}^C$, ${}^I K_{ijk}^e$, ${}^I K_{ki}^\kappa$, ${}^I \lambda_{ijkl}$, ${}^I \lambda_{ijk}^e$, and ${}^I \lambda_{ki}^\kappa$ are the material parameter related to I^{th} component of Prony series of $K_{ijkl}^C(t)$, $K_{ijk}^e(t)$, and $K_{ki}^\kappa(t)$. Equation (3.31) defines the time dependent functions, corresponding to the electro-mechanical properties. The chosen time-dependent functions for material properties, either creep or relaxation function, are determined based on the experimental data. It is also possible that some terms in the properties experience relaxation and other terms experience creep responses. Zhou and Kamlah [83] and Anderson [7] performed experiment on PZT ceramics. They have shown that the electric displacement in the tested piezoelectric ceramics increases with time when a constant electric field is prescribed. In such cases, the time-dependent electric permittivity constants should follow creep functions. It has also been shown that piezoelectric ceramics experience creep deformation due to constant stress, or they undergo stress relaxation when

constant strain is prescribed.

When mathematical models with rather simple forms are considered for the input history and time-dependent material properties, it is possible to obtain exact analytical solutions for the nonlinear time dependent constitutive equation. Laplace transform method [79] is often used to determine the corresponding time-dependent field variables for the linear response of materials. Piezoelectric ceramics exhibit nonlinear electro-mechanical response under a relatively large magnitude of electric field. In dealing with nonlinear responses, numerical methods are considered for obtaining solutions to the governing equations. Recursive integration technique has been shown to be very effective in solving the nonlinear integral problem. In this study, a numerical method based on the recursive approach is adopted for solving the nonlinear time-dependent electro-mechanical coupling response. This numerical technique will be integrated into FE analyses that is explained in following sections.

Using the time dependent constitutive equations that were presented in equation (3.30) and the time kernel function that is expressed as series of exponential functions (equation (3.31)) with ${}^I\lambda_{ijkl} = 0$, ${}^I\lambda_{ijk}^e = 0$, and ${}^I\lambda_{ki}^\kappa = 0$, the expanded constitutive equations are written as:

$$\begin{aligned}
\sigma_{ij}(t) &= \sum_{k,l=1}^3 {}^0K_{ijkl}^C \frac{\partial \sigma_{ij}}{\partial \varepsilon_{kl}}(\varepsilon_{kl}(t)) \varepsilon_{kl}(t) + \sum_{k=1}^3 {}^0K_{ijk}^e \frac{\partial \sigma_{ij}}{\partial E_k}(E_k(t)) E_k(t) + \\
&\quad \int_{0^-}^t \sum_{k,l=1}^3 \sum_{I=1}^{NP} {}^I K_{ijkl}^C \exp(-{}^I \lambda_{ijkl}^C [t-s]) \frac{\partial \sigma_{ij}}{\partial \varepsilon_{kl}}(\varepsilon_{kl}(s)) \dot{\varepsilon}_{kl}(s) ds + \\
&\quad \int_0^t \sum_{k=1}^3 \sum_{I=1}^{NP} {}^I K_{ijk}^e \exp(-{}^I \lambda_{ijk}^e [t-s]) \frac{\partial \sigma_{ij}}{\partial E_k}(E_k(s)) \dot{E}_k(s) ds \\
D_k(t) &= \sum_{i,j=1}^3 {}^0K_{ijk}^e \frac{\partial D_k}{\partial \varepsilon_{ij}}(\varepsilon_{ij}(t)) \varepsilon_{ij}(t) + \sum_{i=1}^3 {}^0K_{ki}^\kappa \frac{\partial D_k}{\partial E_i}(E_i(t)) E_i(t) + \\
&\quad \int_{0^-}^t \sum_{i,j=1}^3 \sum_{I=1}^{NP} {}^I K_{ijk}^e \exp(-{}^I \lambda_{ijk}^e [t-s]) \frac{\partial D_k}{\partial \varepsilon_{ij}}(\varepsilon_{ij}(s)) \dot{\varepsilon}_{ij}(s) ds + \\
&\quad \int_{0^-}^t \sum_{i=1}^3 \sum_{I=0}^{NP} {}^I K_{ki}^\kappa \exp(-{}^I \lambda_{ki}^\kappa [t-s]) \frac{\partial D_k}{\partial E_i}(E_i(s)) \dot{E}_i(s) ds
\end{aligned} \tag{3.32}$$

Equations (3.32) are rewritten with the definition of history variables as follows:

$$\begin{aligned}
\sigma_{ij}(t) &= \sum_{k,l=1}^3 {}^0K_{ijkl}^C \frac{\partial \sigma_{ij}}{\partial \varepsilon_{kl}}(\varepsilon_{kl}(t)) \varepsilon_{kl}(t) + \sum_{k,l=1}^3 \sum_{I=1}^{NP} {}^I q_{ijkl}^{\sigma_C}(t) + \\
&\quad \sum_{k=1}^3 {}^0K_{ijk}^e \frac{\partial \sigma_{ij}}{\partial E_k}(E_k(t)) E_k(t) + \sum_{k=1}^3 \sum_{I=1}^{NP} {}^I q_{ijk}^{\sigma_e}(t) \\
D_k(t) &= \sum_{i,j=1}^3 {}^0K_{ijk}^e \frac{\partial D_k}{\partial \varepsilon_{ij}}(\varepsilon_{ij}(t)) \varepsilon_{ij}(t) + \sum_{i,j=1}^3 \sum_{I=1}^{NP} {}^I q_{kij}^{D_e}(t) + \\
&\quad \sum_{i=1}^3 {}^0K_{ki}^\kappa \frac{\partial D_k}{\partial E_i}(E_i(t)) E_i(t) + \sum_{i=1}^3 \sum_{I=1}^{NP} {}^I q_{ki}^{D_\kappa}(t)
\end{aligned} \tag{3.33}$$

where the variables ${}^I q_{ijkl}^{\sigma_C}(t)$, ${}^I q_{ijk}^{\sigma_e}(t)$, ${}^I q_{kij}^{D_e}(t)$ and ${}^I q_{ki}^{D_\kappa}(t)$ are defined to incorporate the history in the time integral constitutive equations. The time integral functions are split into two parts, the first part carries the integral from the beginning to the time $(t - \Delta t)$ and the second part incorporates the integral within an incremental time

Δt . The recursive method is used for all the integrations. Consider a simple integral with an exponential function such as $q(t) = \int_0^t \exp(-\lambda[t-s])f(s)ds$. This integral can be approximated as $q(t) \approx \exp(-\lambda\Delta t)q(t-\Delta t) + \frac{\Delta t}{2}[f(t) + \exp(-\lambda\Delta t)f(t-\Delta t)]$. This recursive scheme is used for solving the time dependent constitutive equations. Using the recursive integral, the history variables are given as:

$$\begin{aligned}
{}^I q_{ijkl}^{\sigma_C}(t) &= \exp(-{}^I \lambda_{ijkl}^C[\Delta t]) {}^I q_{ijkl}^{\sigma_C}(t-\Delta t) + \\
&\quad \int_{t-\Delta t}^t {}^I K_{ijkl}^C \exp(-{}^I \lambda_{ijkl}^C[t-s]) \frac{\partial \sigma_{ij}}{\partial \varepsilon_{kl}}(\varepsilon_{kl}(s)) \dot{\varepsilon}_{kl}(s) ds \\
{}^I q_{ijk}^{\sigma_e}(t) &= \exp(-{}^I \lambda_{ijk}^e[\Delta t]) {}^I q_{ijk}^{\sigma_e}(t-\Delta t) + \\
&\quad \int_{t-\Delta t}^t {}^I K_{ijk}^e \exp(-{}^I \lambda_{ijk}^e[t-s]) \frac{\partial \sigma_{ij}}{\partial E_k}(E_k(s)) \dot{E}_k(s) ds \\
{}^I q_{ijk}^{D_e}(t) &= \exp(-{}^I \lambda_{ijk}^e[\Delta t]) {}^I q_{ijk}^{D_e}(t-\Delta t) + \\
&\quad \int_{t-\Delta t}^t {}^I K_{ijk}^e \exp(-{}^I \lambda_{ijk}^e[t-s]) \frac{\partial D_k}{\partial \varepsilon_{ij}}(\varepsilon_{ij}(s)) \dot{\varepsilon}_{ij}(s) ds \\
{}^I q_{ki}^{D_\kappa}(t) &= \exp(-{}^I \lambda_{ki}^\kappa[\Delta t]) {}^I q_{ki}^{D_\kappa}(t-\Delta t) + \\
&\quad \int_{t-\Delta t}^t {}^I K_{ki}^\kappa \exp(-{}^I \lambda_{ki}^\kappa[t-s]) \frac{\partial D_k}{\partial E_i}(E_i(s)) \dot{E}_i(s) ds
\end{aligned} \tag{3.34}$$

The above equations only need to be integrated within a time increment Δt . An approximate form of the time derivatives of field variables is taken as: $\dot{\varepsilon}_{kl} \approx \frac{\Delta \varepsilon_{kl}}{\Delta t}$ and $\dot{E}_k \approx \frac{\Delta E_k}{\Delta t}$. Upon solving the integrals in equation (3.34) the history variables are:

$$\begin{aligned}
{}^I q_{ijkl}^{\sigma_C}(t) &= \exp(-{}^I \lambda_{ijkl}^C [\Delta t]) {}^I q_{ijkl}^{\sigma_C}(t - \Delta t) + \\
&\quad \frac{{}^I K_{ijkl}^C}{2} \left(\exp(-{}^I \lambda_{ijkl}^C [\Delta t]) \frac{\partial \sigma_{ij}}{\partial \varepsilon_{kl}} (\varepsilon_{kl}(t - \Delta t)) \Delta \varepsilon_{kl}(t - \Delta t) + \right. \\
&\quad \left. \frac{\partial \sigma_{ij}}{\partial \varepsilon_{kl}} (\varepsilon_{kl}(t)) \Delta \varepsilon_{kl}(t) \right) \\
{}^I q_{ijk}^{\sigma_e}(t) &= \exp(-{}^I \lambda_{ijk}^e [\Delta t]) {}^I q_{ijk}^{\sigma_e}(t - \Delta t) + \\
&\quad \frac{{}^I K_{ijk}^e}{2} \left(\exp(-{}^I \lambda_{ijk}^e [\Delta t]) \frac{\partial \sigma_{ij}}{\partial E_k} (E_k(t - \Delta t)) \Delta E_k(t - \Delta t) + \right. \\
&\quad \left. \frac{\partial \sigma_{ij}}{\partial E_k} (E_k(t)) \Delta E_k(t) \right) \\
{}^I q_{ijk}^{D_e}(t) &= \exp(-{}^I \lambda_{ijk}^e [\Delta t]) {}^I q_k^{D_e}(t - \Delta t) + \\
&\quad \frac{{}^I K_{ijk}^e}{2} \left(\exp(-{}^I \lambda_{ijk}^e [\Delta t]) \frac{\partial D_k}{\partial \varepsilon_{ij}} (\varepsilon_{ij}(t - \Delta t)) \Delta \varepsilon_{ij}(t - \Delta t) + \right. \\
&\quad \left. \frac{\partial D_k}{\partial \varepsilon_{ij}} (\varepsilon_{ij}(t)) \Delta \varepsilon_{ij}(t) \right) \\
{}^I q_{ki}^{D_\kappa}(t) &= \exp(-{}^I \lambda_{ki}^\kappa [\Delta t]) {}^I q_k^{D_\kappa}(t - \Delta t) + \\
&\quad \frac{{}^I K_{ki}^\kappa}{2} \left(\exp(-{}^I \lambda_{ki}^\kappa [\Delta t]) \frac{\partial D_k}{\partial E_i} (E_i(t - \Delta t)) \Delta E_i(t - \Delta t) + \right. \\
&\quad \left. \frac{\partial D_k}{\partial E_i} (E_i(t)) \Delta E_i(t) \right)
\end{aligned} \tag{3.35}$$

Equations (3.33) and (3.35) give an approximate solutions of nonlinear-time-dependent constitutive equations. In the above equations the strain and electric field at each time increment are the independent variables that will be determined from structural analyses.

3.4 Finite Element Implementation of QLV Model

This section briefly presents a FE formulation for analyzing the nonlinear time-dependent electro-mechanical responses of piezoelectric devices. At structural scale, displacement and electric potential are taken as independent field variables, which

are sampled at nodes in finite elements. At the material scale (Gaussian integration points), strains and electric fields are the independent field variables, which are determined from equations (3.5) and (3.6), respectively. At material points the constitutive model discussed in the previous section is used to determine the corresponding stress and electric displacements. General FE formulations for linear and time-independent electro-mechanical response of piezoelectric materials can be found in [14]. This study focuses on nonlinear time dependent electro-mechanical responses of piezoelectric materials and structures.

Consider a 3D continuum element placed in a Cartesian coordinates x_1, x_2, x_3 . Let $[u]^T = [u_1, u_2, u_3, \phi]^T$ be the element field variables (displacements and electric potential). The nodal displacement and electric potential on the element are:

$$[d]^T = [u_1^1, u_2^1, u_3^1, \phi^1 \dots u_1^{nne}, u_2^{nne}, u_3^{nne}, \phi^{nne}] \quad (3.36)$$

where nne is the number of nodes in an element. The field variables in the element u_i are at the nodes d_i are related by the shape function matrix φ_{ip} as follows:

$$u_i = \sum_{p=1}^{ndfe} \varphi_{ip} d_p, (i = 1 \dots nne) \quad (3.37)$$

where $ndfe$ is number of degrees of freedom in each node. The same shape functions are used for the displacement and electric potential field variables. To solve the nonlinear equation, the analyses start with trial linearized relations, followed by an iteration at each time increment in order to minimize error from linearizing the nonlinear equations. At each time increment and at each material point, the constitutive relations in equation (3.30) are implemented. The incremental solution method given in equations (3.33)-(3.35) is used. The finite element analysis based

on variational principle is considered for solving the equilibrium equations and determining the field variables. The virtual work for the electro-mechanically coupled system is [14, 73]:

$$\delta\pi = \int_V \sum_{i,j=1}^3 \sigma_{ij} \delta\varepsilon_{ij} dV - \int_V \sum_{i=1}^3 D_i \delta E_i dV - \int_{\partial V} \sum_{i=1}^3 T_i \delta u_i d\partial V + \int_{\partial V} Q \delta \phi d\partial V \quad (3.38)$$

where T_i and u_i denote the components of the surface traction and mechanical displacement vector, respectively. Moreover, Q and ϕ are the surface charge and scalar potential, respectively. Definition of strain in equation (3.5) and electric field in equation (3.6), are used in the virtual work in equation (3.38). The virtual work is now presented as a function of degrees of freedom and their variation, which are $[u_1, u_2, u_3, \phi]^T$ and $[\delta u_1, \delta u_2, \delta u_3, \delta \phi]^T$. In forming the equilibrium equations, the derivative of the virtual work with respect to the degrees of freedom is taken and set equal to zero:

$$R_k = \frac{\partial \delta\pi}{\partial \delta d_k} = 0, (k = 1 \dots ndf) \quad (3.39)$$

where R_k is residual. Equation (3.39) represents a system of nonlinear equations with respect to degrees of freedom whose solution is obtained at each time increment. By substituting the virtual work in equation (3.38) into the residual in equation (3.39) we have:

$$R_k = \int_V \sum_{i,j=1}^3 \sigma_{ij} \frac{\partial \varepsilon_{ij}}{\partial \delta d_k} dV - \int_V \sum_{i=1}^3 D_i \frac{\partial \delta E_i}{\partial \delta d_k} dV - \int_{\partial V} \sum_{i=1}^3 T_i \frac{\partial \delta u_i}{\partial \delta d_k} d\partial V + \int_{\partial V} Q \frac{\partial \delta \phi}{\partial \delta d_k} d\partial V \quad (3.40)$$

The derivative of strain and electric field that appears in the above equation

contain the derivatives of the shape functions. Using the approximation functions in equation (3.37) for the field variables and definition of strain and electric field in equations (3.5) and (3.6) we have:

$$\begin{aligned}\frac{\partial \delta \varepsilon_{ij}}{\partial \delta d_k} &= \frac{\varphi_{ik,j} + \varphi_{jk,i}}{2} \\ \frac{\partial \delta E_i}{\partial \delta d_k} &= \varphi_{4k,i}\end{aligned}\quad (3.41)$$

This system of equations is solved iteratively. In this study, the Newton-Raphson iterative method is used to determine the field variables by satisfying $\|R_k\| \leq \epsilon_0$ for the entire structure (ϵ_0 is the convergence tolerance). The corrected field variables from the Newton-Raphson iterative methods for solving the nonlinear equation (3.39) are obtained from:

$$R_k^r = -\frac{\partial R_k^{r-1}}{\partial d_k^r} (d_k^r - d_k^{r-1}) \quad (3.42)$$

where r is the iteration counter and d_k^r is degrees of freedom vector for the entire structure. From equation (3.42), the Newton-Raphson method requires finding the tangent matrix $\frac{\partial R_k^r}{\partial d_k^r}$ in each iteration and at each time increment. The consistent tangent matrix is defined as:

$$\begin{aligned}\mathcal{K}_{kl} &= \frac{\partial R_k}{\partial d_l} = \frac{\partial}{\partial d_l} \frac{\partial \delta \pi}{\partial \delta d_k} = \\ &\sum_{i,j=1}^3 \frac{\partial R_k}{\partial \varepsilon_{ij}} \frac{\partial \varepsilon_{ij}}{\partial d_l} + \sum_{i=1}^3 \frac{\partial R_k}{\partial E_i} \frac{\partial E_i}{\partial d_l} \\ &(l, k = 1 \dots ndf)\end{aligned}\quad (3.43)$$

where ndf is the number of degrees of freedom. The derivative terms in the above equation are defined:

$$\begin{aligned}
\frac{\partial R_k}{\partial \varepsilon_{ij}} &= \int_V \sum_{m,n=1}^3 \frac{\partial \sigma_{mn}}{\partial \varepsilon_{ij}} \frac{\partial \delta \varepsilon_{mn}}{\partial \delta d_k} dV - \int_V \sum_{p=1}^3 \frac{\partial D_p}{\partial \varepsilon_{ij}} \frac{\delta E_p}{\partial \delta d_k} dV \\
\frac{\partial R_k}{\partial E_i} &= \int_V \sum_{m,n=1}^3 \frac{\partial \sigma_{mn}}{\partial E_i} \frac{\partial \delta \varepsilon_{mn}}{\partial \delta d_k} dV - \int_V \sum_{p=1}^3 \frac{\partial D_p}{\partial E_i} \frac{\delta E_p}{\partial \delta d_k} dV
\end{aligned} \tag{3.44}$$

(k = 1 ... ndf)

For the nonlinear and time dependent electro-mechanical response, the material derivatives in equations (3.8) and time representation of stress and electric field are used in the above equation.

3.5 Numerical Implementation

3.5.1 Analyses of Nonlinear Electro-Mechanical Response

The experimental data of piezoelectric ceramics reported in [20] are first used to validate the constitutive model. Calibrating the material properties is a rather non trivial task. The first guess starts with the linear and time independent response. In order to calibrate the material parameter in proposed constitutive model, we use the coupling coefficient d_{ijk} in the constitutive equation, $\varepsilon_{11} = -d_{311}E_3$. The coupling coefficients d_{ijk} are related to the stress coupling coefficients e_{ijk} [43]. The experiment was conducted on G-1195 PZT where the sample was excited with electric field at frequency 0.1Hz and three different amplitudes: 250V/mm, 500V/mm and 750V/mm.

In case a linear and time independent model is considered for the piezoelectric response of this material there will not be any hysteresis response, as shown in Figure 3.2. The material constant d_{311} , is taken to be 340pm/V in order to match the strain at 500V/mm. In order to compare the piezoelectric constant d_{311} of G-1195 PZT with other testing data under small electric field (linear range), the d_{311} value of 180pm/V [49] is also plotted in Figure 3.2.

We use the model in equation (3.32) [74] to include the effect of loading history. The time kernel function with $K(t) = 1.0 - 0.6\exp(-t/1.2)$ is considered within the integral representation for the strain $\varepsilon_{11}(t) = \int_0^t K(t-s) \frac{\partial \varepsilon_{11}}{\partial E_3} \frac{\partial E_3(s)}{\partial s} ds$ with $\frac{\partial \varepsilon_{11}}{\partial E_3} = -d_{311}$ taken to be $340\text{pm}/V$ and the model shows a better result compared to the experiment under amplitude of $250V/mm$ as seen in Figure 3.3. It is clear from these results that the response of this material, even for small strain, is nonlinear, therefore taking $\frac{\partial \varepsilon_{11}}{\partial E_3}$ as a constant leads to some error when large electric field is considered. As it is suggested in the literature [7, 20] the piezoelectric coefficient should be defined as a function of applied electric field (they showed that d_{311} changes linearly with strain and also electric field). In this analysis we include the quadratic function of electric field. Following the same procedure as [74] we define a nonlinear response function $\varepsilon_{11}(E_3) = -d_{311}^0 E_3 - d_{311}^1 |E_3| E_3$. Here we take $d_{311}^0 = 340\text{pm}/V$ and² $d_{311}^1 = 0.71\text{fm}^2/V^2$ the result from this calibration is shown in Figure 3.4. It is seen that the hysteresis strain and electric field curves under several amplitude of electric field at frequency 0.1 Hz determined from the model are in good correlation with experimental data. As discussed previously, it is possible to consider only odd terms in the H.O.T. of the nonlinear constitutive relation. Another nonlinear model incorporating first and third order terms is considered, e.g. $\varepsilon_{11}(E_3) = -d_{311}^0 E_3 - d_{311}^2 E_3^3$ with $d_{311}^0 = 340\text{pm}/V$ and $d_{311}^2 = 0.55\text{zm}/V$ ³ using the time dependent parameter discussed above ($K(t) = 1.0 - 0.6\exp(-t/1.2)$), the nonlinear and time dependent model can capture the hysteresis response under different amplitude of electric fields, as shown in Figure 3.5.

In order to examine the rate (frequency) dependent response, parametric studies are presented by applying electric fields at various frequencies. Different frequency

²f here stands for femto i.e. 10^{-15}

³z here stands for Zepto i.e. 10^{-21}

inputs are applied to the same material constitutive model presented in this section. The electric field amplitude input is chosen to be $750V/mm$. The corresponding strains response of the model under three different frequencies are shown in Figure 3.6. It is apparent from the results that higher frequency of loading reduces time-dependent (hysteresis) effect. This is due to the fact that the material does not have enough time to exhibit time-dependent effect. Fast loading reduces the creep-like or relaxation-like behavior and the area inside the hysteresis curve becomes smaller.

3.5.2 Structural Analyses

Piezoelectric telescopic actuators are used to amplify displacements by utilizing the piezoelectric coupling effect. Using the 3D continuum elements discussed in section 3.4, time-dependent nonlinear electro-mechanical coupling response of telescopic actuators is studied. Detailed discussion of manufacturing of the piezoelectric actuators and experimental tests are given by Alexander et. al. [5, 3, 4]. The actuators are poled in the radial direction and an electric field is applied in such a way that it causes elongation or contraction in the axial direction of the telescopic actuators.

The first actuator to be considered for simulation is PZT-568 that is formed by acrylate polymerization method. The geometry of the actuator is shown in Figure 3.9. In order to activate it and obtain the overall axial deflection, each wall was subjected to electric field in the radial direction. The alternating electric potential with amplitude of $300[V]$ and $-300[V]$ with frequency of $0.1Hz$ is applied. The way that the electric potential is distributed in the actuator is illustrated in Figure 3.10. The displacement due to this applied electric field is obtained from the FE simulation. The corresponding displacement contour at applied electric fields are shown in Figure 3.10. The comparison between the time-dependent hysteresis response from current simulation and experiment are shown in Figure 3.11. The nonlinear

hysteresis response is captured effectively by taking the electro-mechanical coupling coefficients to be a nonlinear function of applied electric field. The material data are calibrated to fit the experimental data presented in [5, 3]. The rest of electro-mechanical properties are taken to be same as PZT and presented in Table 3.1. The nonlinear coefficients are defined with respect to the applied electric field in the radial direction.

Another actuator, MSI-53, is considered in order to examine performance of FE model. The geometry of this actuator is shown in Figure 3.12. The distribution of electric potential in the actuator is shown in Figure 3.13. The material properties of MSI-53 that are used for the FE analysis are given in Table 3.2. It is noted that frequency of applied electric field is taken to be 0.1Hz. The nonlinear coefficients are defined with respect to the applied electric field in the radial direction. The distribution of the axial displacement and electric field distribution for this actuator is shown in Figure 3.14. The tip deflection response of this actuator is simulated using the presented electro-mechanical model and it is compared with experimental result shown in Figure 3.14. There is a good agreement between experiment and the model. The nonlinear coefficient have a very small effect on the result, which could be due to a small amplitude of the electric field applied.

Table 3.1: Material Properties of PZT-586 Actuator on its peak[5]

Young's Modulus	62	GPa
Poisson's Ratio	0.3	
e_{212}	-32.51	C/m ²
e_{122}	13.77	C/m ²
e_{111}	-16.92	C/m ²
$\kappa_{11} = \kappa_{22}$	4	pF/m
κ_{33}	2	pF/m
\hat{b}_{1122}	3.35×10^{-5}	N/V ²
\hat{b}_{1111}	-3.35×10^{-5}	N/V ²
$\kappa_{11} = \kappa_{22}$	4	pF/m
κ_{33}	2	pF/m
${}^0K_{ijk}^e$	1.0	
${}^1K_{ijk}^e$	-0.4	
${}^0\lambda_{ijk}^e$	0	
${}^1\lambda_{ijk}^e$	0.5	

Table 3.2: Material Properties of MSI-53 Actuator [5]

Young's Modulus	60.06	GPa
Poisson's Ratio	0.3	
e_{111}	-20.92	C/m ²
e_{122}	17.06	C/m ²
e_{212}	-45.74	C/m ²
$\kappa_{11} = \kappa_{22}$	4	pF/m
κ_{33}	2	pF/m
\hat{b}_{1122}	3.35×10^{-5}	N/V ²
\hat{b}_{1111}	-3.35×10^{-5}	N/V ²
$\kappa_{11} = \kappa_{22}$	4	pF/m
κ_{33}	2	pF/m
${}^0K_{ijk}^e$	1.0	
${}^1K_{ijk}^e$	-0.4	
${}^0\lambda_{ijk}^e$	0	
${}^1\lambda_{ijk}^e$	0.5	

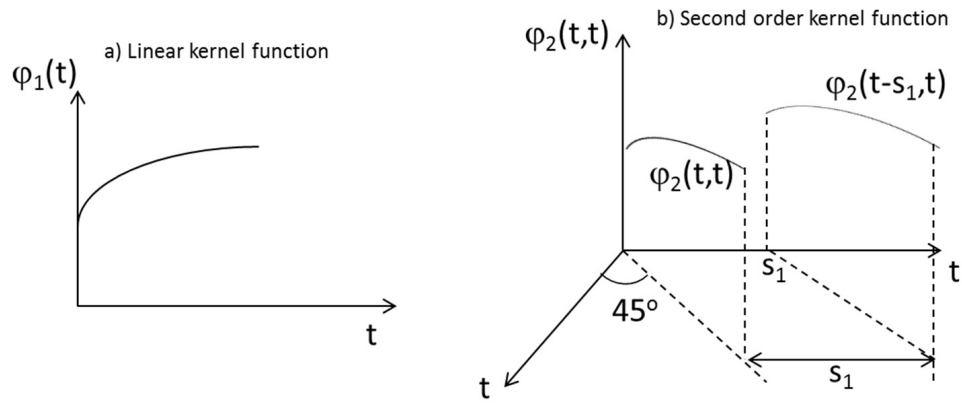


Figure 3.1: The comparison between viscoelastic and elastic materials as host structure.

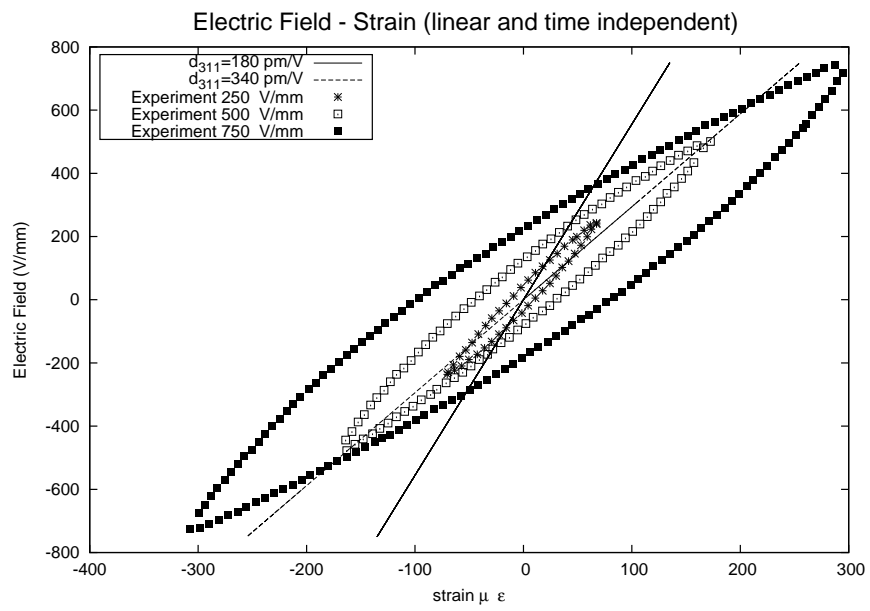


Figure 3.2: Linear time independent model compared with experimental strain (ε_{11}) response under electric field (E_3) with frequency 0.1 Hz in [20].

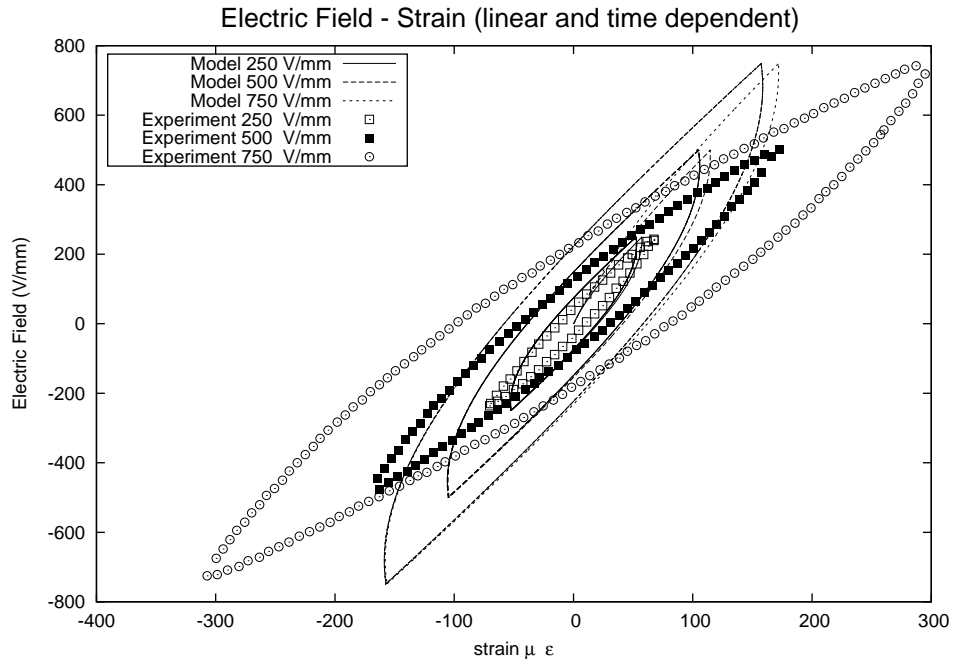


Figure 3.3: Linear and history dependent model compared with experimental strain (ε_{11}) response under electric field (E_3) with frequency 0.1 Hz in [20].

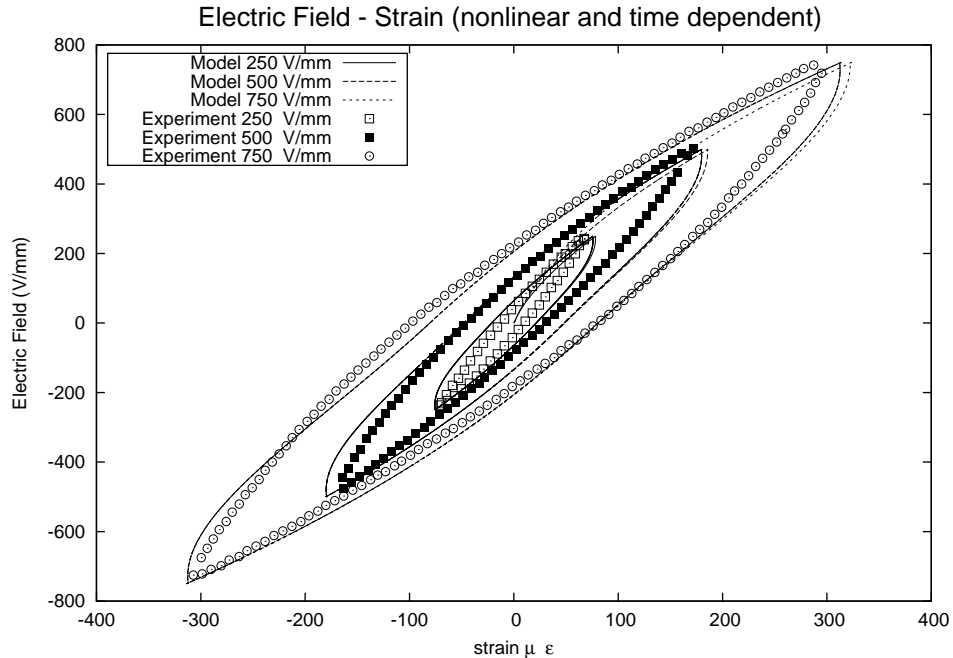


Figure 3.4: Nonlinear time dependent strain (ε_{11}) response under electric field (E_3) with frequency 0.1 Hz compared with experiment[20].

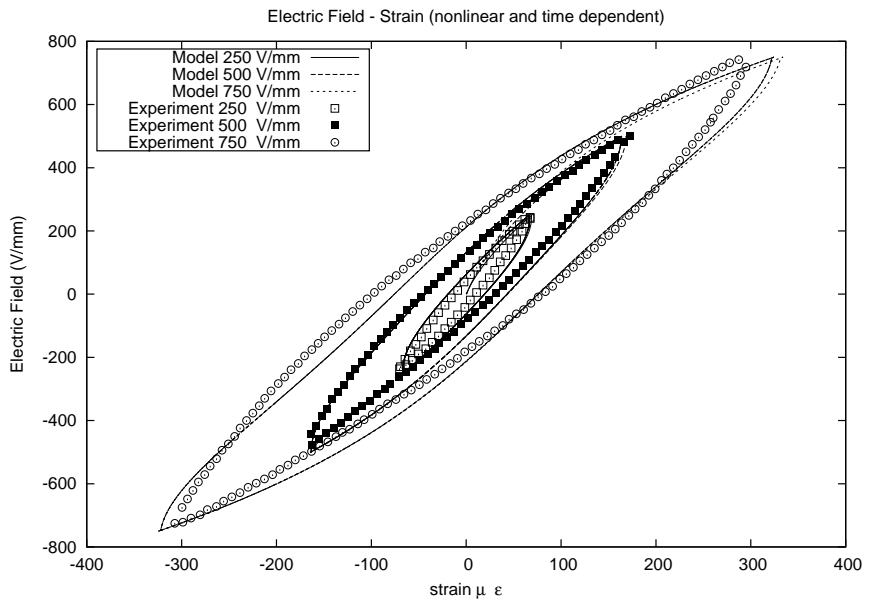


Figure 3.5: Nonlinear time dependent strain (ε_{11}) response under electric field (E_3) with frequency 0.1 Hz for third order model compared with experiment[20].

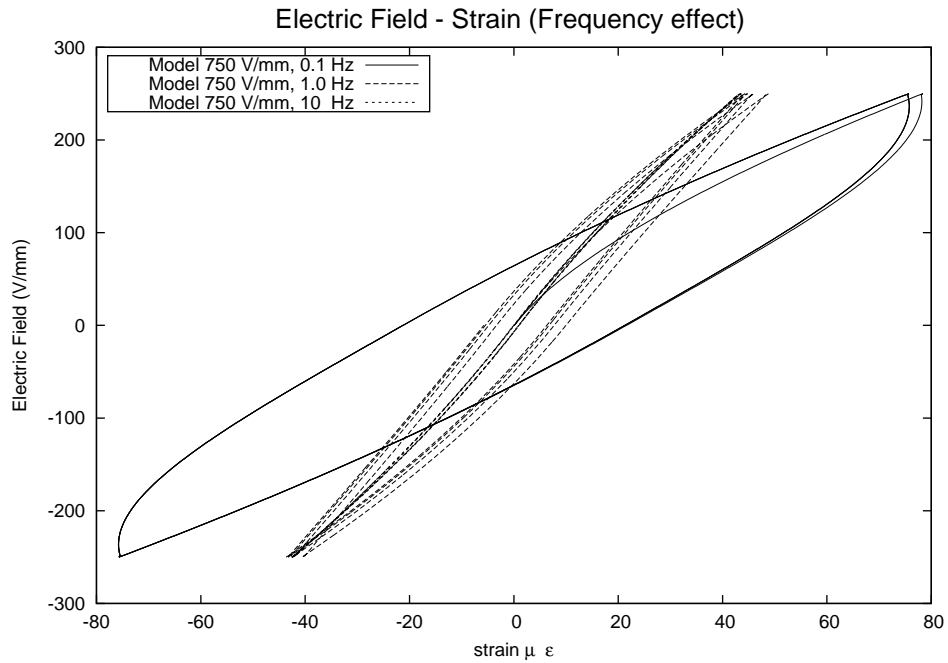


Figure 3.6: Effect of frequency of applied electric field (E_3) on strain (ε_{11}) response.

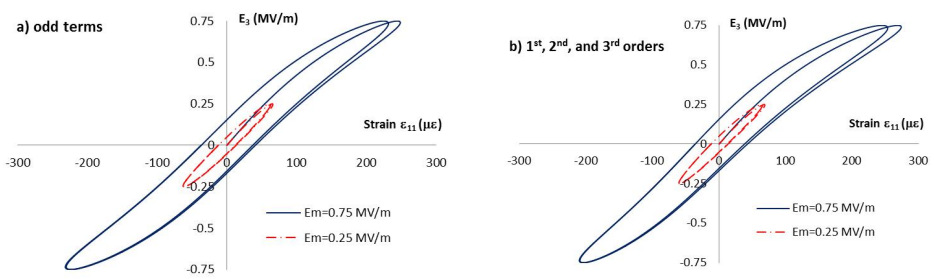


Figure 3.7: The effect of the higher order terms on the hysteretic response ($f=0.1$ Hz)

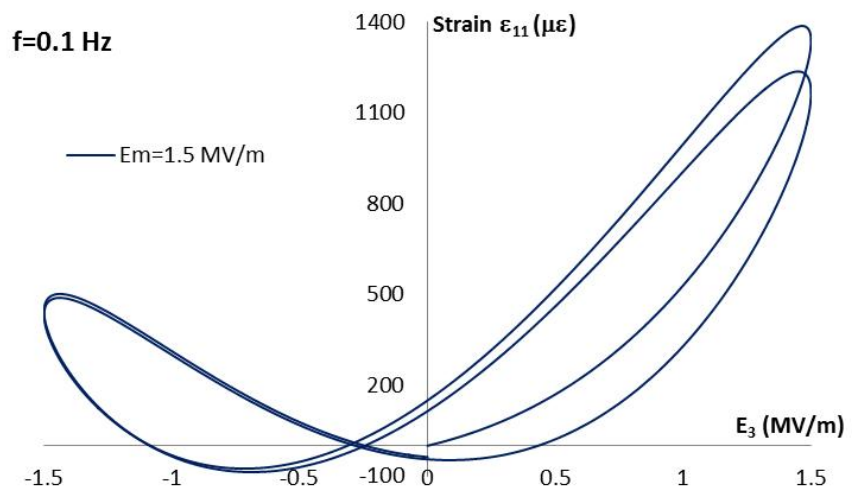


Figure 3.8: The butterfly-like shape of the electro-mechanical coupling response

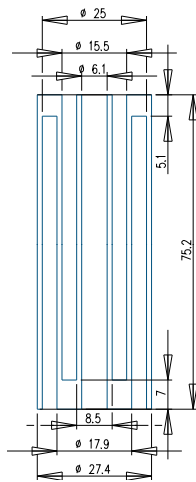


Figure 3.9: Geometry of PZT-586 Telescopic Actuator (dimensions are in mm)

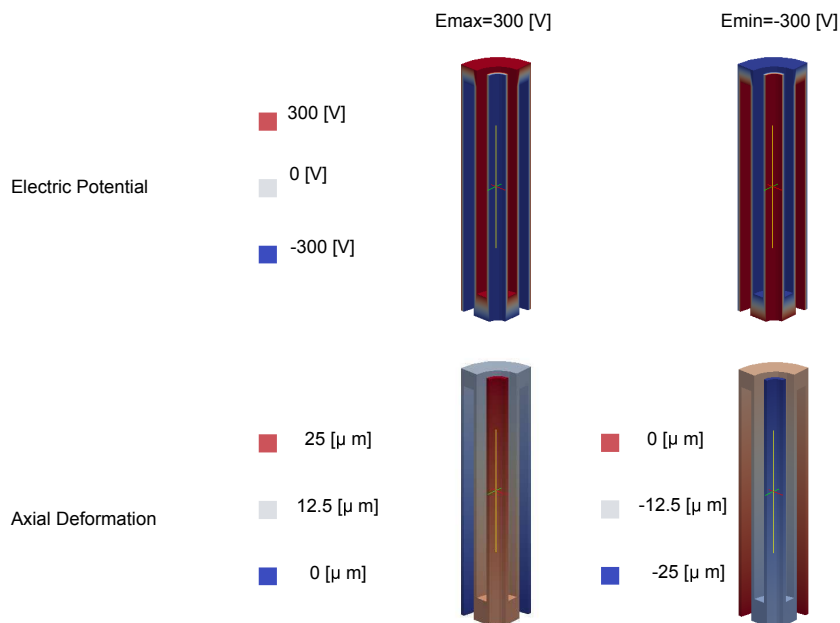


Figure 3.10: Electric potential and deflection contour of PZT-586 Telescopic Actuator

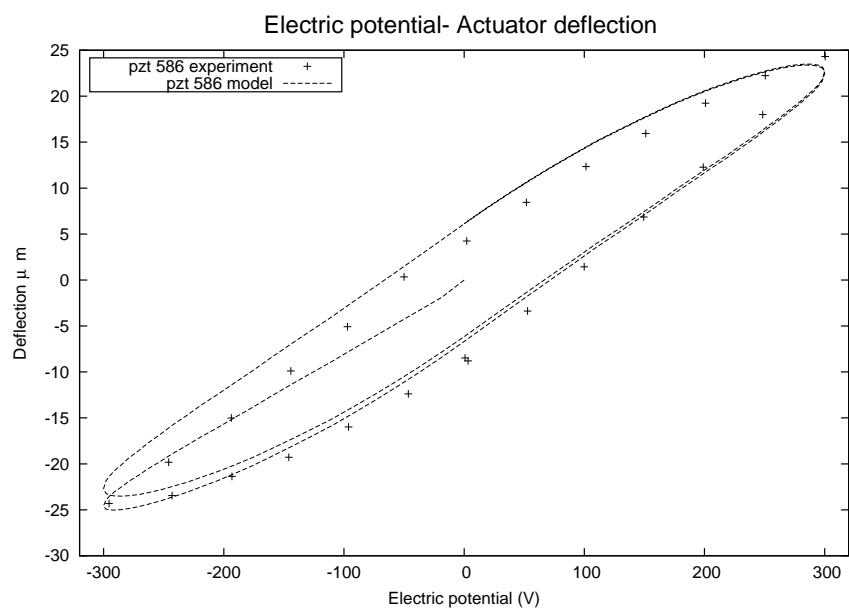


Figure 3.11: Tip deflection of PZT-586 comparing FEM with experiment

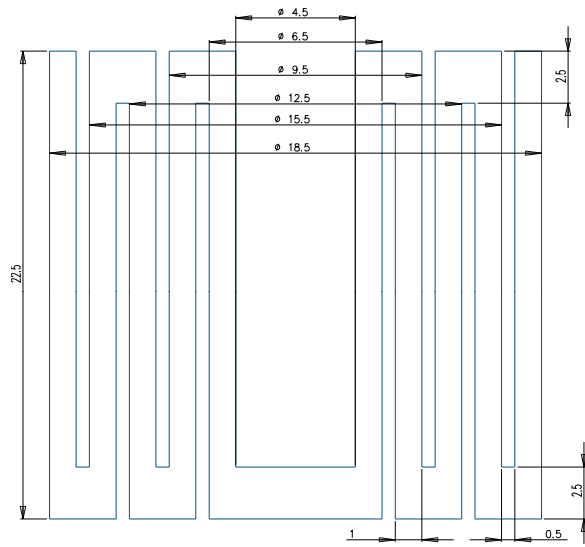


Figure 3.12: Geometry of MSI-53 (dimensions are in mm)

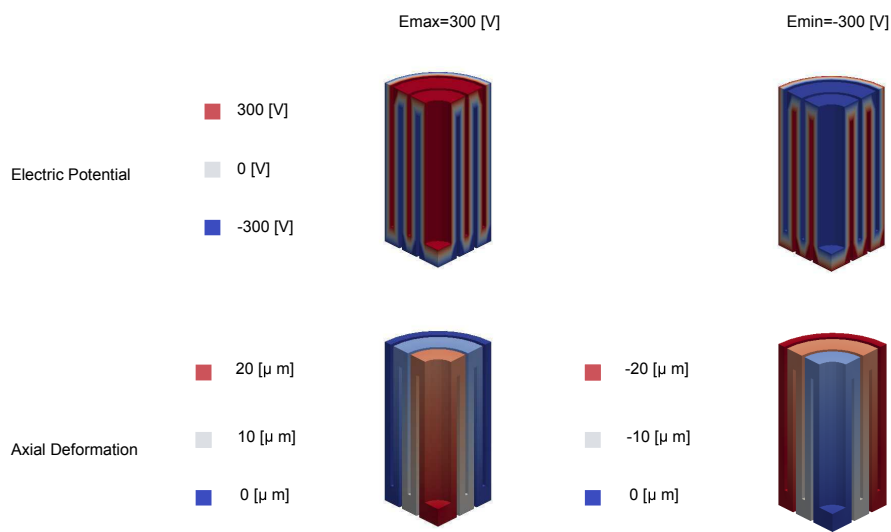


Figure 3.13: Geometry of MSI-53

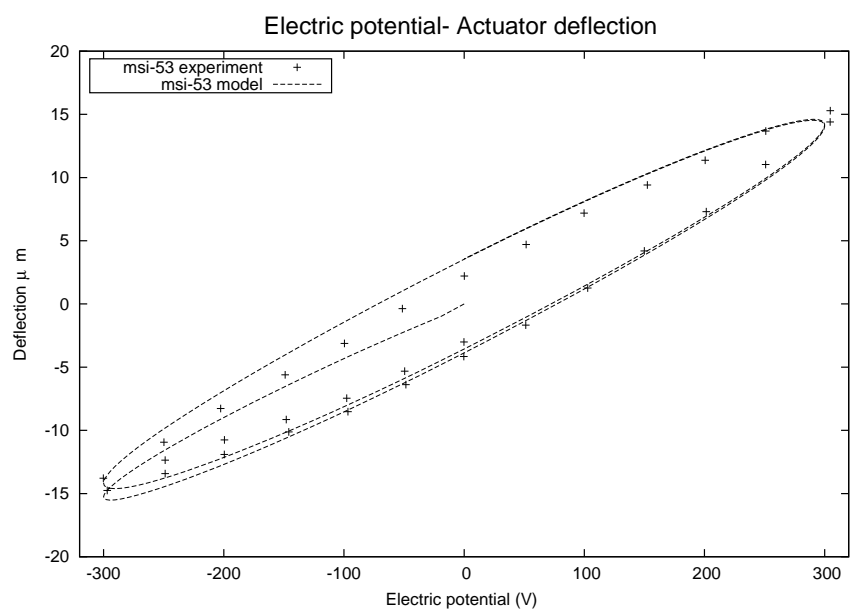


Figure 3.14: Tip deflection of MSI-53 comparing FEM model with experiment

4. STRUCTURAL ANALYSES

This chapter presents analyses of electro-active structures under several loading histories. The constitutive equations that were introduced in the previous chapters are used for the active materials. Two types of smart structures are studied, which are smart multi-layered beams and active fiber composites. The smart beams consist of layers of piezoelectric and inactive materials. Through thickness electric fields are prescribed in order to create bending in the beams. Analytical solutions of the deflections of smart beams with time dependent and electro-mechanical coupling effect are presented. The analytical solutions are also compared to the results obtained from finite element analyses and experiments. The active fiber composite comprises of unidirectional fibers placed in a polymeric matrix. Electrode fingers are attached to the top and bottom surfaces of the composite. In this study, a representative unit cell model is considered for the active fiber composite and the overall electro-mechanical response of the composite is examined.

4.1 Analyses of Smart Beams

Analytical and numerical solutions of the time-dependent electro-mechanical coupled deformations of piezoelectric multi-layered composite beams are presented. The Laplace transform method is used to obtain the analytical solutions while finite element method is considered for the numerical solutions. The results from the analytical solutions are compared with the experimental data and finite element solutions. Several parametric studies are also conducted in order to study the time-dependent electro-mechanical behavior of the composites.

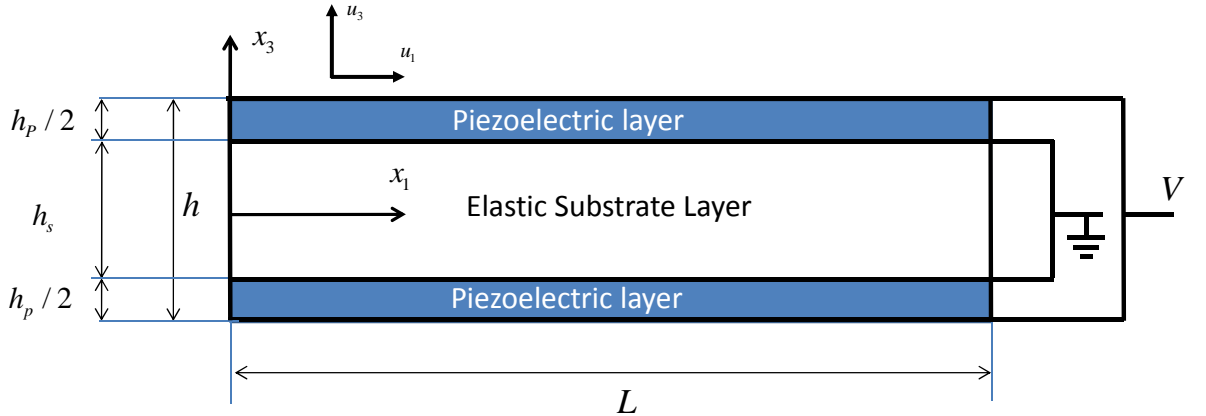


Figure 4.1: Substrated bimorph beam geometry

4.1.1 Governing Equation for Electro-Active Beams

The analyses presented here are suitable for multi-layered slender beams undergoing small deformation gradients. Figure 4.1 illustrates an example of a multi-layered active beam. This beam has three layers, two active layers at the top and bottom and one substrate (inactive) layer in the center. There are electrodes on the surfaces of active layer. An electric field is obtained to these active layers by applying an electric potential difference to the electrodes. In order to describe the various beam theories, the following coordinate system is introduced. The x_1 -coordinate is taken along the length of the beam, x_2 -coordinate is taken along the width of the beam, and the x_3 -coordinate along the thickness (the height) of the beam. According to this coordinate system the loading and geometry are such that the displacements $(\bar{u}_1, \bar{u}_2, \bar{u}_3)$ along the coordinates axis (x_1, x_2, x_3) are independent of x_2 . Moreover, it is assumed that displacements in the width of the beam \bar{u}_2 is zero. For the beam analyses, the field variables are: stress σ_{11} and strain ε_{11} along the longitudinal axis of the beam, electric field E_3 and electric flux (displacement) D_3 through the thickness of the beam. Strain and electric field are taken as the independent variables. The

corresponding stress and electric displacement field for a linear electro-mechanical response is expressed as:

$$\begin{aligned}\sigma_{11} &= C_{1111}\varepsilon_{11} - e_{311}E_3 \\ D_3 &= e_{311}\varepsilon_{11} + \kappa_{33}^{\varepsilon}E_3\end{aligned}\tag{4.1}$$

where C_{1111} is the elastic stiffness measured at constant electric field, e_{311} is the piezoelectric constant, and $\kappa_{33}^{\varepsilon}$ is the dielectric coefficient at constant strain.

The above constitutive model is used for the static response of piezoelectric material. This study deals with time dependent response of active composite beams with nonlinear electro-mechanical behavior. The following constitutive relations for the time-dependent-electro-elastic deformation of solids (see chapter 2) is used for the piezoelectric composite beams shown in figure 4.1 :

$$\begin{aligned}\sigma_{11}(t) &= \int_{0^-}^t K^C(t-s) \frac{\partial \sigma_{11}}{\partial \varepsilon_{11}}(\varepsilon_{11}(s)) \frac{\partial \varepsilon_{11}(s)}{\partial s} ds + \\ &\quad \int_{0^-}^t K^e(t-s) \frac{\partial \sigma_{11}}{\partial E_3}(E_3(s)) \frac{\partial E_3(s)}{\partial s} ds \\ D_3(t) &= \int_{0^-}^t K^e(t-s) \frac{\partial D_3}{\partial \varepsilon_{11}}(\varepsilon_{11}(s)) \frac{\partial \varepsilon_{11}(s)}{\partial s} ds + \\ &\quad \int_{0^-}^t K^{\kappa}(t-s) \frac{\partial D_3}{\partial E_3}(E_3(s)) \frac{\partial E_3(s)}{\partial s} ds\end{aligned}\tag{4.2}$$

This is a one dimensional version of the 3D constitutive equation that is suitable for beam analyses. $K^{\kappa}(t)$, $K^e(t)$, $K^C(t)$ are the normalized time dependent kernels. The time kernels in this constitutive equation can be expressed in terms of Prony series as discussed in chapter 2. A beam is defined as a structural element that is predominantly under bending. Three beam theories are considered which are the classical Euler-Bernoulli beam theory, Timoshenko beam theory, and higher order beam theory. The Euler-Bernoulli beam theory is followed, in which the deformation

due to the transverse shear is ignored. The displacements fields are defined in terms of only two unknown variables, for the transverse displacement and axial displacement:

$$\begin{aligned}\bar{u}_1(x_1, x_2, x_3, t) &= u_1(x_1, t) - x_3 \frac{\partial u_3(x_1, t)}{\partial x_1} \\ \bar{u}_2(x_1, x_2, x_3, t) &= 0 \\ \bar{u}_3(x_1, x_2, x_3, t) &= u_3(x_1, t)\end{aligned}\tag{4.3}$$

where (u_1, u_3) are the displacements along the coordinates axis (x_1, x_3) measured at the neutral axis. The Euler-Bernoulli beam theory is valid when the beams are slender enough. On the other hand if the shear stress in the thickness direction of the beam contributes to the lateral deflection, Timoshenko beam theory is used. The Timoshenko beam theory assumes a constant shear stress in the thickness of beam and the normal axis to the neutral axis of the beam can rotate with respect to the center line. This will introduce a new degree of freedom and a new unknown function due to the additional rotation:

$$\begin{aligned}\bar{u}_1(x_1, x_2, x_3, t) &= u_1(x_1, t) + x_3 \psi_2(x_1, t) \\ \bar{u}_2(x_1, x_2, x_3, t) &= 0 \\ \bar{u}_3(x_1, x_2, x_3, t) &= u_3(x_1, t)\end{aligned}\tag{4.4}$$

In the Timoshenko beam theory, the unknown function $\psi_2(x_1, t)$ is a measure of rotation of the beam. The axial beam displacement u_1 and transverse displacement field of the beam u_3 have the same meaning as equation (4.3). It can be shown by the elasticity solution that the through thickness stress of the beam is quadratic with respect to the transverse coordinate x_3 while the Timoshenko beam theory assumes a constant shear stress through the thickness. In order to correct this inconsistency the shear energy of beam is related to the shear energy of the Timoshenko beam by

a constant called shear correction factor. This constant depends on the geometry of the cross section of the beam and it affects the accuracy of the solutions. The higher order beam theory is introduced to account for the quadratic distribution of the shear through the thickness of the beam and relax the need for the shear correction factor.

The higher order beam theory uses the same number of degrees of freedom as the Timoshenko beam and therefore, the same number of unknowns of the displacement field. Using the fact that, the shear stress is zero in the upper and bottom surface of the beam, the quadratic distribution of the shear stress in the thickness is defined. The displacement field of the theory is defined based on three unknown as in the Timoshenko beam theory:

$$\begin{aligned}\bar{u}_1(x_1, x_2, x_3, t) &= u_1(x_1, t) + x_3\phi_2(x_1, t) + \alpha x_3^3(\phi_2(x_1, t) + \frac{\partial u_3(x_1, t)}{\partial x_1}) \\ \bar{u}_2(x_1, x_2, x_3, t) &= 0 \\ \bar{u}_3(x_1, x_2, x_3, t) &= u_3(x_1, t)\end{aligned}\tag{4.5}$$

By applying stress free conditions on the top and bottom surface of the beam value of α is found to be $-4/3h^2$ [77]. Here $\phi_2(x_1, t)$ is defined as the slope of the normal line measured from the neutral axis. It can be seen that the normal line in the beam is not straight anymore and it is defined as a cubic function. The non zero strain component for the displacement defined in the beam equations (4.3-4.5) are:

$$\begin{aligned}\varepsilon_{11}(x_1, x_3, t) &= \frac{\partial \bar{u}_1(x_1, x_3, t)}{\partial x_1} - x_3 \frac{\partial^2 \bar{u}_3(x_1, x_3, t)}{\partial x_1^2} \\ 2\varepsilon_{13}(x_1, x_3, t) &= \frac{\partial \bar{u}_3(x_1, x_3, t)}{\partial x_1} + \frac{\partial \bar{u}_1(x_1, x_3, t)}{\partial x_3}\end{aligned}\tag{4.6}$$

This strain formulation can be used for each of the above beam theories. It is worth

noting that for the Euler-Bernoulli beams theory ε_{13} is zero. The higher order beam theories can incorporate the effect of shear in the thickness of the beam. In the case of active composite beams are subjected to electric field through thickness with no transverse mechanical loading, the transverse shear deformation is insignificant. As a result, using the Timoshenko or higher order beam theories for predicting the deflection gives the same result as the Euler-Bernoulli beam theory. Therefore, in this study the Euler-Bernoulli beam theory is used for the smart beams.

Using the variational method, the equilibrium equations for the beam model are determined. The external axial force $N_{11}(x_1, t)$ and bending moment $M_{11}(x_1, t)$ are given as:

$$\begin{aligned} N_{11}(x_1, t) &= \int_{x_2, x_3} \sigma_{11}(x_1, x_3, t) dx_2 dx_3 \\ M_{11}(x_1, t) &= \int_{x_2, x_3} x_3 \sigma_{11}(x_1, x_3, t) dx_2 dx_3 \end{aligned} \quad (4.7)$$

The equilibrium equations for the beam bending are:

$$\begin{aligned} \frac{\partial N_{11}(x_1, t)}{\partial x_1} &= f(x_1, t) \\ -\frac{\partial^2 M_{11}(x_1, t)}{\partial x_1^2} &= q(x_1, t) \end{aligned} \quad (4.8)$$

where $f(x_1, t)$ and $q(x_1, t)$ are the distributed axial and transverse loads respectively.

4.1.2 Responses of 3-Layered Active Beam Under Constant Electric Field

This section presents solution for the analyses of 3-layered active beams using the Euler-Bernoulli beam theory. First, the response of the beam neglecting the time dependent effect is obtained. This result is used to verify the finite element formulation and also used to develop the time dependent solution by using the Laplace

transform method. The analytical method that is discussed here is then extended to time dependent and nonlinear electro-mechanical formulation.

Consider a bimorph beam with a thickness h as shown in figure 4.1. The beam consists of two layers of piezoelectric materials with thickness $h_p/2$ each. A substrate layer between these two layers of piezoelectric has a thickness h_s . In practice there are electrodes placed between layers and also on the top and bottom parts of the beam in order to prescribe electric field inputs. If the electric potential V is applied to top and bottom electrodes, the piezoelectric layers will be subjected to electric field $E_3 = 2V/h_p$. The applied electric field in each layer can be either positive or negative depending on the direction of electric potential applied. Regardless of the sign of the applied potential the direction of the formed electric fields on the top and bottom layers are opposite to each other in order to create bending. Since the electrode layer is very thin, its effect on the overall response of the beam is disregarded. The total thickness of the beam is $h = h_p + h_s$ as shown in figure 4.1. Using the equilibrium equation in (4.8), and the linear electro-mechanical constitutive model presented in equation (4.1) the axial force and bending moments are:

$$\begin{aligned} N_{11}(x_1) &= (w C_p h_p + w C_s h_s) u_1 \\ M_{11}(x_1) &= \left(-C_p h_p^2 h_s / 4 - C_p h_p h_s^2 / 4 - C_p h_p^3 / 12 - C_s h_s^3 / 12 \right) w \frac{\partial^2 u_3(x_1, t)}{\partial x_1^2} - \\ &\quad w e E_3 (h_p h_s / 2 - h_p^2 / 4) \end{aligned} \quad (4.9)$$

where w is the width of the beam. A simplified notation for the material parameters is considered here. For the piezoelectric layer the stiffness and piezoelectric constants are $C_{1111} = C_p$, $e_{311} = e$ respectively. For the elastic substrate the properties are $C_{1111} = C_s$ and $e_{311} = 0$. The effect of the electric displacement on the strain is

ignored. If the beam shown in figure 4.1 is clamped at the left end, the boundary conditions are as follows:

$$u_1(0) = u_3(0) = \frac{\partial u_3(0)}{\partial x_1} = 0 \quad (4.10)$$

Then, for a beam with no transverse loading the deflection of the beam is:

$$u_3(x_1) = \frac{1}{2} \frac{3eEh_p(h_p + 2h_s)}{C_p h_p^3 + 3C_p h_p^2 h_s + 3C_p h_p h_s^2 + C_s h_s^3} x_1^2 \quad (4.11)$$

The above analyses is extended for the time dependent constitutive equation of active composite beams. The time dependent electro-mechanical constitutive piezoelectric layers and linear visco-elasticity is considered for the substrate. A closed-form solution for the deformations of the active beam is presented. The time dependent response of the beam is obtained by using the Laplace transform method. Consider the beam geometry as shown in figure 4.1, with the constitutive equation (4.2) for the piezoelectric layers of the beam. The stress in the piezoelectric layers is additively decomposed into the mechanical and electro-mechanical stresses:

$$\sigma_{11} = \sigma_{11}^m + \sigma_{11}^e \quad (4.12)$$

where

$$\begin{aligned} \sigma_{11}^m &= \int_{0^-}^t K^C(t-s) \frac{\partial \sigma_{11}}{\partial \varepsilon_{11}}(\varepsilon_{11}(s)) \frac{\partial \varepsilon_{11}(s)}{\partial s} ds \\ \sigma_{11}^e &= \int_{0^-}^t K^e(t-s) \frac{\partial \sigma_{11}}{\partial E_3}(E_3(s)) \frac{\partial E_3(s)}{\partial s} ds \end{aligned} \quad (4.13)$$

The mechanical stress is considered to be linear and elastic, which for the host structure and active layer are $\sigma_{11}^m = C_s \varepsilon_{11}$ and $\sigma_{11}^m = C_p \varepsilon_{11}$. The stress due to the electro-mechanical coupling is defined as a polynomial function of the electric field

in order to include the effect of high electric fields.

The Laplace transform is used to transform the equations from time domain to the Laplace variable domain. The derivatives with respect to time will be expressed as polynomials with respect to the Laplace variable. The constitutive equation (4.13) for beam is presented in the Laplace form as:

$$\mathcal{L}[\sigma_{11}(t)] = aC_p \mathcal{L}[K^C(t)] \mathcal{L}[\varepsilon_{11}(t)] \quad (4.14)$$

where \mathcal{L} is the Laplace transform and a is the transform variable. In the same manner the Laplace transform for the electro-mechanical stress σ_{11}^e is defined.

$$\mathcal{L}[\sigma_{11}^e(t)] = \mathcal{L}\left[\int_{0^-}^t K^e(t-s) \frac{\partial \sigma_{11}}{\partial E_3}(E_3(s)) \dot{E}_3(s) ds\right] \quad (4.15)$$

Since the electric field is known, the explicit definition of the electro-mechanical coupling stress in the Laplace domain is obtained using equation (4.15). The Laplace transform turns the time dependent integral equation into an algebraic equation.

The differential equation for the displacement with respect to spatial variables are given in Equations (4.8) and (4.7). The axial force and bending moment in the Laplace domain are:

$$\begin{aligned} \bar{N}_{11}(x_1, a) &= \int_{x_2, x_3} \bar{\sigma}_{11}(x_1, x_3, a) dx_2 dx_3 \\ \bar{M}_{11}(x_1, a) &= \int_{x_2, x_3} x_3 \bar{\sigma}_{11}(x_1, x_3, a) dx_2 dx_3 \end{aligned} \quad (4.16)$$

where the upper bar means the function in Laplace domain. The equilibrium equations are:

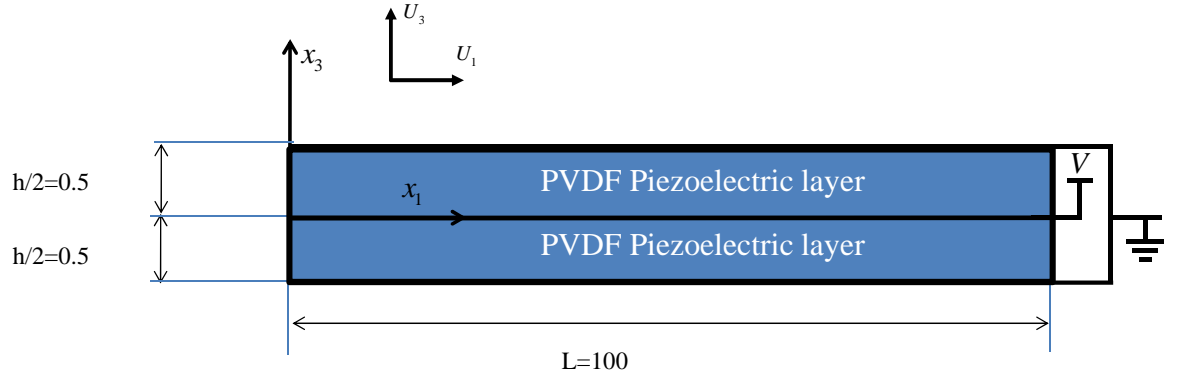


Figure 4.2: Bimorph PVDF beam geometry and placement of electrodes

$$\begin{aligned} \frac{\partial \bar{N}_{11}(x_1, a)}{\partial x_1} &= \bar{f}(x_1, a) \\ - \frac{\partial^2 \bar{M}_{11}(x_1, a)}{\partial x_1^2} &= \bar{q}(x_1, a) \end{aligned} \quad (4.17)$$

It is noted that the applied transverse and axial boundary conditions should be defined in the Laplace domain. The Laplace transform should also be performed for the time dependent boundary conditions. Solving the differential equations presented in equation (4.17) will result in transverse deflection in Laplace space $\bar{u}_3(x_3, a)$. The inverse of the Laplace transform gives the function in time domain:

$$u_3(x_3, t) = \mathcal{L}^{-1} [\bar{u}_3(x_3, a)] \quad (4.18)$$

4.1.3 Numerical Validation

This section compares the result from the analytical solutions to the finite element analyses. The objective of this study is to validate the results from finite element analyses. The experimental data published in literature are also used to validate the analytical and finite element solutions.

An experiment that has been done on a PVDF bimorph is first simulated. The bimorph beam is subjected to a constant electric field input. The PVDF layer is polarized through its thickness direction. The configuration of the beam is illustrated in figure 4.2. This beam is modeled with the results from equation (4.11) with $h_s = 0$ and $h_p = h/2$. Figure 4.2 also illustrates the electrodes that are placed on the top, bottom and middle layers of the beam. The electric potential is applied to the central electrode, and the top and bottom electrodes are grounded. This actuation architecture guarantees that the two PVDF layers will be under electric field in the opposite direction, inducing opposite axial stresses to the top and bottom layers and, allowing for the beam to bend. The distribution of the electric potential through the thickness of the beam from the finite element analyses is shown in figure 4.3. The bending deformation of the bimorph beam is predicted using a linear piezoelectric constitutive equation. Experimental data reported by [75] and analytical solutions [17, 25, 72] of the tip deflection of the bimorph beam are used for comparisons. The material properties used for the PVDF are taken from [72] and also [25]. The Young's modulus C_p or E_y is considered to be $2GPa$ and the shear modulus is taken $1GPa$. The electro-mechanical constant for PVDF, in this case, is taken as $e_{311} = e = 0.046C/m^2$. The dielectric constant or electric dielectric coefficient is taken to be $k^\varepsilon = 0.1062 \times 10^{-8}F/m$. The bonding between the different layers in the bimorph beam is assumed perfect; thus the traction and displacement continuity

Table 4.1: Numerical Result from Present Model for Deflection of PVDF Bimorph

Method		Tip deflection $\times 10^{-7}m$
Experiment [75]		3.15
Analytical solution	$w(x) = 345x^2$	3.45
Plate FEM [25]		3.45
Beam Finite Difference	41 nodes	3.4
2D FEM present model	C2D9 elements in 10x4y mesh	3.15
3D FEM ABAQUS model	C3D8E elements in 162x10y4z mesh	2.99
3D FEM ABAQUS model	C3D20QE elements in 10x1y4z mesh	3.4414
3D FEM present model	C3D20 elements in 5x2y2z mesh	3.455

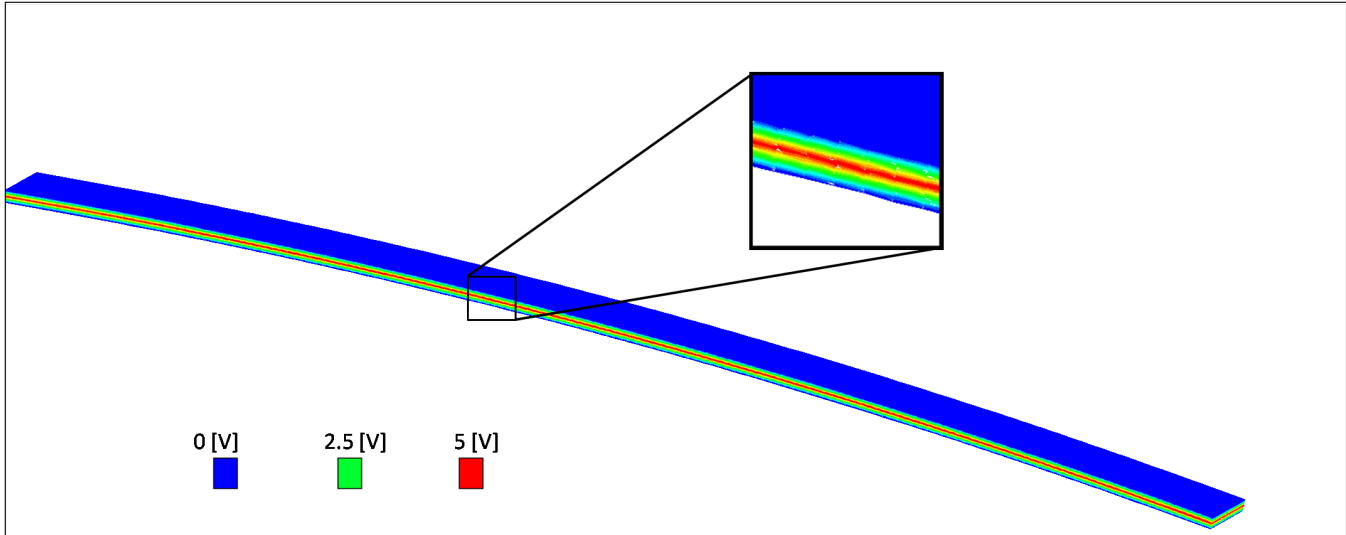


Figure 4.3: Bimorph PVDF beam electric potential distribution

conditions are imposed at the interface layers. The beam has a length L of 100mm, width of 5mm and the thickness of the beam is 1mm. The middle layer is under 0.5 V. This results in 1000V/m electric field to each PVDF layer. The result from the current model is compared with the experiment and also other computational methods, which are presented in Table 4.1. Good comparisons are observed among the results.

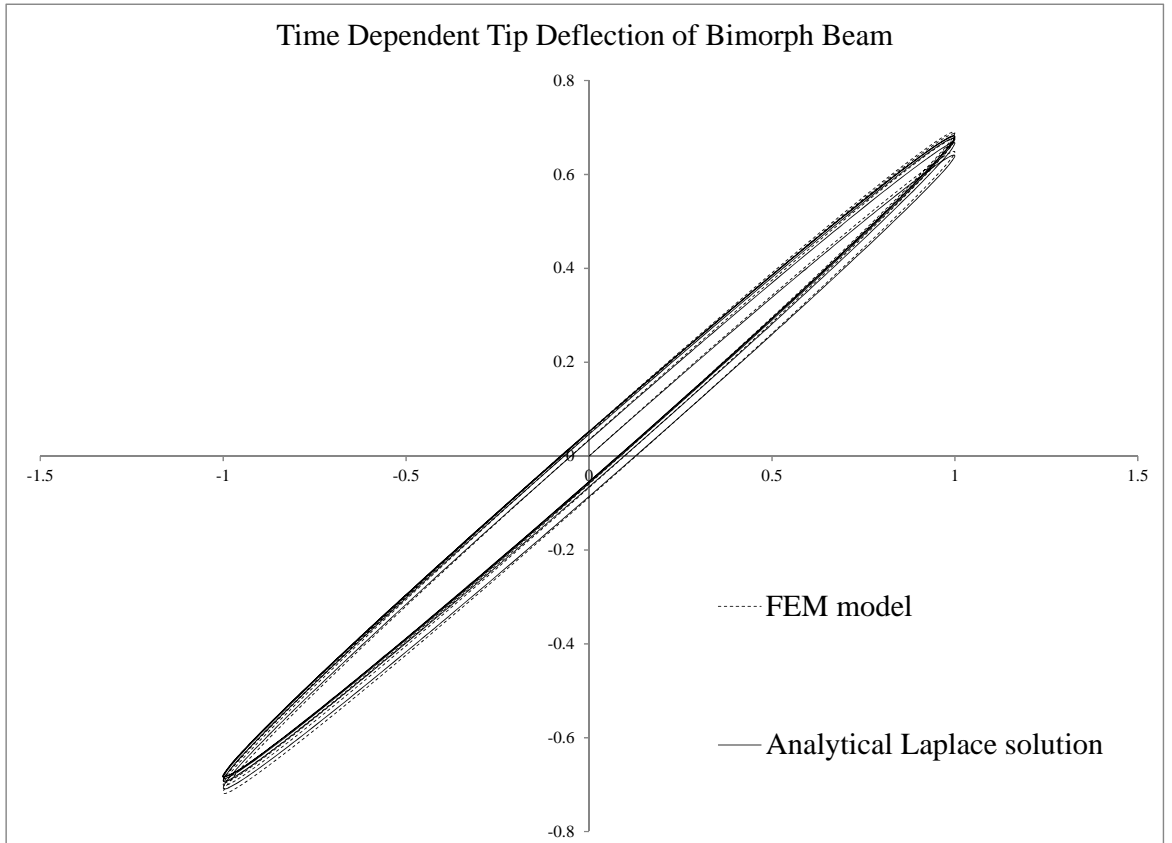


Figure 4.4: Tip deflection of bimorph beam, comparing Laplace solution with numerical recursive method

The time-dependent behavior of active beams are presented here. The Laplace transform method is used for obtaining analytical solutions of the time-dependent electro-elastic beams. A bimorph beam shown in figure 4.1 is subjected to a sinusoidal voltage. The time dependent kernel function for the electro-mechanical properties in equation (4.2) is chosen as $K^e(t) = 1 + \exp(-t)$. A sinusoidal electric field is applied with frequency of 1 Hz and the amplitude 1 V/mm. The electro-mechanical coupling effect is considered to be linear, $\frac{\partial \sigma_{11}}{\partial E_3} = e_{311} = .046$.

Using these values in equations (4.13)-(4.18) and taking inverse of the Laplace transform, the analytical solution for the time dependent deflection of the beam is:

Table 4.2: Coefficients for close form time dependent solution of PVDF beam

n	A_n	B_n	λ_{A_n}	λ_{B_n}
0	$-4.462664015 \times 10^{19}$	$8.333333335 \times 10^{17}$	-1.0	0.0
1	$5.678974503 \times 10^{20}$	1.326291193×10^9	1.0	1.0
2	$4.462664015 \times 10^{19}$	0	1.0	0.0

$$u_3(x_1, t) = \frac{A(t)}{B(t)} \quad (4.19)$$

where $A(t)$ and $B(t)$ are the solutions of time dependent deformation that is obtained by a commercial computer algebra system, Maple. For the present case study with the material properties for PVDF and the kernel function that is defined above, are forms for $A(t)$ and $B(t)$ are:

$$\begin{aligned} A(t) &= A_0 e^{-\lambda_{A_0} t} + A_1 \sin(2\pi\lambda_{A_1} t) + A_2 \cos(2\pi\lambda_{A_2} t) \\ B(t) &= B_0 e^{-\lambda_{B_0} t} + B_1 \sin(2\pi\lambda_{B_1} t) + B_2 \cos(2\pi\lambda_{B_2} t) \end{aligned} \quad (4.20)$$

where the constants for this equation are presented in Table 4.2. The analytical solution is compared with the numerical solution from the recursive finite element analyses. A 3D quadratic element with 20 nodes is used for finite element. It is noted that quadratic elements shown to be more accurate in dealing with bending. The result from analytical solution and finite element analyses are compared in figure 4.4. A good match between the Laplace transform method and numerical solution is observed. This validates the recursive integration algorithm for the linear time-dependent electro-mechanical responses, which are implemented in finite elements.

The nonlinear electro-mechanical deflection of an active beam has been experimentally observed by Lin et al. [44]. This experiment is used to validate the nonlinear and time dependent closed form solution. The beam has three layers, two piezoelec-

tric and one metal substrate. A metallic layer is placed in the middle of the beam with thickness of $h_s = 0.0075in$. The substrate is made of stainless steel and its elastic modulus is taken to be $E_s = C_s = 180GPa$. Two piezoelectric active layer are placed on the top and bottom of the substrate with thickness of $h_p = 0.005in$. These layers are activated by electric potential. The frequency of the excitation is 1Hz and the electric potential is applied with amplitude of 100 V. The beam's length is $L = 1.5in$. The beam's width is $b = 0.375in$. The stiffness of piezoelectric layers in the longitudinal and transverse direction are reported as $E_p^L = C_p = 63GPa$ and $E_p^T = 49GPa$, respectively. The electro-mechanical coupling stress is considered to be a nonlinear cubic function of electric field.

$$\sigma_{11}^e(E_3) = e_{311}^0 E_3 + e_{311}^2 E_3^3 \quad (4.21)$$

where the constants are taken to $e_{311}^0 = 14.5C/m^2$ and $e_{311}^2 = -6pC/m^2$. Moreover, the time dependent kernel function is taken as

$$K_e(t) = K_0^e + K_1^e \exp(-\lambda_1 t) \quad (4.22)$$

where the Prony constants are taken as: $K_0^e = 1.7$, $K_1^e = -0.7$ and $\lambda_1 = -0.7$. The beam is constrained to be simply supported. The result from the deflection produced by the actuator along with the applied voltage is reported in [44]. This comparison is shown in figure 4.5. The cubic approximation of the electro-mechanical coupling is close enough to the experimental data.

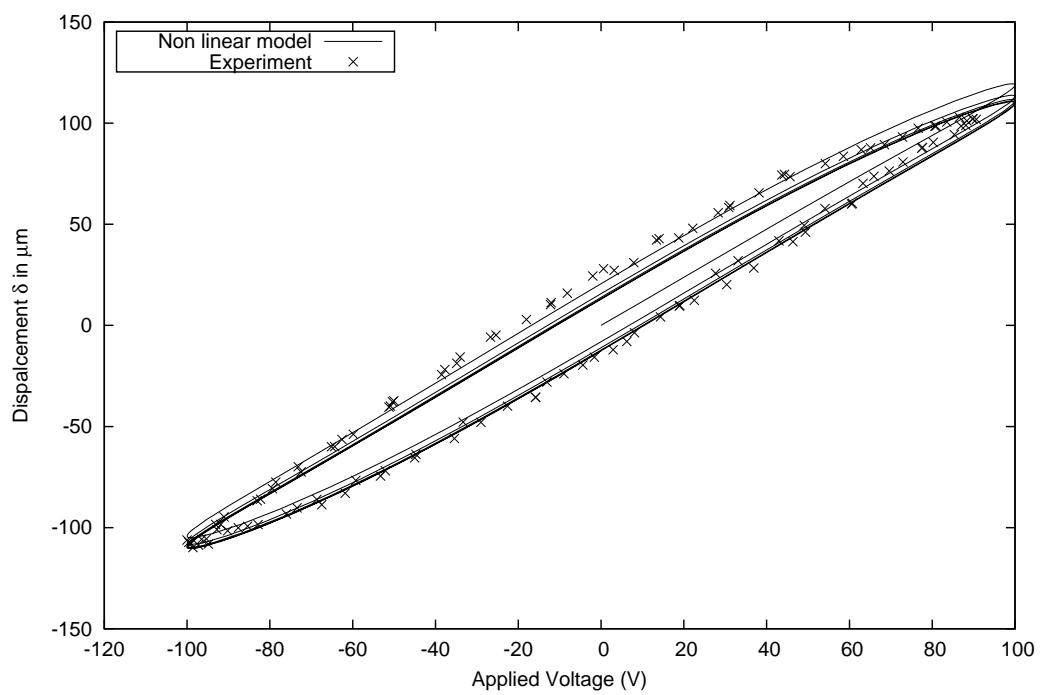


Figure 4.5: Experimental result [44] compared with Laplace solution of an actuator made of three layer active beam

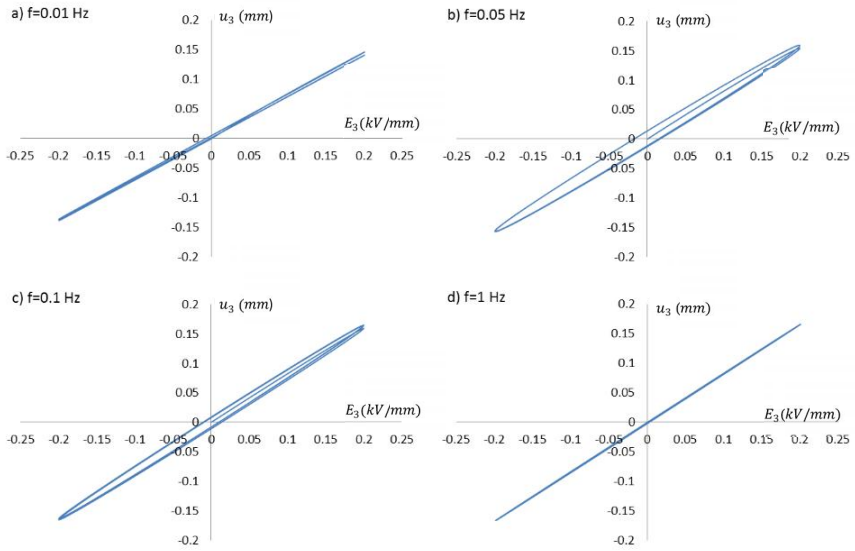


Figure 4.6: Tip deflection of bimorph beam, comparing observing effect of frequency of applied electric field

4.1.4 Effect of Frequency on the Hysteresis Responses of Active Beams

The effect of different histories of electric potential inputs is also analyzed. Consider a bimorph beam consisting of two layers of polarized piezoelectric ceramics and an elastic layer, as shown in figure (4.1). In order to produce a bending deflection in the beam, the two piezoelectric layers should undergo opposite tensile and compressive strains. The beam is fixed at one end and the other end is left free; the top and bottom surfaces are under a traction free condition. A potential is applied at the top and bottom surfaces of the beam and the corresponding displacement is monitored.

A bimorph beam without an elastic layer placed in between the piezoelectric layers is studied as it is shown in (4.2). It is assumed that the beam is relatively slender so that it is sensible to adopt Euler-Bernoulli beam theory in finding the corresponding displacement of the bimorph beam. Since a uniform voltage is prescribed on

the top and bottom surfaces of the beam, the problem reduces to a pure bending problem. The beam has a length of 100mm, width of 1mm and the thickness of each piezoelectric layer is 1mm. The following time-dependent properties of PZT5A are used for the bending analyses.

$$\begin{aligned} C_p(t) &= 90K^C(t) \text{ GPa} & K^C(t) &= 1 + \exp(-0.02t)/3 \\ e(t) &= -5.35K^e(t) \text{ C/m}^2 & K^e(t) &= 1 + \exp(-0.2t)/4 \end{aligned} \quad (4.23)$$

A sinusoidal input of an electric potential with various frequencies are applied. figure 4.6 illustrates hysteresis response of the bending of the bimorph beam. The displacements are measured at the free end ($x_1 = 100\text{mm}$). When the rate of loading is comparable to the characteristics time, the effect of time-dependent material properties on the hysteretic response becomes significant, as shown by the response with frequencies of 0.05Hz and 0.1Hz. When the rate of loading is relatively fast (or slow) with regards to the characteristics time, i.e. $f=0.01\text{Hz}$ and 1Hz , insignificant (less pronounced) time-dependent effect is shown, indicated by narrow ellipsoidal shapes.

4.2 Large Deformation Analyses

In this section, large deformation analyses of slender beams is discussed. We use the bimorph beam geometry that was discussed in the previous example for large deformation analyses. The geometry of this beam is introduced in figure 4.2. In order to validate the result from finite element model, the closed form formulation for simple case of folding of a biomorph beam is considered.

The Green St. Venant strain induced in the material due to deformations is a quadratic function of the displacement gradient [41]. If the deformation is large then the nonlinear term of the strain cannot be disregarded. The quadratic function for

the strain displacement relationship is defined as:

$$\varepsilon_{ij} = \frac{u_{i,j} + u_{j,i}}{2} + \sum_{m=1}^3 \frac{u_{m,i}u_{m,j}}{2} \quad (4.24)$$

Equation (4.24) is the more general form of infinitesimal strain theory that is represented in equation (3.6). The model is already developed based on nonlinear formulation for multi-functional material. Therefore, only the terms for strain should be modified in order to capture large deformation.

It is possible to present analytical solutions for folding of beams [57]. The bimorph beam that is considered for large deformation is only under bending due to electric field. Therefore, the stretch in the beam is neglected. The strain is assumed linear in stress and the linear constitutive equations presented in equations (4.1) and (4.7) are considered for the analyses. The internal bending moment of the beam due to the mechanical strain can be presented as [57]:

$$M_{11}^m = E_1 I_{11} \dot{\phi} \quad (4.25)$$

where E_1 is the Young modulus and it is same as C_p , I_{11} is the second moment of area that is $h_p^3/12$ in the case of bimorph geometry shown in figure 4.2, $\dot{\phi}$ is the curvature of the beam can be presented as $\dot{\phi} = 1/r$ where r is the radius of folded shape of beam. In case of a complete folding of the beam, the radius of curvature for beam will be $r = \frac{L}{2\pi}$, where L is the length of beam.

The electrical bending moment of beam due to electric field using equations 4.1 and 4.7 can be presented as:

$$M_{11}^e = \frac{e_p h_p V}{2} \quad (4.26)$$

There is no other external force or moment is acting on the beam. Then, the equi-

librium equation in the beam can be satisfied at each point on the neutral axis, thus $M_{11}^m = M_{11}^e$.

Considering the mechanical and electrical properties for the PVDF beam the electric potential needed to completely fold the PVDF bimorph beam will be

$$V_{fold} = \frac{h_p^2 \pi C_p}{3e_p L} \quad (4.27)$$

Using the electro-mechanical material properties and geometries of bimorph beam that were discussed before the electric potential for folding the beam is $V_{fold} = 455kV$. This electric potential is applied to the central electrode of the biomorph beam in the finite element analyses. The result from this analyses is shown in figure 4.7. It can be seen that a complete folding is captured by taking the nonlinear kinematics into account as it is expected from the analytical solution presented.

4.3 Active Fiber Composites

Active Fiber Composite (AFC) is an actuation architecture that has been introduced to amplify the deflection cased by piezo-electric effect. The active part is due to PZT5A fibers. PZT5A fibers are embedded in the Epoxy matrix and are aligned along the longitudinal direction. The electric field is applied to PZT5A fiber through the aluminum electrode fingers that are placed on the top and bottom of the fibers. Aluminum electrode fingers are aligned perpendicular to the longitudinal direction of fiber in the width direction of AFC patch. Electrodes that are placed on the top and bottom in the thickness direction of the AFC patch have the same electric potential. Therefore, the electric field on the central plane of the AFC is zero. Electrodes that are adjacent to each other in the longitudinal direction of the AFC have the opposite electric potentials. As a result, an electric field is formed in the longitudinal direction

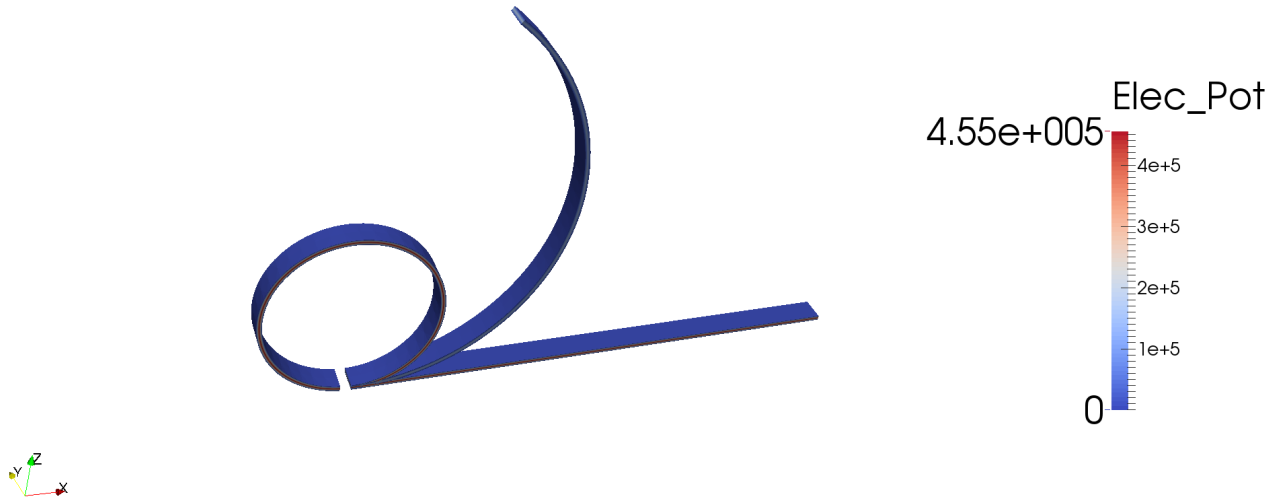


Figure 4.7: Folding of bimorph PVDF beam under very high electric potential

of fibers. The electric field in the gap between electrodes is directly proportional to the value of applied potential. The electric field in the gap between electrodes is inversely proportional to the gap distance between electrodes. An example of AFCs is shown in figure 4.9. Schematic for the placement of fibers and electrodes is shown in 4.8 [34].

The configuration of AFC patch is symmetric with respect to its thickness direction. Moreover, there is a periodic pattern in the placement of fibers, electrodes and matrix in the longitudinal direction of AFC. Due to this symmetry and periodic configuration, a unit cell model for AFC is defined as a representative microstructure. This unit cell can present the overall electro-mechanical behavior of AFC.

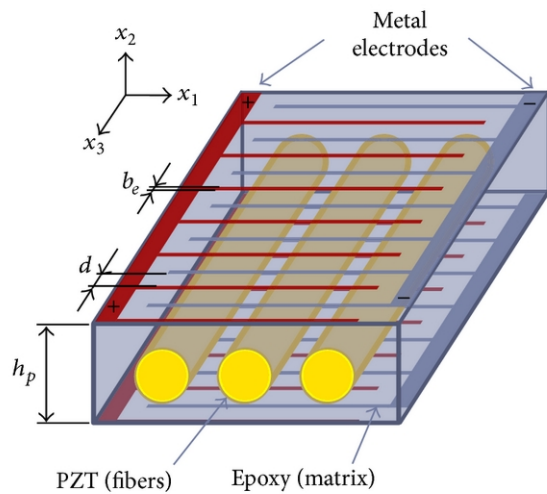


Figure 4.8: Schematic for placement of Fibers and electrodes in the Epoxy matrix [34]



Figure 4.9: Active Fiber Composite and applying electric potential

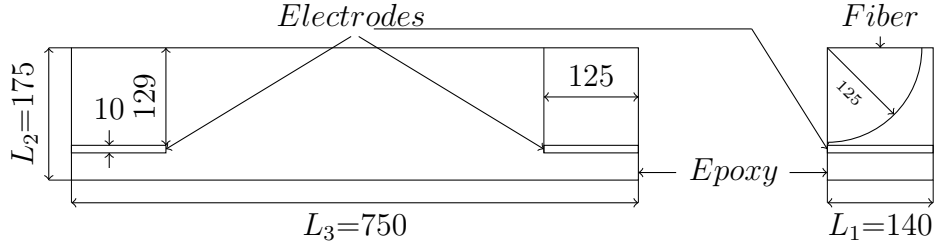


Figure 4.10: Geometry of Unit Cell (dimensions are in μm)

4.3.1 Unit Cell of an Active Fiber Composite

The smallest possible unit cell of AFC is considered in order to simulate its overall behavior. This unit cell contains one quarter of the fiber in the space between two electrodes. This unit cell of AFC is shown in figure 4.10. It is a cubical domain with dimensions of $L_1 \times L_2 \times L_3 = 140\mu m \times 175\mu m \times 750\mu m$. A PZT5A fiber with the radius of $125\mu m$ is embedded in Epoxy matrix as shown in figure 4.10 (right). Two Aluminum electrodes can be seen in the unit cell under the fiber with thickness of $10\mu m$. Each Aluminum electrode finger is $250\mu m$ long due to periodicity of the microstructure only half of each electrode is considered in the unit cell. There is $500\mu m$ gap between two electrodes that is filled with Epoxy. Moreover, there is $4\mu m$ vertical threshold between the electrodes and PZT5A fiber that is filled with Epoxy. The electric potential applied to the Aluminum electrodes induces electric field inside the Epoxy and also inside the PZT5A fiber.

The mechanical response of Epoxy is considered to be linear visco-elastic. The Epoxy is assumed to have very small electro-mechanical coupling that can be excluded from the analyses. The electric potential is transferred from the electrodes to fibers through the Epoxy. Therefore, the dielectric properties of Epoxy has significant effect on overall electro-mechanical properties of AFC [9]. The electric potential

are applied to the two aluminum electrodes which, are shown in the unit cell in the figure 4.10. The embedded aluminum electrodes have $10\mu m$ thickness. It is noted that only half of each electrode is considered in this unit cell. The length of each electrode is $250\mu m$. Two electrodes that are considered in the unit cell are charged with electric potential with an opposite sign. The response of Aluminum on the AFC is assumed to be linear a elastic.

The periodic and symmetric boundary conditions are applied to the unit cell in order to model the effective behavior of AFC. The boundary conditions prescribe on the unit cell of AFC are given as follows:

$$\begin{aligned} x_1 = -\frac{L_1}{2}, \quad u_1 = 0, \quad \frac{\partial\phi}{\partial x_1} = 0 & ; \quad x_1 = \frac{L_1}{2}, \quad u_1 = \bar{u}_1, \quad \frac{\partial\phi}{\partial x_1} = 0 \\ x_2 = -\frac{L_2}{2}, \quad u_2 = 0, \quad \frac{\partial\phi}{\partial x_2} = 0 & ; \quad x_2 = \frac{L_2}{2}, \quad u_2 = \bar{u}_2, \quad \frac{\partial\phi}{\partial x_2} = 0 \\ x_3 = -\frac{L_3}{2}, \quad u_3 = 0, \quad \frac{\partial\phi}{\partial x_3} = 0 & ; \quad x_3 = \frac{L_3}{2}, \quad u_3 = \bar{u}_3, \quad \frac{\partial\phi}{\partial x_3} = 0 \end{aligned} \quad (4.28)$$

where the geometry of the unit cell is defined in $x_1 \in [-L_1/2, L_1/2]$, $x_2 \in [-L_2/2, L_2/2]$, $x_3 \in [-L_3/2, L_3/2]$.

The matrix, electrodes and fibers are glued together. It is assumed that the glue has the same mechanical and electrical properties as the Epoxy. Only the piezoelectric fiber experiences electro-mechanical coupling due to the applied electric field. The strain induced inside the fiber causes deformations of the unit cell. The visco elastic properties of the Epoxy and the time dependent electro-mechanical response of piezo electric fiber can affect the overall deflection of the unit cell. The finite element analyses for nonlinear time-dependent electro-mechanical response are used to simulate and predict the behavior of AFC.

The electric potential is applied to the electrodes in the unit cell. The material properties that are taken for PZT5A fiber, Epoxy matrix and aluminum electrodes

Table 4.3: Material Properties of AFC

	PZT5A	Epoxy	Aluminum	
Young's Modulus	60.06	1.5	69	GPa
Poisson's Ratio	0.3	0.35	0.33	
e_{113}	-59.5			C/m^2
e_{311}	8.00			C/m^2
e_{333}	-27.196			C/m^2
$\kappa_{11} = \kappa_{22}$	4	8.854		pF/m
κ_{33}	2	8.854		pF/m
${}^0K_{ijk}^e$	1.0			
${}^1K_{ijk}^e$	-0.45			
${}^0\lambda_{ijk}^e$	0			s
${}^1\lambda_{ijk}^e$	1.5			s
${}^0K_{ijkl}^c$		1.0		
${}^1K_{ijkl}^c$		0.4		
${}^0\lambda_{ijkl}^c$		0		s
${}^1\lambda_{ijkl}^c$		0.8		s

are presented in table 4.3. The distribution of electric potential is shown in figure 4.11. In this picture the positive and negative electric potentials applied to the unit cell are shown.

4.3.2 Validating The AFC Model with Experiment Data

The finite element analyses for AFC unit cell is validated with the existing experimental results. The detailed experimental procedure is discussed in [On the temperature and time dependence of the electro-mechanical properties flexible active fiber composites]. In order to calibrate the properties of PZT, line between two peaks of the hysteresis curve from experimental data is used to find the linear and time independent material properties. The material properties Epoxy and Aluminum are taken from [9]. The Aluminum as considered elastic and its material property is taken from [1]. Then, the width of hysteresis curve is used as a reference to choose

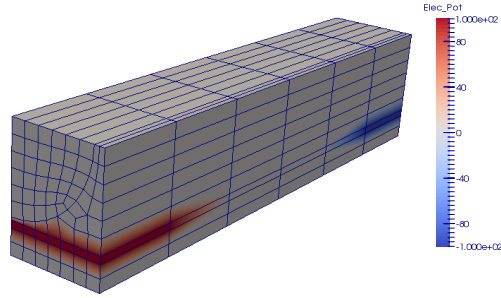


Figure 4.11: Active Fiber Composite distribution of electric potential in its unit cell

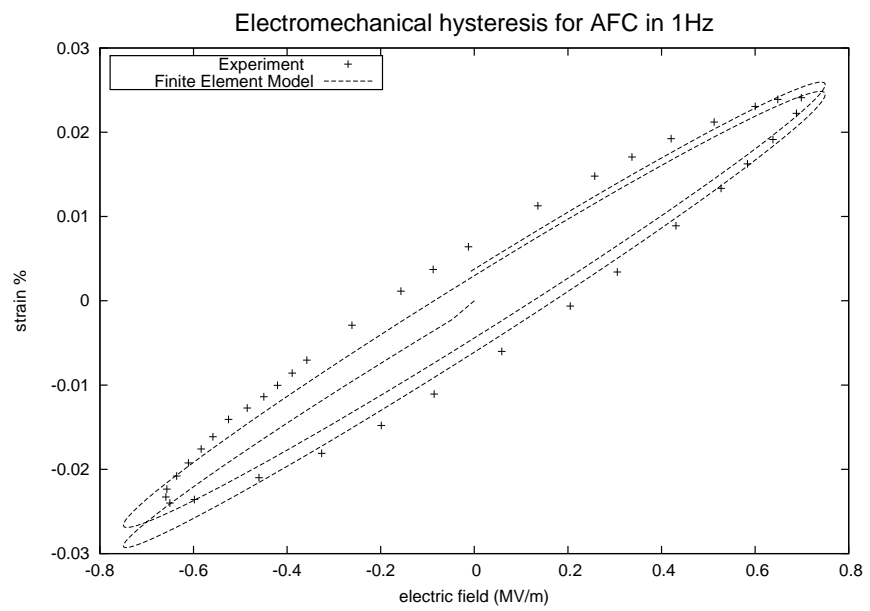


Figure 4.12: Electro-mechanical hysteresis at 1Hz compared with experiment

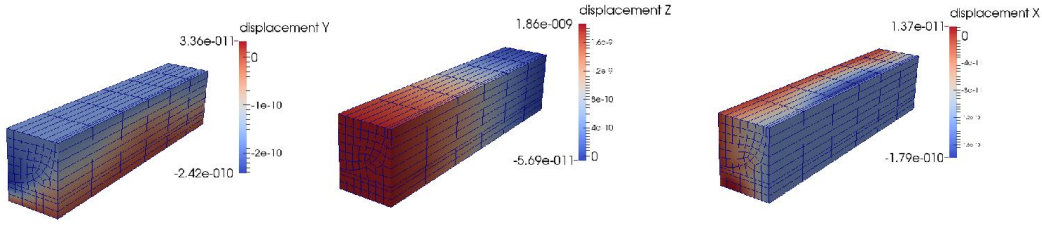


Figure 4.13: Displacement field distribution in unite cell of AFC in mm

the Proney series coefficient presented in table 4.3.

The comparison between experimental results and results from finite element analyses with linear time dependent electro-mechanical coupling for PZT is shown in figure 4.12. The hysteresis response shown in the deflection of this unit cell is due to the time dependent response of the Epoxy matrix and also time dependent electro-mechanical coupling of piezo-electric fiber. There is good comparison between the experiments and finite element analyses. The distribution of displacement field in the unit cell is shown in figure 4.13. As it is expected the value of displacement in longitudinal (displacement Z) is significantly larger than the other two directions.

At higher amplitudes of electric field AFC shows nonlinear and time dependent response due to nonlinear electromechanical coupling. This effect is simulated using the QLV model that has been disuses in the previous chapters. A polynomial for the nonlinear electric field is considered. The material parameters for this model are presented in Table 4.4. It can be seen that model is in good agreement with the experimental results. The deviation between the result from experiment and numer-

Table 4.4: Nonlinear Material Properties of AFC

	PZT5A	Epoxy	Aluminum	
Young's Modulus	60.06	1.5	69	GPa
Poisson's Ratio	0.3	0.35	0.33	
e_{113}	-18.9			C/m ²
e_{311}	9.82			C/m ²
e_{333}	-8.0			C/m ²
$\kappa_{11} = \kappa_{22}$	4	8.854		pF/m
κ_{33}	2	8.854		pF/m
${}^0K_{ijk}^e$	1.0			
${}^1K_{ijk}^e$	-0.6			
${}^0\lambda_{ijk}^e$	0			s
${}^1\lambda_{ijk}^e$	1.5			s
${}^0K_{ijkl}^c$		1.0		
${}^1K_{ijkl}^c$		0.1		
${}^0\lambda_{ijkl}^c$		0		s
${}^1\lambda_{ijkl}^c$		0.8		s
\hat{b}_{3333}	1.5×10^{-5}	N/V^2		

ical results in higher amplitude of electric field could be due to effect of polarization switching in some parts of piezoelectric fiber. It is noted that in the AFC and distribution of electric potential inside the fiber is not uniform. In some part of fiber where the intensity of electric field is larger than the coercive field, there is a change in polarization of PZT. This effect will cause large deviation between the result from the current analyses for minor effect.

4.3.3 The effect of scale time on electro mechanical response of AFC

It can be shown that at higher intensity of electric field the piezoelectric materials respond faster to the change in electric field. We use the same analogy with thermorheologically simple materials that have widely used for mechanical response of polymers [29, 74]. The time scale factor is defined as an exponential function with respect to the electric field intensity $|\mathbf{E}|$. Then the

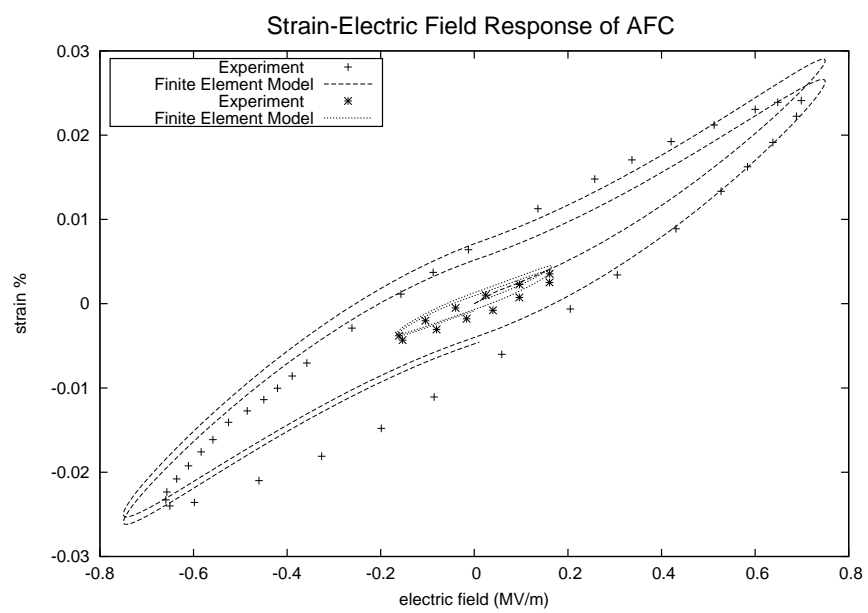


Figure 4.14: Nonlinear electro-mechanical hysteresis for different electric fields at 1Hz compared with experiment

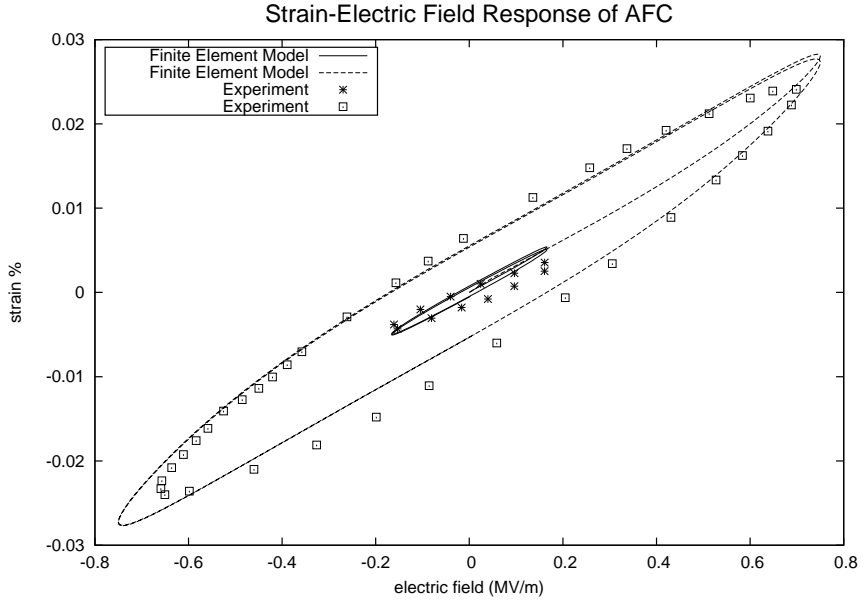


Figure 4.15: Linear electro-mechanical hysteresis response of AFC model with time shift for different electric fields at 1Hz compared with experiment

$$\Delta t_{scaled} = \frac{\Delta t}{a(|\mathbf{E}|)} \quad (4.29)$$

where $a(|\mathbf{E}|)$ is the time shift factor that is defined with respect to norm of electric field vector and a material constant.

$$a_{|\mathbf{E}|} = e^{-\gamma_E \times |\mathbf{E}|} \quad (4.30)$$

Figure 4.15 shows the result of linear analyses, including the time shift concept for piezoelectric materials. The time shift material constant is taken as $\gamma_E = 1.75m/MV$ for this analyses.

In order to examine the rate (frequency) dependent response, parametric studies

are presented by applying electric fields at various frequencies. Different frequency inputs are applied to the same material constitutive model presented in this section.

The corresponding strains response of the model under different frequencies and amplitudes are shown in Figure 4.16. It is apparent from the results that higher frequency of loading reduces time-dependent (hysteresis) effect. This is due to the fact that the material does not have enough time to exhibit time-dependent effect. Fast loading reduces the creep-like or relaxation-like behavior and the area inside the hysteresis curve becomes smaller. Even for small frequencies of applied electric field the response of AFC is faster in higher electric field. This is due to inclusion of time shift in the model. This is the main reason for the pointy shape of hysteresis curves in smaller frequencies.

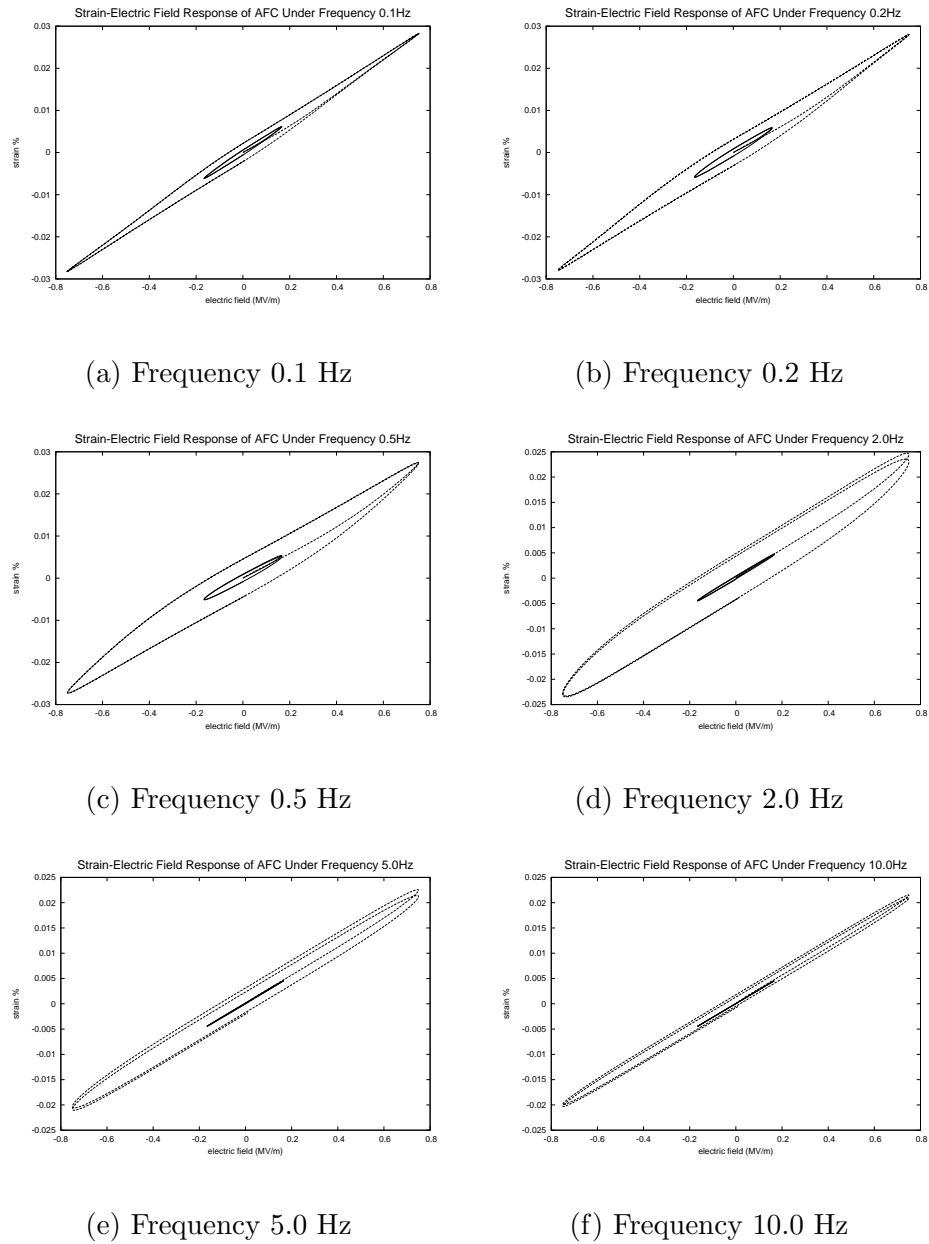


Figure 4.16: Effect of frequency of applied electric field on strain response of AFC

5. ACTIVE TRUSSES

Simulations of shape changing in active truss structures are discussed in this chapter. Finite element analyses of 3D truss system are presented in order to incorporate both material and geometric nonlinearities. Two truss systems, namely planar truss and tetrahedral truss are considered. Shape changing in these truss systems are controlled by an actuation of each truss component using a piezoelectric actuation. The embedded actuation in as an effective strategy that is capable of matching these key kinematic features for active trusses and tensegrity-based structures are explored and compared by Moored [54]. In his paper, Moored [54] derived analytical solutions for active planar tensegrity structures for design of an artificial pectoral fin.

5.1 Deformed Shapes

Consider a 3D continuum object in reference configuration X_i . This continuum object change its shape from the reference X_i configuration to current configuration x_i . In the case of Lagrangian description, the current configuration is defined as a function of reference configuration:

$$x_i = \chi(X_i) \quad (5.1)$$

Since the new configuration is decided apriori, the mapping function $\chi(X_i)$ is defined and the gradient of deformation is known:

$$F_{ij} = \frac{\partial x_i}{\partial X_j} \quad (5.2)$$

The strain corresponding due to the induced deformation in the truss system is easily

calculated. The Green-St. Venant strain is given as:

$$E_{KL} = \frac{1}{2} \left(\frac{\partial x_j}{\partial X_K} \frac{\partial x_j}{\partial X_L} - \delta_{KL} \right) \quad (5.3)$$

In order to induce the desired strain, as calculated above, in each truss member, an electric field is prescribed to the truss member. The deformation in each truss member is considered only along the longitudinal axis of each truss. Thus the constitutive relation for each truss is:

$$E_{11} = f_1(S_{11}) + f_2(E_3) \quad (5.4)$$

where E_{11} is the axial strain due to longitudinal axis of each truss member, $f_1(S_{11})$ is the strain due to the mechanical stress and f_2 is the strain due to the electric field input. In order to achieve desired shapes in the truss system, either stress or electric field, or both stress and electric field can be prescribed. The chosen constitutive relation is discussed later in this chapter.

5.2 Nonlinear Truss Finite Element

Truss systems consist of relatively slender members connected by joints. The joints connect the translations and allow the members to rotate with respect to each others. Each truss element is specified by two joints in the space and the line that connect these two joints. Let us consider these two joints P_1 and P_2 . The location of these two joints in the reference configuration is defined by two vectors namely \mathbf{X}^{P_1} and \mathbf{X}^{P_2} . The vector that connects these two joints in the reference configuration is defined as:

$$\mathbf{V}^{12} = \mathbf{X}^{P_2} - \mathbf{X}^{P_1} \quad (5.5)$$

and the base vector in the direction that connects these two joint is:

$$\mathbf{N}^{12} = \mathbf{V}^{12}/\|\mathbf{V}^{12}\| \quad (5.6)$$

The displacement from the reference to the current configurations is defined in terms of displacement of each node with respect to the reference configuration:

$$u_i^{P_1} = x_i^{P_1} - X_i^{P_1}; u_i^{P_2} = x_i^{P_2} - X_i^{P_2}; \quad (5.7)$$

If the linear test functions are used for the finite element approximation, the displacement at each point on the truss can be interpolated as a linear function. In the case of linear interpolation of variables and also geometry, the master shape function of the isoparametric element $[-1, 1]$ is introduced as:

$$\begin{aligned} \psi^1 &= 0.5(1 + \zeta); \psi_{,\zeta}^1 = 0.5 \\ \psi^2 &= 0.5(1 - \zeta); \psi_{,\zeta}^2 = -0.5 \end{aligned} \quad (5.8)$$

The mapping must be defined from each truss element into this master element. The global deformation gradient is:

$$\frac{\partial u_i}{\partial X_j} = \frac{\partial u_i}{\partial \zeta} \frac{\partial \zeta}{\partial X_j} \quad (5.9)$$

For the truss element in 3D we define the gradient of deformation as follows:

$$\frac{\partial X_j}{\partial \zeta} = \sum_{i=1}^{NPE=2} \psi_{,\zeta}^i X_j^{P_i} \quad (5.10)$$

where NPE is the number of joints in an element. It is noted that the integration is done on the member that connects two joints of the truss element. Then the

deformation gradient in a point on the truss is defined as:

$$F_{ij} = \delta_{ij} + \frac{\partial u_i}{\partial X_j}; \quad (5.11)$$

The tensor $\frac{\partial u_i}{\partial X_j}$ in each integration point is approximated by equation (5.9). Then the strain is obtained by equation (5.3). The finite element approximation for 3D truss developed will be same as in the previous chapter. In the geometric nonlinear analyses the derivative of strain with respect to the degrees of freedom will include the nonlinear terms of strain. The nonlinear terms will be added to equation (3.41) as follows:

$$\frac{\partial \delta \varepsilon_{ij}}{\partial \delta d_k} = \frac{\varphi_{ik,j} + \varphi_{jk,i} + \sum_{m=1}^3 u_{m,i} \frac{\partial \delta u_{m,j}}{\partial \delta d_k} + \sum_{m=1}^3 u_{m,j} \frac{\partial \delta u_{m,i}}{\partial \delta d_k}}{2} \quad (5.12)$$

5.2.1 Space Filler Truss Configuration

The first example that is considered is the planar truss. The truss is formed by the cubical element as a building block. A single element that forms truss system is shown in figure 5.1. The element consists of 12 side truss members and 4 diagonal members. The deformation of the members can be controlled by the electric field or other stimuli. The change in the length of each member will cause change of shape of each single cubical element and consequently change in shape of the structure that is made of these members.

As an example, consider a planar domain that is in the form of a plate structure. The domain is defined as follows:

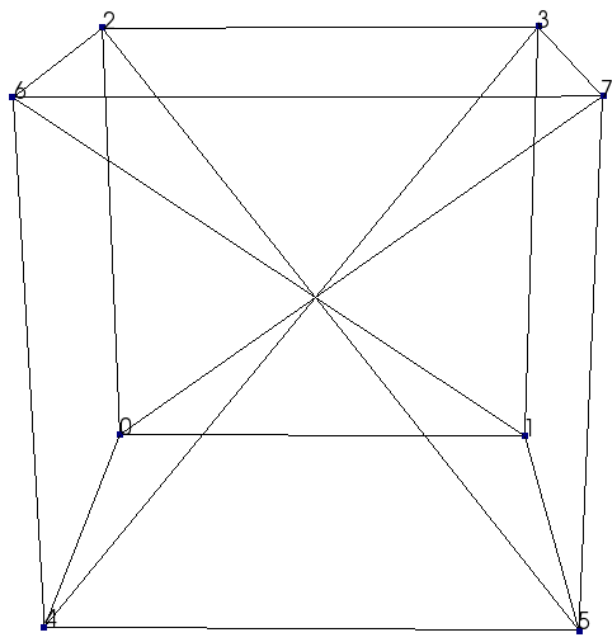


Figure 5.1: One element of space filler truss

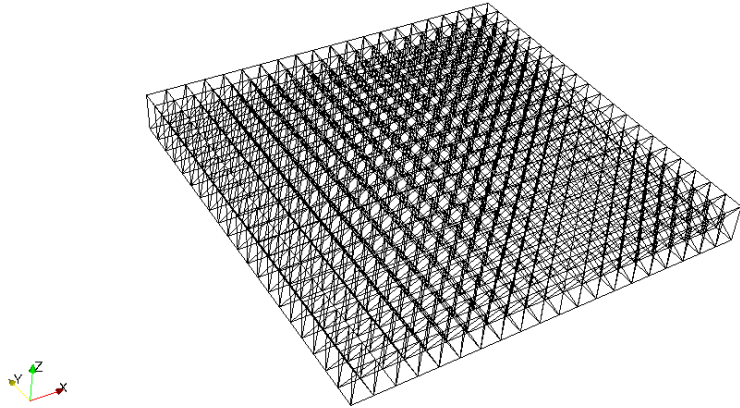


Figure 5.2: Planar Truss in Reference Configuration

$$X_1 \in [-L_1/2, L_1/2]$$

$$X_2 \in [-L_2/2, L_2/2] \quad (5.13)$$

$$X_3 \in [-h/2, h/2]$$

We take $[L_1, L_2, h] = [1, 1, 0.1]$ in meter, and fill the domain with 20 elements in X_1 and X_2 directions and 1 element in X_3 direction. The planar truss is shown in figure 5.2. To examine the performance of the method a doubly surface shape $z = xy$ is considered. This shape is shown in figure 5.3

The mapping between the reference and current configurations for $z = xy$ surface is defined as following.

$$\begin{aligned} x_1(X_1, X_2, X_3) &= X_1 \\ x_2(X_1, X_2, X_3) &= X_2 \\ x_3(X_1, X_2, X_3) &= X_3 + X_1 X_2 \end{aligned} \quad (5.14)$$

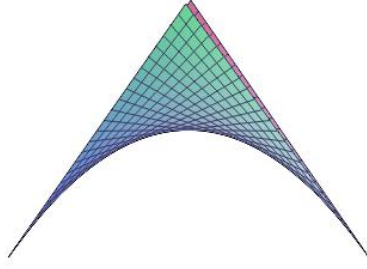


Figure 5.3: The desired current configuration for the planar truss

The deformation gradient for this deformation is defined as:

$$\mathbf{F} = \begin{bmatrix} 1 & 0 & 0 \\ 0 & 1 & 0 \\ X_2 & X_1 & 1 \end{bmatrix} \quad (5.15)$$

Then the stretch tensor $\mathbf{C} = \mathbf{F}^T \mathbf{F}$ and Green-St. Venant strain tensors are:

$$\mathbf{C} = \begin{bmatrix} X_2^2 + 1 & X_1 X_2 & X_2 \\ X_1 X_2 & X_1^2 + 1 & X_1 \\ X_2 & X_1 & 1 \end{bmatrix}; \mathbf{E} = \begin{bmatrix} X_2^2 & X_1 X_2 & X_2 \\ X_1 X_2 & X_1^2 & X_1 \\ X_2 & X_1 & 0 \end{bmatrix} \quad (5.16)$$

It is shown in figure 5.4 that the application of stimuli to each truss element based on equation represented for shape change can induce desired shape into a structure made of smart trusses. The space filler truss that has been discussed in the previous chapter can offer good flexibility for planar and even 3D shapes. The length of all truss members are not equal in this truss configuration. Moreover, in the center of each truss members the elements truss members are crossing and this will reduce the

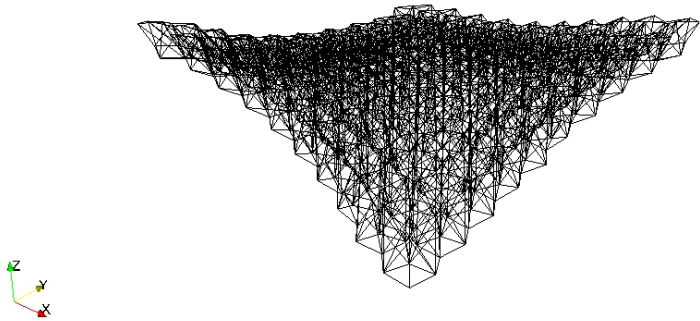


Figure 5.4: The deformed configuration for the planar truss

feasibility of this truss configuration.

5.2.2 Tetrahedral Beam Like Truss

Using simplex as a truss configuration we can arrange the truss elements to take a beam like form. The building block of the tetrahedral beam like truss is shown in figure 5.5 that contains 3 tetrahedron. The beam like truss is formed by arranging these tetrahedral units in one direction. An example of truss with 150 tetrahedral units is shown in 5.6. It can be seen from the cross section view of the beam in figure 5.7 that none of the truss members crosses the center line. Therefore, this configuration behaves like a hollow beam. An example of bending deformation is considered for the truss system.

The bending can be induced by creating normal strain in the longitudinal direction of the beam. In the simple bending case the radius of curvature of the beam $r_{curvature}$ is defined:

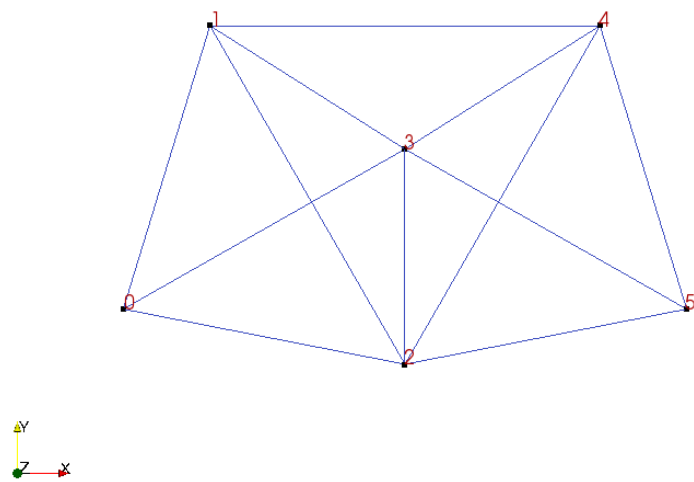


Figure 5.5: The Building block of Tetrahedral beam like Truss



Figure 5.6: Tetrahedral beam like Truss with 150 Units that is Used as Reference Configuration

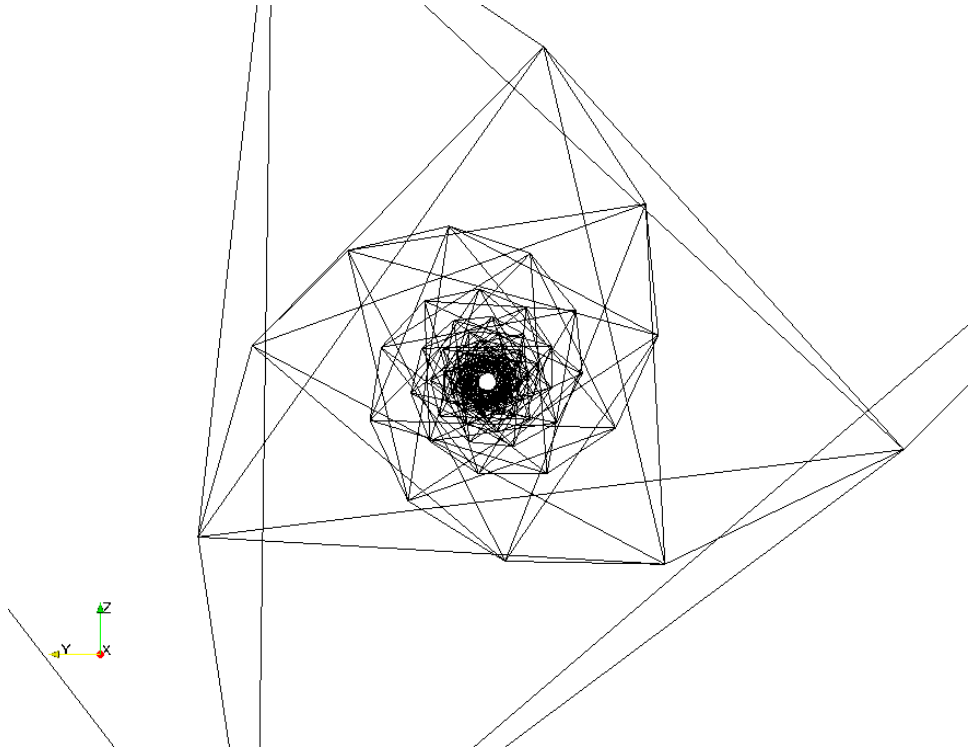


Figure 5.7: Cross Section View of Tetrahedral beam like Truss (perspective view)

$$r_{curvature} = \frac{L_{beam}}{2\theta} \quad (5.17)$$

$$E_{11} = X_3/r_{curvature}$$

where θ is the curvature angle (for full circle it is 2π) and L_{beam} is the length of the beam made of tetrahedral units. The strain $E_{11} = X_3/r_{curvature}$ causes lateral deformation in the X_3 direction with positive curvature.

We try to produce the shape of an arc with a curvature angle π . The result is shown in figure 5.8. As it can be seen the shape is very different from the real arc. The reason of the difference between the produced shape and desired shape is disregarding normal strain in the thickness direction of beam that is produced in bending of a beam. Increasing the curvature in the tetrahedral beam like truss will

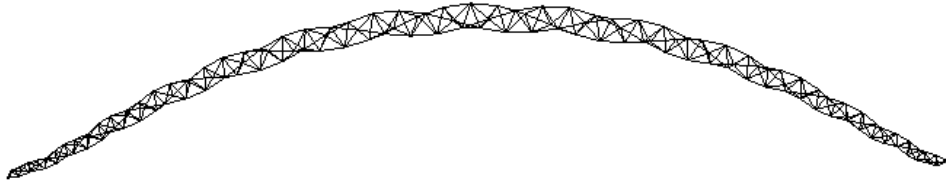


Figure 5.8: Arc shape produced in the tetrahedral beam like truss

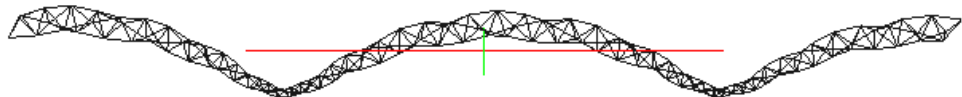


Figure 5.9: Cyclic shape produced in the tetrahedral beam like truss

cause a cyclic shape in the truss. The strain that is induced in this truss is taken from equation (5.17) with $\theta = 2\pi$.

In order to get a shape closer to the actual bending of a beam we apply the normal strain in the thickness direction too. This will cause a strain field closer to the real beam made of continuous solid members. We modify the bending strain defined in equation (5.17) with the though thickness normal strain as follows:

$$\begin{aligned} E_{11} &= X_3/r_{curvature} + \kappa_v \\ E_{22} &= -X_3/(2r_{curvature}) + \kappa_v \\ E_{33} &= -X_3/(2r_{curvature}) + \kappa_v \end{aligned} \quad (5.18)$$

where κ_v is the dilation that is added to mimic the effect of change in volume in the beam. It is observed that if $\kappa_v = 2.0$ there will be an arc forming in the beam like truss. This arc is shown in figure 5.10.

In the last example we will try to apply a shape in the beam in the way that it passes four specific points. Consider bending tetrahedral beam like truss in the way

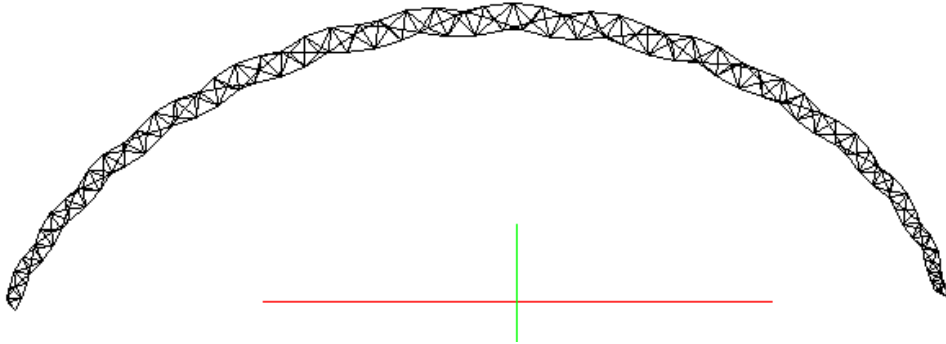


Figure 5.10: Shape produced in the tetrahedral beam like truss including the all normal strains

that it passes through three points as follows:

$$\begin{aligned}
 \underline{X}^1 &= (0, 0, 0) \\
 \underline{X}^2 &= (L_{beam}/4, 0, L_{beam}/8) \\
 \underline{X}^3 &= (3L_{beam}/4, 0, -L_{beam}/8) \\
 \underline{X}^4 &= (L_{beam}, 0, L_{beam}/8)
 \end{aligned} \tag{5.19}$$

In this case it can be found that the following strain should be applied:

$$E_{11} = X_3 \left(\frac{329}{36L_{beam}} - \frac{220X_1}{L_{beam}^2} + \frac{280X_1}{3L_{beam}^3} \right) \tag{5.20}$$

5.2.3 Effect of Nonlinear and Time Dependent Constitutive Equation on Active Truss

Prescribing this strain field to the truss structure, the desired shape is attained. The corresponding strain in each truss element is achieved through application of electric field to the piezoelectric materials in the truss. In the case of piezoelectric patch with the electro-mechanical coupling factor d_{311} the electric field that should

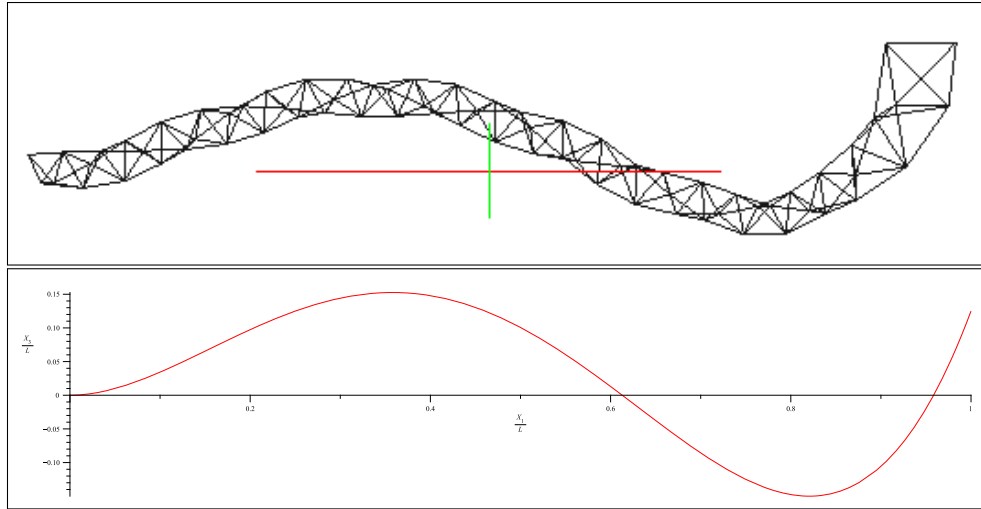


Figure 5.11: Shape of tetrahedral beam that passes thought four specific points

be applied to each truss E_3 can be found from the following equation:

$$e_{truss} = E_{ij} N_i^{truss} N_j^{truss} \quad (5.21)$$

$$e_{truss} = E_3 d_{311}$$

where N^{truss} is the vector in the direction of each truss element and e_{truss} is the electric field that should be applied to each truss element to apply the deformation. When a nonlinear electro-mechanical constitutive equation is considered, the strain in the longitudinal axis of each truss is $e_{truss} = (\text{nonlinearequation})$. The relationship between the strain and electric field can also be taken as time dependent to include hysteresis response of piezoelectric materials.

The effect of nonlinear and time dependent electro-mechanical response of each truss member on the overall deformation of truss structure is examined. The time dependent constitutive equation based on quasi linear viscoelastic model that was introduced in previous chapters is used. The beam like tetrahedral truss is used for these analyses and the desired shape is taken to be an arc with arc angle of $\pi/2$.

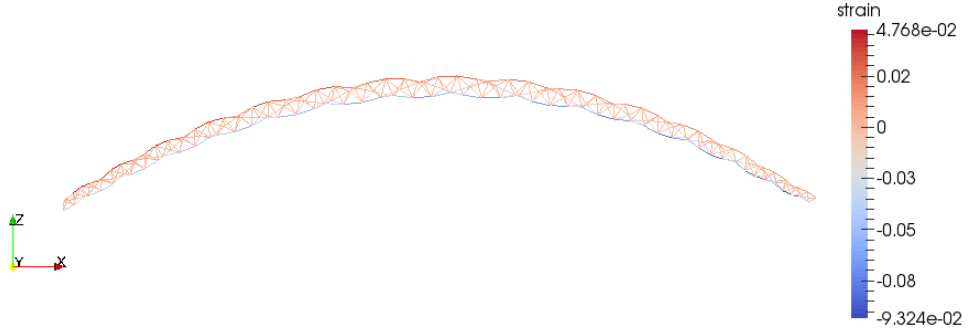


Figure 5.12: The strain distribution in a beam like tetrahedral truss in the arc configuration

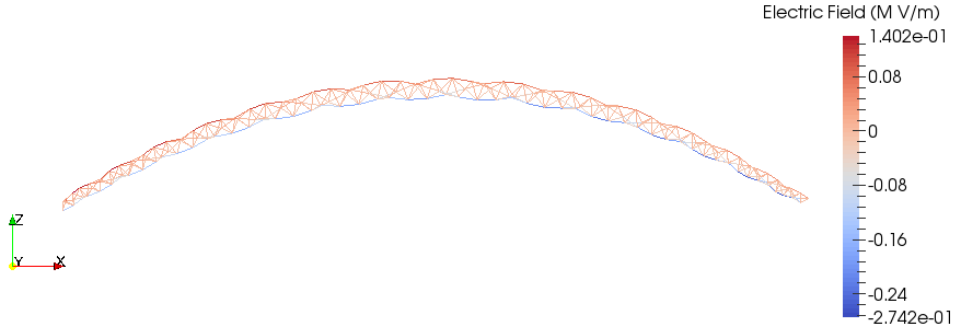


Figure 5.13: The electric field distribution in a beam like tetrahedral truss in the arc configuration

The strain distribution for this configuration is shown in figure 5.12. If we take the electromechanical coupling factor as $d_{311}^0 = 340\text{pm}/V$ the corresponding required electric field contour for each truss shape is shown in 5.13.

At first the analyses is conducted for a linear constitutive model for the truss. The coupling between the stimuli and strain in the truss members are taken to be linear and independent of time. The relationship between the input stimuli and maximum deflection in the middle of beam like tetrahedral beam in this analyses is shown in figure 5.14. The stimuli is applied to each truss member with the frequency of 1Hz.

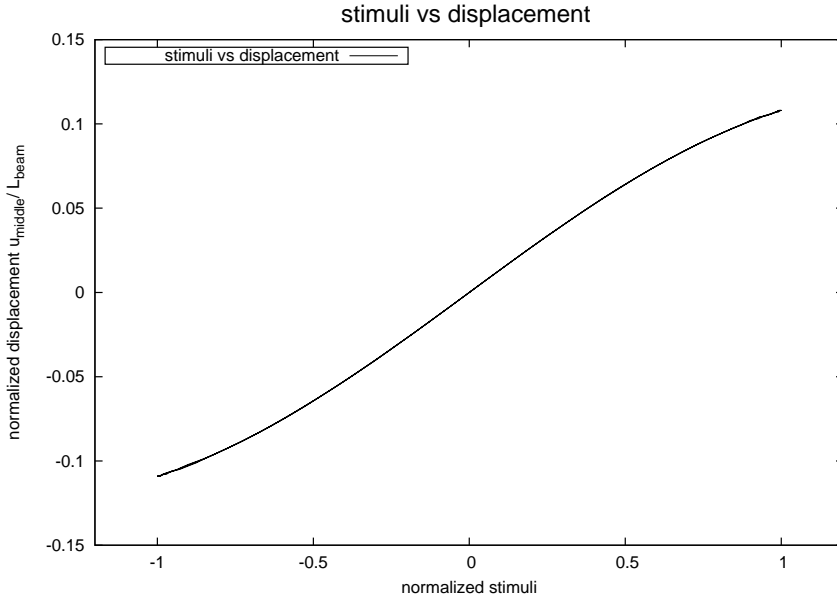


Figure 5.14: linear and time independent model for deflection under frequency 1Hz

The nonlinear relationship between the deflection and input stimuli that is shown in figure 5.14 is mainly due to geometric nonlinearity.

In case the time dependent electro-mechanical response, a cyclic electric field input with frequency 1Hz is prescribed. The time kernel function with $K(t) = 1.0 - 0.6\exp(-t/1.2)$ is considered within the integral representation for the strain $\varepsilon_{11}(t) = \int_0^t K(t-s) \frac{\partial \varepsilon_{11}}{\partial E_3} \frac{\partial E_3(s)}{\partial s} ds$ with $\frac{\partial \varepsilon_{11}}{\partial E_3} = -d_{311}$ taken to be 340pm/V. The hysteresis between the input stimuli and deflection is shown in figure 5.15.

We follow the same approach as previous chapters and assume the nonlinear and time dependent response for the constitutive equation in each truss element. We define a nonlinear response function $\varepsilon_{11}(E_3) = -d_{311}^0 E_3 - d_{311}^1 |E_3| E_3$. Here we take

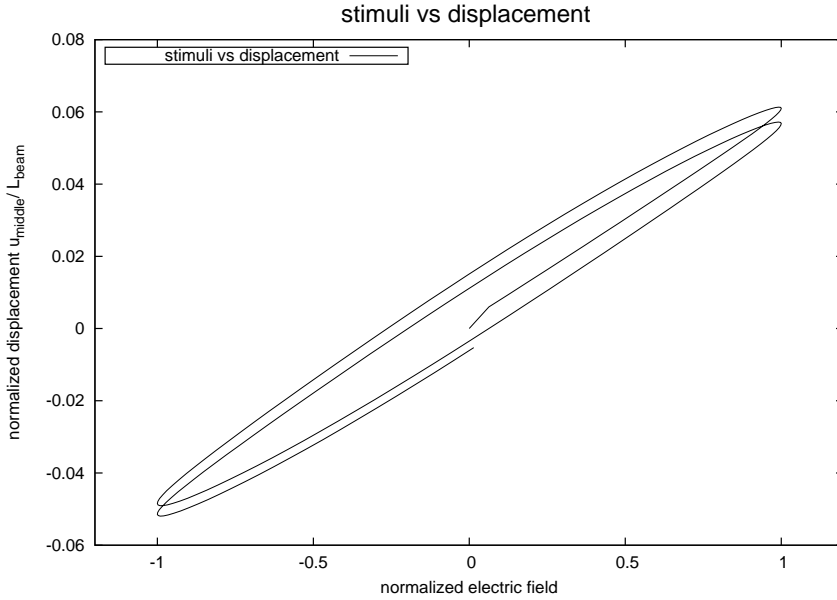


Figure 5.15: linear and time dependent response for deflection under frequency 1Hz

$d_{311}^0 = 340 \text{pm/V}$ and¹ $d_{311}^1 = 0.02 \text{fm}^2/\text{V}^2$. The results from taking a nonlinear and time dependent electric coupling between electric stimuli and resulting strain is shown in figure 5.16. The hysteresis curve shown in figure 5.16 combines the nonlinear response both from the large geometry and also from the nonlinear constitutive equation between strain and applied electric field in each truss.

In figure 5.17 the configuration of the truss in four different values of electric stimuli is shown.

As it can be seen from figures 5.12 and 5.13 the applied strain and therefore electric field can be beyond the limits of material. With a little investigation on the location of maximum strain it has been postulated that even with the limiting

¹f here stands for femto i.e. 10^{-15}

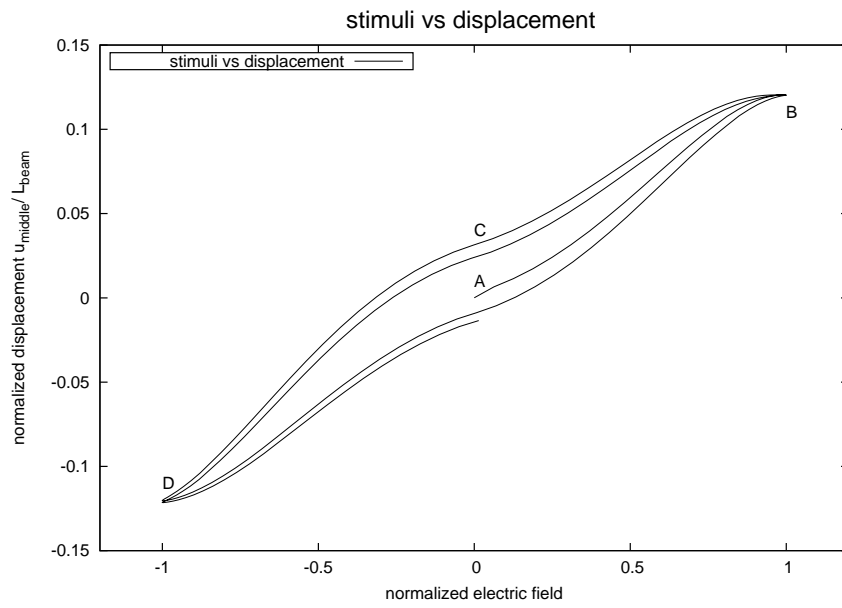


Figure 5.16: nonlinear and time dependent response for deflection of beam like truss under frequency 1Hz

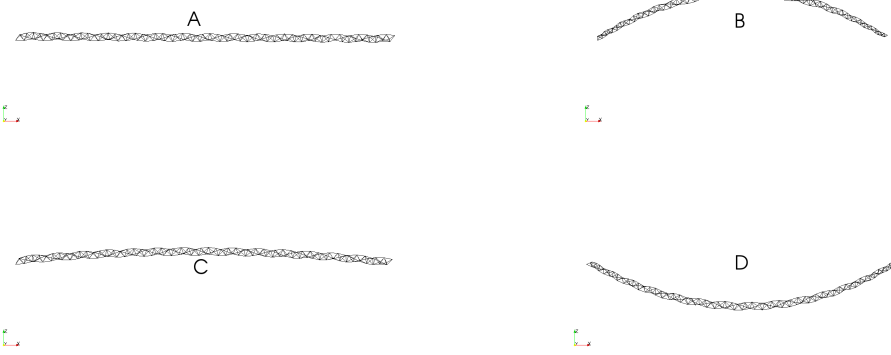


Figure 5.17: The snapshots of linear tetrahedral truss in configurations labeled in figure 5.16

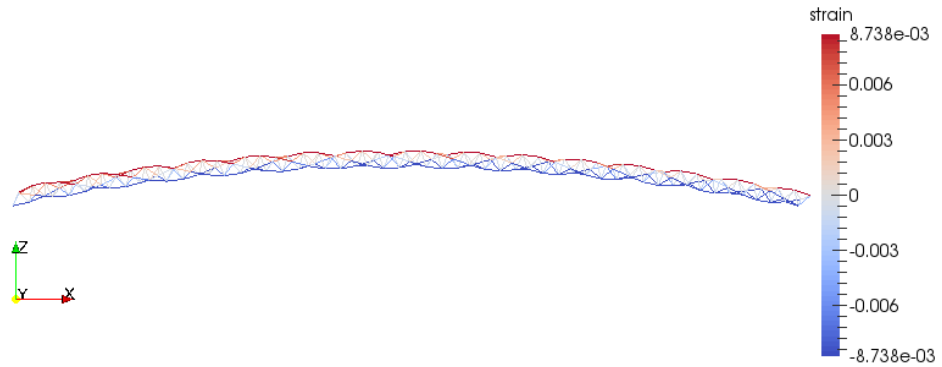


Figure 5.18: The strain distribution in a beam like tetrahedral truss in the arc configuration with limiting strain 1%

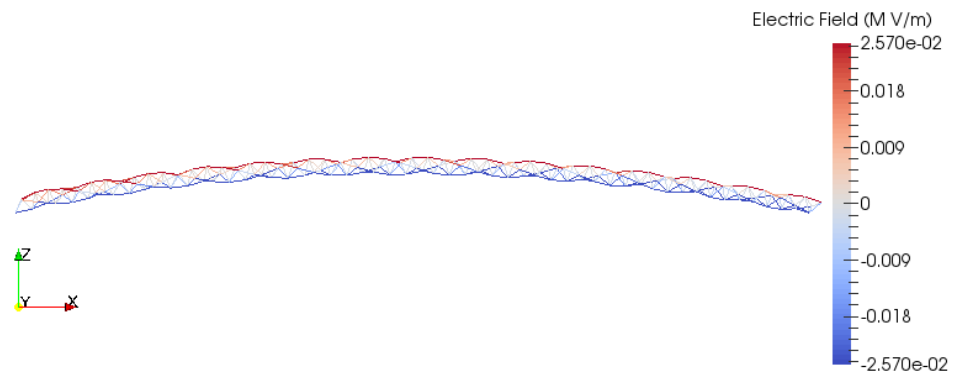


Figure 5.19: The electric field distribution in a beam like tetrahedral truss in the arc configuration with limiting strain 1%

amount of strain it is still possible to get the same shape. The 1% strain is chosen as maximum applicable strain. As a result of limiting strain the resulting shape will change slightly. The resulting shape with this limiting strain is shown in figure 5.18.

Moreover, less electric field will be needed for the actuation as it is shown in figure 5.19

Application of limiting strain in the model will decrease the maximum overall

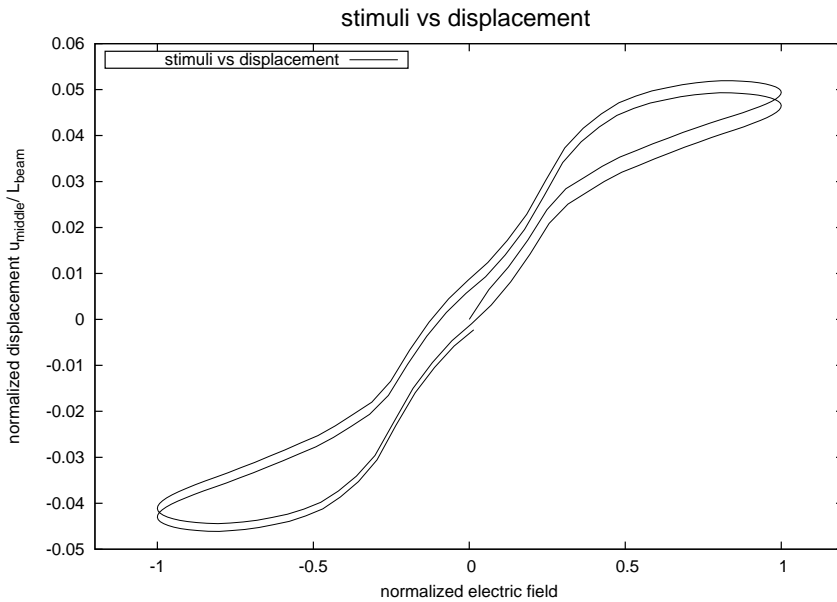
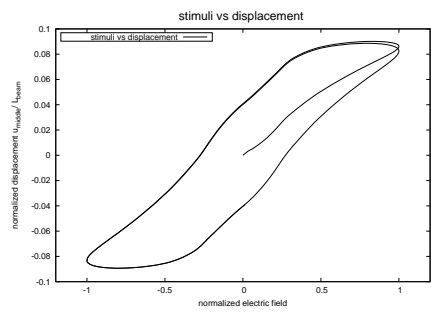


Figure 5.20: nonlinear and time dependent response for deflection of beam like truss under frequency 1Hz with limiting strain

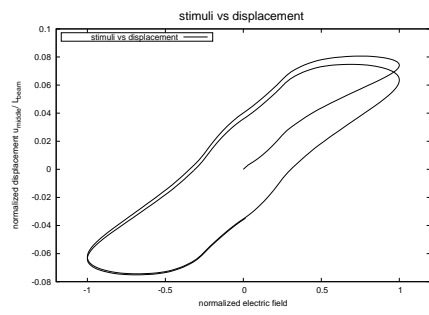
deflection of truss. This will also change the shape of hysteresis curve as it is shown in figure 5.20.

In order to examine the rate (frequency) dependent response, parametric studies are presented by applying electric fields at various frequencies. Different frequency inputs are applied to the same material constitutive model presented in this section.

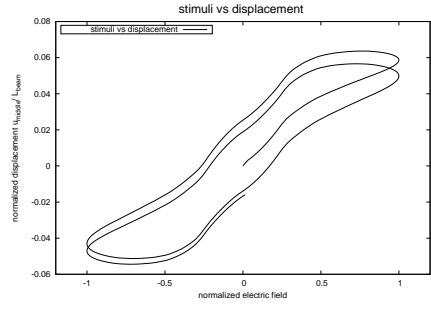
The corresponding strains response of the truss under different frequencies and amplitudes are shown in Figure 5.21. It is apparent from the results that higher frequency of loading reduces time-dependent (hysteresis) effect. This is due to the fact that the material does not have enough time to exhibit time-dependent effect. In higher frequency the response is very similar to the non rate dependent analysis.



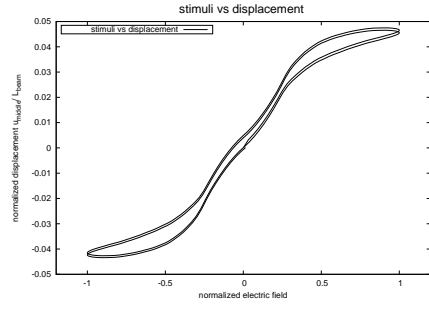
(a) Frequency 0.1 Hz



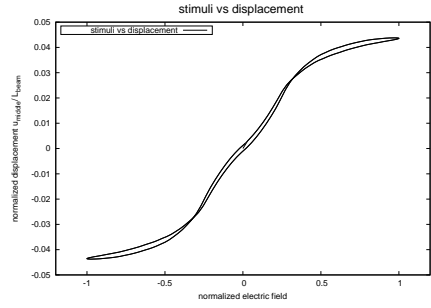
(b) Frequency 0.2 Hz



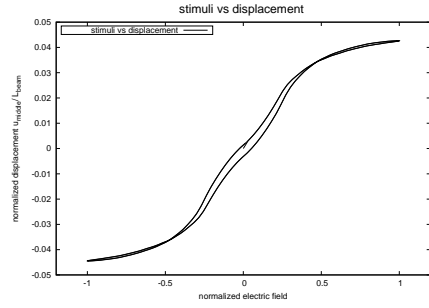
(c) Frequency 0.5 Hz



(d) Frequency 2.0 Hz



(e) Frequency 5.0 Hz



(f) Frequency 10.0 Hz

Figure 5.21: Effect of frequency of applied electric field on strain response of tetrahedral truss

6. CONCLUSION

This study presents nonlinear and time-dependent electro-mechanical analyses of piezoelectric based materials and structures. Ceramics based piezoelectric materials, such as lead zirconate titanate (PZT), are considered, and their hysteretic behaviors under various magnitude of electric-field stimulus are studied. Phenomenological constitutive models have been formulation in order to capture minor and major loops of piezoelectric ceramics under cyclic electric field inputs. A quasi-linear viscoelastic (QLV) model is adopted in order to incorporate the time-dependent effect on the nonlinear electro-mechanical response of piezoelectric ceramics. These phenomenological models are implemented in continuum 3D finite elements, which are useful for analyzing behaviors of several piezoelectric structures and structural components under various boundary conditions. A time-integration algorithm, based on linearized predictor and corrector schemes, has been developed to solve for the nonlinear time-dependent electro-mechanical response at the material and structural levels. The nonlinear time-dependent electro-mechanical models have been validated with experimental data on PZT materials and structural components such as telescopic actuators and bimorph beams.

The integrated time-dependent electro-mechanical material model and finite element analysis is also used to study the overall electro-mechanical responses of active fiber composites (AFCs). AFCs comprise of long unidirectional piezoelectric fibers embedded in polymeric matrix and placed in between two electrode fingers on the top and bottom surfaces of the AFCs. Electric fields are prescribed through the electrode fingers in order to actuate the AFCs. AFCs form flexible piezoelectric ceramics based actuators suitable for morphing, bending, and/or twisting type of

deformations. In this study, a unit-cell model of AFCs comprising of a segment of quarter fibers, epoxy matrix, and metallic electrode fingers is considered in order to reduce computational cost. The overall nonlinear electro-mechanical hysteretic responses of the unit-cell model are comparable to the ones of experimental data. The presented study on AFCs is useful in designing electro-active composites with various microstructural architectures and properties of constituents as it can give an estimate of the overall electro-mechanical responses of electro-active composites prior to manufacturing them.

Finally, the nonlinear time-dependent electro-mechanical constitutive model is integrated to 3D truss finite element and used to analyze shape changing behaviors of active truss systems. The active truss system consists of arrangements of truss elements, and some of the elements are integrated with active materials such as piezoelectric, in which shape changing in the entire truss systems is generated by activating some or all of the active elements. In this study, two types of truss arrangements are considered and deformed shapes of a truss structures are controlled by the application of electric stimuli. Parametric studies on the effect of time dependent and nonlinear constitutive equation in controlling the shapes of truss structures are conducted.

REFERENCES

- [1] Aluminium, <http://en.wikipedia.org/wiki/aluminium>.
- [2] Josu Aguirrebeitia, Carlos Angulo, Luis M Macareno, and Rafael Aviles, R.s. A metamodeling technique for variable geometry trusses design via equivalent parametric macroelements. *Journal of Mechanical Design*, 131(10):104501, 2009.
- [3] P.W. Alexander and D. Brei. Piezoceramic telescopic actuator quasi-static experimental characterization. *Journal of intelligent material systems and structures*, 14(10):643–655, 2003.
- [4] P.W. Alexander, D. Brei, W. Miao, J.W. Halloran, R.L. Gentilman, G.E. Schmidt, P.T. McGuire, and J.R. Hollenbeck. Fabrication and experimental characterization of d31 telescopic piezoelectric actuators. *Journal of materials science*, 36(17):4231–4237, 2001.
- [5] P.W. Alexander and D.E. Brei. Experimental characterization and model validation of the quasi-static performance of piezoceramic telescopic actuators. In *SPIE's 8th Annual International Symposium on Smart Structures and Materials*, pages 342–353. International Society for Optics and Photonics, 2001.
- [6] Henno Allik and Thomas J. R. Hughes. Finite element method for piezoelectric vibration. *International Journal for Numerical Methods in Engineering*, 2(2):151–157, 1970.
- [7] Eric Harold Anderson. *Piezoceramic induced strain actuation of one-and two-dimensional structures*. PhD thesis, Massachusetts Institute of Technology, 1989.

- [8] Emil V. Ardelean, Daniel G. Cole, and Robert L. Clark. High performance v-stack piezoelectric actuator. *Journal of Intelligent Material Systems and Structures*, 15(11):879–889, 2004.
- [9] Hassene Ben Atitallah, Zoubeida Ounaies, and Anastasia Muliana. A parametric study on flexible electro-active composites: Importance of geometry and matrix properties. *Journal of Intelligent Material Systems and Structures*, page 1045389X14556163, 2014.
- [10] Rafael Avilés, Goizalde Ajuria, Enrique Amezua, and Vicente Gómez-Garay. A finite element approach to the position problems in open-loop variable geometry trusses. *Finite elements in analysis and design*, 34(3):233–255, 2000.
- [11] E Bassiouny, AF Ghaleb, and GA Maugin. Thermodynamical formulation for coupled electromechanical hysteresis effects i. basic equations. *International Journal of Engineering Science*, 26(12):1279–1295, 1988.
- [12] E. Bassiouny, A.F. Ghaleb, and G.A. Maugin. Thermodynamical formulation for coupled electromechanical hysteresis effects ii. poling of ceramics. *International Journal of Engineering Science*, 26(12):1297 – 1306, 1988.
- [13] H Ben Atitallah, Z Ounaies, and A Muliana. Temperature and time effects in the electro-mechanical coupling behavior of active fiber composites. In *Proceedings of 16th US National Congress on Theoretical and Applied Mechanics USNCTAM, State College, Pennsylvania*, 2010.
- [14] A. Benjeddou. Advances in piezoelectric finite element modeling of adaptive structural elements: a survey. *Computers & Structures*, 76(1-3):347–363, 2000.
- [15] A Benjeddou, MA Trindade, and R Ohayon. New shear actuated smart structure beam finite element. *AIAA journal*, 37(3):378–383, 1999.

- [16] A. Bilbao, R. Aviles, J. Aguirrebeitia, and I.F. Bustos. A reduced eigenproblem formulation for variable geometry trusses. *Finite Elements in Analysis and Design*, 50(0):134 – 141, 2012.
- [17] E. Carrera. Theories and finite elements for multilayered, anisotropic, composite plates and shells. *Archives of Computational Methods in Engineering*, 9(2):87–140, 2002.
- [18] W. Chen and C. Lynch. A micro-electro-mechanical model for polarization switching of ferroelectric materials. *Acta Materialia*, 46(15):5303–5311, 1998.
- [19] X. Chen. Nonlinear electro-thermo-viscoelasticity. *Acta Mechanica*, 211(1-2):49–59, 2010. cited By (since 1996)3.
- [20] Edward F. Crawley and Eric H. Anderson. Detailed models of piezoceramic actuation of beams. *Journal of Intelligent Material Systems and Structures*, 1(1):4–25, 1990.
- [21] Jacques Curie and Pierre Curie. Phenomenes electriques des cristaux hemiedres a faces inclinees. *J. Phys. Theor. Appl.*, 1882. 10.1051/jphystap:018820010024500.
- [22] A. Erturk and D.J. Inman. *Piezoelectric Energy Harvesting*. Wiley, 2011.
- [23] T. Fett and G. Thun. Determination of room-temperature tensile creep of pzt. *Journal of Materials Science Letters*, 17(22):1929–1931, 1998.
- [24] W.N. Findley, J.S. Lai, and K. Onaran. *Creep and Relaxation of Nonlinear Viscoelastic Materials: With an Introduction to Linear Viscoelasticity*. Dover Civil and Mechanical Engineering Series. Dover, 1976.
- [25] Victor M Franco Correia, Maria A Aguiar Gomes, Afzal Suleman, Cristóvão M Mota Soares, and Carlos A Mota Soares. Modelling and design of adaptive

- composite structures. *Computer Methods in Applied Mechanics and Engineering*, 185(2):325–346, 2000.
- [26] Y. Fung. *Biomechanics: mechanical properties of living tissues*. Biomechanics / Y. C. Fung. Springer-Verlag, 1981.
- [27] D. Gookin and R. Morris. Electro-optic hysteresis in polyvinylidene fluoride. *Applied Physics Letters*, 45:603, 1984.
- [28] AE Green and RS Rivlin. The mechanics of non-linear materials with memory. *Archive for rational mechanics and analysis*, 4(1):387–404, 1959.
- [29] Rami M Haj-Ali and Anastasia H Muliana. Numerical finite element formulation of the schapery non-linear viscoelastic material model. *International Journal for Numerical Methods in Engineering*, 59(1):25–45, 2004.
- [30] D. Hall. Review nonlinearity in piezoelectric ceramics. *Journal of Materials Science*, 36(19):4575–4601, 2001. 10.1023/A:1017959111402.
- [31] L Huang and HF Tiersten. An analytical description of slow hysteresis in polarized ferroelectric ceramic actuators. *Journal of Intelligent Material Systems and Structures*, 9(6):417–426, 1998.
- [32] L Huang and HF Tiersten. Electroelastic equations describing slow hysteresis in polarized ferroelectric ceramic plates. *Journal of applied physics*, 83(11):6126–6139, 1998.
- [33] Bernard Jaffe. *Piezoelectric ceramics*, volume 3. Elsevier, 2012.
- [34] A Jemai, F Najar, M Chafra, and Z Ounaies. Mathematical modeling of an active-fiber composite energy harvester with interdigitated electrodes. *Shock and Vibration*, 2014, 2014.

- [35] M. Kamlah and U. Bohle. Finite element analysis of piezoceramic components taking into account ferroelectric hysteresis behavior. *International Journal of Solids and Structures*, 38(4):605–633, 2001. cited By (since 1996)87.
- [36] Marc Kamlah and Charalampos Tsakmakis. Phenomenological modeling of the non-linear electro-mechanical coupling in ferroelectrics. *International Journal of Solids and Structures*, 36(5):669–695, 1999.
- [37] Ahmed A Khdeir and Osama J Aldraihem. Deflection analysis of beams with extension and shear piezoelectric patches using discontinuity functions. *Smart Materials and Structures*, 10(2):212, 2001.
- [38] S.-J. Kim and Q. Jiang. A finite element model for rate-dependent behavior of ferroelectric ceramics. *International Journal of Solids and Structures*, 39(4):1015–1030, 2002. cited By (since 1996)54.
- [39] S. Klinkel. A phenomenological constitutive model for ferroelastic and ferroelectric hysteresis effects in ferroelectric ceramics. *International Journal of Solids and Structures*, 43(22-23):7197–7222, 2006. cited By (since 1996)29.
- [40] S. Klinkel and W. Wagner. A geometrically non-linear piezoelectric solid shell element based on a mixed multi-field variational formulation. *International Journal for Numerical Methods in Engineering*, 65(3):349–382, 2006. cited By (since 1996)22.
- [41] W.M. Lai, D. Rubin, and E. Krempl. *Introduction to Continuum Mechanics*. Butterworth-Heinemann/Elsevier, 2009.
- [42] Chad M Landis. A new finite element formulation for electromechanical boundary value problems. *International Journal for Numerical Methods in Engineering*, 55(5):613–628, 2002.

- [43] D.J. Leo. *Engineering Analysis of Smart Material Systems*. Wiley InterScience. Wiley, 2007.
- [44] F. Li and D. Fang. Simulations of domain switching in ferroelectrics by a three-dimensional finite element model. *Mechanics of Materials*, 36(10):959–973, 2004. cited By (since 1996)46.
- [45] J. Li and G.J. Weng. A theory of domain switch for the nonlinear behaviour of ferro electrics. *Proceedings of the Royal Society A: Mathematical, Physical and Engineering Sciences*, 455(1989):3493–3511, 1999. cited By (since 1996)46.
- [46] J. Li and G.J. Weng. A micromechanics-based hysteresis model for ferroelectric ceramics. *Journal of Intelligent Material Systems and Structures*, 12(2):79–91, 2001. cited By (since 1996)36.
- [47] E. Lines and A.M. Glass. *Principles and Applications of Ferroelectrics and Related Materials*. OUP Oxford, 1977.
- [48] K. Linnemann, S. Klinkel, and W. Wagner. A constitutive model for magnetostrictive and piezoelectric materials. *International Journal of Solids and Structures*, 46(5):1149–1166, 2009. cited By (since 1996)21.
- [49] TS Low and W Guo. Modeling of a three-layer piezoelectric bimorph beam with hysteresis. *Microelectromechanical Systems, Journal of*, 4(4):230–237, 1995.
- [50] Christopher S Lynch. The effect of uniaxial stress on the electro-mechanical response of 8/65/35 plzt. *Acta Materialia*, 44(10):4137–4148, 1996.
- [51] Luis M. Macareno, Josu Agirrebeitia, Carlos Angulo, and Rafael Aviles. Fem subsystem replacement techniques for strength problems in variable geometry trusses. *Finite Elements in Analysis and Design*, 44(67):346 – 357, 2008.

- [52] C.V. Massalas, G. Foutsitzi, and V.K. Kalpakidis. Thermoelasticity theory for materials with memory. *International Journal of Engineering Science*, 32(7):1075–1084, 1994. cited By (since 1996)5.
- [53] G.A. Maugin. *Configurational Forces: Thermomechanics, Physics, Mathematics, and Numerics*. Modern Mechanics and Mathematics. Taylor & Francis, 2010.
- [54] KW Moored, TH Kemp, NE Houle, and H Bart-Smith. Analytical predictions, optimization, and design of a tensegrity-based artificial pectoral fin. *International Journal of Solids and Structures*, 48(22):3142–3159, 2011.
- [55] R. Mould. Pierre curie, 1859-1906. *Current Oncology*, 14(2):74, 2007.
- [56] A. Muliana. Time dependent behavior of ferroelectric materials undergoing changes in their material properties with electric field and temperature. *International Journal of Solids and Structures*, 48(19):2718–2731, 2011.
- [57] Anastasia Muliana. Large deformations of nonlinear viscoelastic and multi-responsive beams. *International Journal of Non-Linear Mechanics*, (0):–, 2014.
- [58] Anastasia Muliana and Chien-Hong Lin. A multi-scale formulation for predicting non-linear thermo-electro-mechanical response in heterogeneous bodies. *Journal of Intelligent Material Systems and Structures*, 22(8):723–738, 2011.
- [59] AC Pipkin and TG Rogers. A non-linear integral representation for viscoelastic behaviour. *Journal of the Mechanics and Physics of Solids*, 16(1):59–72, 1968.
- [60] S Raja, R Sreedep, and Gangan Prathap. Bending behavior of hybrid-actuated piezoelectric sandwich beams. *Journal of intelligent material systems and structures*, 15(8):611–619, 2004.

- [61] Micky Rakotondrabe, Cédric Clévy, and Philippe Lutz. Hysteresis and vibration compensation in a nonlinear unimorph piezocantilever. In *Intelligent Robots and Systems, 2008. IROS 2008. IEEE/RSJ International Conference on*, pages 558–563. IEEE, 2008.
- [62] Micky Rakotondrabe, Yassine Haddab, Philippe Lutz, et al. Plurilinear modeling and discrete μ -synthesis control of a hysteretic and creeped unimorph piezoelectric cantilever. In *9th International Conference on Control, Automation, Robotics and Vision, IEEE ICARV'06.*, number sur CD ROM, pages 57–64, 2006.
- [63] Richard A Schapery. On the characterization of nonlinear viscoelastic materials. *Polymer Engineering & Science*, 9(4):295–310, 1969.
- [64] Ansgar B Schaufele and Karl Heinz Hardtl. Ferroelastic properties of lead zirconate titanate ceramics. *Journal of the American Ceramic Society*, 79(10):2637–2640, 1996.
- [65] N. Schmidt. Coercive force and 90 degree domain wall motion in ferroelectric PLZT ceramics with square hysteresis loops. *Ferroelectrics*, 31(1):105–111, 1981.
- [66] R.C. Smith, S. Seellecke, M. Dapino, and Z. Ounaies. A unified framework for modeling hysteresis in ferroic materials. *Journal of the Mechanics and Physics of Solids*, 54(1):46–85, 2006. cited By (since 1996)70.
- [67] R.C. Smith, S. Seellecke, Z. Ounaies, and J. Smith. A free energy model for hysteresis in ferroelectric materials. *Journal of Intelligent Material Systems and Structures*, 14(11):719–739, 2003. cited By (since 1996)81.
- [68] AYN Sofla, DM Elzey, and HNG Wadley. Shape morphing hinged truss structures. *Smart Materials and Structures*, 18(6):065012, 2009.

- [69] A. Sohrabi and A. Muliana. *Nonlinear Hysteretic Response of Piezoelectric Ceramics, Ferroelectrics - Characterization and Modeling*. InTech, 2011. <http://www.intechopen.com/books/ferroelectrics-characterization-and-modeling/nonlinear-hysteretic-response-of-piezoelectric-ceramics>.
- [70] Amir Sohrabi and Anastasia Muliana. Rate-dependent electro-mechanical coupling response of ferroelectric materials: A finite element formulation. *Mechanics of Materials*, 62(0):44 – 59, 2013.
- [71] Y. Su and C.M. Landis. Continuum thermodynamics of ferroelectric domain evolution: Theory, finite element implementation, and application to domain wall pinning. *Journal of the Mechanics and Physics of Solids*, 55(2):280–305, 2007. cited By (since 1996)91.
- [72] A Suleman and VB Venkayya. A simple finite element formulation for a laminated composite plate with piezoelectric layers. *Journal of intelligent material systems and structures*, 6(6):776–782, 1995.
- [73] HF Tiersten. Electroelastic equations for electroded thin plates subject to large driving voltages. *Journal of Applied Physics*, 74(5):3389–3393, 1993.
- [74] Daniel Tscharnuter and Anastasia Muliana. Nonlinear response of viscoelastic polyoxymethylene (pom) at elevated temperatures. *Polymer*, 2012.
- [75] HS Tzou and CI Tseng. Distributed vibration control and identification of coupled elastic/piezoelectric systems: finite element formulation and applications. *Mechanical Systems and Signal Processing*, 5(3):215–231, 1991.
- [76] Timothy D Usher, Kenneth R Ulibarri, and Gilberto S Camargo. Piezoelectric microfiber composite actuators for morphing wings. *ISRN Materials Science*, 2013, 2013.

- [77] C.M. Wang, J.N. Reddy, and K.H. Lee. *Shear Deformable Beams and Plates: Relationships with Classical Solutions*. Elsevier Science, 2000.
- [78] Jie Wang and Marc Kamlah. Three-dimensional finite element modeling of polarization switching in a ferroelectric single domain with an impermeable notch. *Smart Materials and Structures*, 18(10):104008, 2009.
- [79] A.S. Wineman and K.R. Rajagopal. *Mechanical Response of Polymers: An Introduction*. Cambridge University Press, 2000.
- [80] Sung Yi, Shih Fu Ling, Ming Ying, Harry H Hilton, and Jack R Vinson. Finite element formulation for anisotropic coupled piezoelectro hygro thermo viscoelasto dynamic problems. *International journal for numerical methods in engineering*, 45(11):1531–1546, 1999.
- [81] Wenjun Zeng, Majid T. Manzari, James D. Lee, and Yin-Lin Shen. Fully coupled non-linear analysis of piezoelectric solids involving domain switching. *International Journal for Numerical Methods in Engineering*, 56(1):13–34, 2003.
- [82] W. Zhang and K. Bhattacharya. A computational model of ferroelectric domains. part i: Model formulation and domain switching. *Acta Materialia*, 53(1):185–198, 2005. cited By (since 1996)112.
- [83] Dayu Zhou and Marc Kamlah. Determination of room-temperature creep of soft lead zirconate titanate piezoceramics under static electric fields. *Journal of Applied Physics*, 98(10):104107–104107, 2005.
- [84] Dayu Zhou and Marc Kamlah. Room-temperature creep of soft pzt under static electrical and compressive stress loading. *Acta Materialia*, 54(5):1389–1396, 2006.

- [85] Dayu Zhou, Ruoyu Wang, and Marc Kamlah. Determination of reversible and irreversible contributions to the polarization and strain response of soft pzt using the partial unloading method. *Journal of the European Ceramic Society*, 30(12):2603–2615, 2010.

May 26, 2015